

İSTANBUL TECHNICAL UNIVERSITY ★ INSTITUTE OF SCIENCE AND TECHNOLOGY

**MECHANICAL PROPERTIES AND FRICTIONAL BEHAVIOUR OF
NANOPOROUS ANODIC ALUMINIUM OXIDE**

**M.Sc. Thesis by
Berkay KAVAS**

Department : Advanced Technologies

Programme : Materials Science and Engineering

NOVEMBER 2011

**MECHANICAL PROPERTIES AND FRICTIONAL BEHAVIOUR OF
NANOPOROUS ANODIC ALUMINIUM OXIDE**

M.Sc. Thesis by

Berkay KAVAS

Date of submission : 19 October 2011

Date of defense examination: 15 November 2011

**Supervisor (Chairman) : Assoc. Prof. Dr. Kürşat KAZMANLI
(ITU)**

**Members of the Examining Committee : Prof. Dr. Mustafa ÜRGEN (ITU)
Assoc. Prof. Dr. Gökhan ORHAN (IU)**

NOVEMBER 2011

İSTANBUL TEKNİK ÜNİVERSİTESİ ★ FEN BİLİMLERİ ENSTİTÜSÜ

**NANOPOROZ ANODİK ALÜMİNYUM OKSİTİN MEKANİK
ÖZELLİKLERİ VE SÜRTÜNME DAVRANIŞI**

YÜKSEK LİSANS TEZİ

Berkay KAVAS

Tezin Enstitüye Verildiği Tarih : 19 Ekim 2011

Tezin Savunulduğu Tarih : 15 Kasım 2011

Tez Danışmanı : Doç. Dr. Kürşat KAZMANLI (İTÜ)
Diğer Jüri Üyeleri : Prof. Dr. Mustafa Ürgen (İTÜ)
Doç. Dr. Gökhan ORHAN (İÜ)

KASIM 2011

FOREWORD

I would like to thank to my supervisor Assoc. Prof. Dr. Kürşat KAZMANLI for his guidance through out the period of my thesis studies. I am very much thankful to Prof. Dr. Mustafa ÜRGEN from Istanbul Technical University, Prof. Dr.-ir. Jean-Pierre CELIS and Marrie Curie Fellow Dr. Natalia TSYNTARU from Katholieke Universiteit Leuven for their tremendous support and guidance.

I would like to thank to Res. Assist. Beril AKINCI and Fatma BAYATA for their help and motivation, to Talat ALPAK and Wassim Zeineddine for SEM characterizations and to Marc Peeters and Pieter L'hoest for their technical assistance.

Finally and most importantly, I would like to thank to my parents who have never lost their belief in me and to my friends for keeping me motivated at all times.

October 2011

Berkay KAVAS

(Metallurgical and Materials Engineer)

TABLE OF CONTENTS

	<u>Page</u>
FOREWORD	v
TABLE OF CONTENTS	vii
LIST OF TABLES	xi
LIST OF FIGURES	xiii
SUMMARY	xvii
ÖZET	xix
1. INTRODUCTION AND THE AIM OF THE STUDY	1
1.1 History	2
2. STATE OF THE ART	5
2.1 Applications of Anodization and State of the Art Anodic Aluminium Oxide ...	5
2.1.1 Protective applications	5
2.1.2 Architectural applications	5
2.1.3 Nanotechnology applications.....	6
2.2 Anodization Process and Types of Aluminium Oxides	6
2.2.1 Types of oxides.....	7
2.2.1.1 Barrier oxides	7
2.2.1.2 Porous oxides	9
2.2.2 Thermodynamics and kinetics of AAO formation	11
2.2.3 Structure and composition of the aluminium oxide.....	12
2.2.4 Self-ordering	14
2.2.5 Two-step anodization of aluminium.....	15
2.2.5.1 Pretreatment of Al surfaces prior to anodization	17
2.2.5.2 Pore widening and surface porosity	20
2.3 Mechanical Properties of AAO	21
2.3.1 General Theory of nanoindentation	22
2.3.2 Characterization of mechanical properties of AAO by nanoindentation...	25
2.4 Tribological Properties and Wear Behaviour of AAO	30
2.4.1 Tribology and wear	30
2.4.1.1 Fretting	32
2.4.2 Tribological behaviour of non-porous AAO	33
2.4.3 Tribological characterization of porous AAO	35
3. EXPERIMENTAL METHODS	43
3.1 Production and Characterization of Samples	43
3.1.1 Surface preparations	43
3.1.2 Electropolishing	44
3.1.3 Anodizing	44
3.1.4 Mechanical characterization	46
3.1.5 Tribological characterization	46
3.2 Results and Discussion	46
3.2.1 Electropolishing	46

3.2.2 Composition, pore size and thickness of the oxide layer.....	47
3.2.3 Mechanical characterization by nanoindentation.....	53
3.2.4 Tribological characterization	62
3.2.4.1 Evolution of coefficient of friction.....	67
3.2.4.2 Wear tracks.....	70
4. CONCLUSIONS.....	75
REFERENCES	77
CIRRICULUM VITAE	81

ABBREVIATIONS

AAO	: Anodic Aluminium Oxide
COF	: Coefficient of Friction
DC	: Direct Current
E	: Elastic Modulus
EDS	: Energy Dispersive Spectroscopy
FEG	: Field Emission Gun
FIB	: Focused Ion Beam
mN	: Milinewton
N	: Newton
nm	: Nanometer
SEM	: Scanning Electron Microscopy
XRD	: X-Ray Diffractometer
µm	: Micrometer

LIST OF TABLES

	<u>Page</u>
Table 2.1: List of AAO forms (Choi, 2004).....	12
Table 2.2: Mobility behaviour of anion species (Choi, 2004)	14
Table 2.3 : Duration of the second anodizing step at various cell potentials (Sulka, 2006)	17
Table 2.4: Porosity percentages of samples (Xia, 2006).....	25
Table 2.5: Comparison of hardness by Oliver-Pharr method and true hardness (Ng, 2009).....	28
Table 2.6: Slip ratio – Friction regimes (Suciu, 2010).....	33
Table 3.1 : Linear growth rates of AAO during anodization in sulphuric acid (Sulka,2006)	49
Table 3.2: Sample names with pore diameters and porosity percentages	53
Table 3.3: Maximum penetration and final depths of the nanoindentation imprints under 100mN maximum load.....	57
Table 3.4: Slip ratios of S1 and S2.....	64
Table 3.5: Slip ratios of O1, O2 and O3	67

LIST OF FIGURES

	<u>Page</u>
Figure 2.1 : Anodizing Setup (Paşaoğlu, 2011)	7
Figure 2.2 : SEM image of a cross section of an amorphous aluminium oxide layer (top) grown on aluminium (bottom) in 0.16 M ammonium tartrate at 20°C with a current density of 10 mA/cm ² , voltage of 200 V. The oxide thickness is ~220 nm (Su, 2008).....	8
Figure 2.3 : Illustration of ion transport through barrier oxide layer (Hagelsieb, 2007)	8
Figure 2.5 : a)Current density vs. Anodization time, b)Illustration of AAO growth steps (Choi, 2004)	10
Figure 2.6 : a)Illustration of ion diffusion through barrier layer, b)SEM image of the barrier layer	11
Figure 2.7 : XRD patterns of AAO before and after annealing (Wang, 2004)	13
Figure 2.8 : Illustration of barrier-type and porous-type AAO(Hagelsieb, 2007)....	13
Figure 2.9 : GDOES profiles of the anodized surface a)Distribution of O,C, Al and S, b)High magnification of a part of (a) (Bensalah, 2011)	14
Figure 2.10 : Two step anodization steps a)electropolished surface, b)1 st anodization, c)oxide removal, d)2 nd anodization (Lee,2010)	15
Figure 2.11 : Double layer (Adelkhani, 2009)	18
Figure 2.12 : FEG-SEM image of AAO surface without electropolishing (Paşaoğlu, 2011)	19
Figure 2.13 : FEG-SEM image of AAO surface produced on electropolished aluminum (Paşaoğlu, 2011)	19
Figure 2.14 : SEM image of specimen with ~30nm pore diameter(d) and ~95nm interpore distance(D) (Vojkuvka, 2007)	20
Figure 2.15 : SEM images of AAO surface a) as-produced, b) after pore widening for 10 min, c) 20 min, d) 30 min, e) 40 min (Vojkuvka, 2007)	20
Figure 2.16 : Pore diameter and porosity as a function of widening time (Vojkuvka, 2007)	21
Figure 2.17 : Loading ranges of hardness testing methods (De Wolf, 2011)	21
Figure 2.18 : Berkovich indentation tip, $a = 65.3^\circ$ (Url-1)	22
Figure 2.19 : a) Load versus penetration depth for elastic-plastic loading followed by elastic unloading. h_c is the depth of the residual impression, h_f is the depth from the original specimen surface at load P_{max} , h_c is the elastic displacement during unloading. b) Crossectional representation of the indentation process showing distances used for analysis (Fischer-Cripps, 2002; Ko, 2006).....	23
Figure 2.20 : Examples of load-penetration depth curves a)Creep, b)Pop-out event, c)pop-in event, d)Elastic recovery, e)Full elastic recovery (De Wolf, 2011)	24

Figure 2.21: a) Transversely isotropic indentation modulus, b) hardness, c) residual stress as a function of sample porosity before and after heat treatment (Ko, 2006)	26
Figure 2.22: a) Load–displacement curve of AAO and b) SEM image of the nanoindentation imprint on AAO using a Berkovich indenter (Fang, 2008)	27
Figure 2.23: a) Top-view SEM images of the Berkovich indent revealing two systems of cracks. Maximum load 120mN, loading rate 1.5 mN min ⁻¹ and unloading rate 40 mN min ⁻¹ . b) Comparison of Berkovich indents made at increasing peak loads with a loading rate of 1.5 mN min ⁻¹ , showing similarity between the crack systems. c) High magnification SEM image of a bilinear crack d) Magnified views of cracks formed during indentations with different loading rates as 0.5, 5 and 50 mN min ⁻¹ from top to bottom respectively (Ng, 2009).	28
Figure 2.24: a) Indentation imprint on reinforced AAO with 200nm pore diameter under 400mN load, b) High-mag. of the crack indicated with the arrow in (a), c) SEM image of reinforced AAO with a pore diameter of 20nm, pile-up on the edges of the imprint, absence of cracks emanating from residual indent impression, d) cracks emanating from the residual indent impression on AAO (Kothari, 2009)	30
Figure 2.25: Sub-mechanisms of abrasive wear a) Ploughing, b) Cutting, c) Cracking (Stachowiak, 2001; Url-5)	31
Figure 2.26: Adhesive wear (Url-5)	31
Figure 2.27: Fretting Regimes a) Full stick regime, b) partial slip regime, c) gross slip regime, d) reciprocating sliding regime (Suciu, 2010)	33
Figure 2.28: COF values for samples produced at a current density of a) 0.100 A/cm ² , b) 0.125 A/cm ² , c) 0.150 A/cm ² (Baxi, 2008)	34
Figure 2.29: Illustration of solid lubricant precipitation within and over the porous film (Skeldon, 1996)	35
Figure 2.30: Evolution of COF on anodized A6061-T ₄ alloy with and without impregnation with iodine compound (Takaya, 2003)	36
Figure 2.31: a) Evolution of COF of as-produced and oil infiltrated AAO, b) variation of mean COF of oil infiltrated AAO vs. sliding velocity (Jiang, 2005)	37
Figure 2.32: SEM images of wear tracks formed under 980mN normal load with 0.2m/s velocity on a) as-prepared AAO, b) oil-infiltrated AAO (Jiang, 2005)	37
Figure 2.33: Porous Anodic Alumina (PAA) with a pore diameter of a) 50nm, b) 260nm, c) 470nm (Lee, 2011)	38
Figure 2.34: Evolution of COF on AAO with a pore diameter of a) 50nm, b) 260nm and c) 470nm. Black curves indicate condition 1, dark grey: condition 2 and light grey: condition 3	38
Figure 2.35: Illustration of releasing mechanism of water (Lee, 2011)	39
Figure 2.36: a) Evolution of COF with fretting cycles under 10mN load, b) COF of nanoporous AAO at various loads in relation to the pore diameter (Kim, 2010)	39
Figure 2.37: SEM images of tribolayer formed on the worn surfaces of nanoporous AAO films (Kim, 2010)	40
Figure 2.38: Wear track forming as a result of ductile deformations (Stachowiak, 2001)	41

Figure 3.1 : Experiment flow chart.....	43
Figure 3.2 : Anodization setup used for oxalic acid anodizing	45
Figure 3.3 : SEM image of Al surface a) prior to electropolishing; b) after electropolishing.....	47
Figure 3.4 : Surface profiles. a) method I, b)method II.....	47
Figure 3.5 : SEM images taken from different spots on the surface of anodized aluminium after a single step anodization at 21V.....	48
Figure 3.6 : Hexagonally distributed (indicated by white hexagon, b)well-ordered nanoporous AAO produced in sulphuric acid at a potential of a)15V, b)21V, for 97 and 20 min, at a temperature of ~1°C with pore diameters of a)~16nm, b)~27nm	48
Figure 3.7 : Crossectional FIB-SEM image of AAO produced in sulphuric acid....	50
Figure 3.8 : EDS results of AAO produced in sulphuric acid	50
Figure 3.9 : SEM images of hexagonally (indicated with white hexagon) arranged pores of AAO produced in oxalic acid at 40V (first step) and 70V (second step) a)high magnification, b)lower magnification	51
Figure 3.10 : EDS results of AAO produced in oxalic acid.....	51
Figure 3.11 : SEM images of AAO after pore widening for a)45min, b)60min, c)75min, d) 90min, e)110min	52
Figure 3.12 : AAO produced in oxalic acid and subjected to pore widening for a)32min, b)75min.....	52
Figure 3.13 : Crossectional FEG-SEM image of ~17µm thick AAO produced in oxalic acid	52
Figure 3.14 :SEM images of nanoindentation imprints done on AAO with a pore diameter of ~16 (S1) (a,d), ~27 (S2)(b,e) and 45 nm (O2) (c,f). The anodizing was done in sulphuric acid (a-e) and oxalic acid (c,f)	53
Figure 3.15 : SEM images of nanoindentation imprints under 50mN on a)S1, b)S2, c)O1, d)O2, e)O3	55
Figure 3.16 : Loading-unloading nanoindentation curves on AAO at 5 (magnified), 20, 50 and 100mN normal loads a)S1, b)S2, c)O1, d)O2, e)O3.....	56
Figure 3.17 : Hardness- Penetration depth curves of AAO produced in a)sulphuric acid, b)oxalic acid	58
Figure 3.18 : Corrected hardness-Penetration depth curves of a)S1 and S2, b)O1, O2 and O3, c)all samples	60
Figure 3.19 : Comparison of corrected hardness curves	61
Figure 3.21 : SEM Images of wear tracks on S1 (1Hz, 500µm, 1000 cycles) a,b) under 40mN normal load; overall view, center respectively and b)under 80mN; overall view and center, respectively	63
Figure 3.23 : SEM Images of different wear Tracks (50 cycles, 1 Hz, 100 µm displacement) on AAO anodized at 21 V: Normal load of a,b) 40mN, c,d) 80 mN	65
Figure 3.25 : Fretting loops of a)O1, b)O2, c)O3 under 1000mN loading	66
Figure 3.26 : Evolution of friction coefficient with number of cycles under various loads a)S1 b)S2	68
Figure 3.27 : Evolution of COF of samples produced in oxalic acid under 1000mN	69
Figure 3.28 : Evolution of COF of all samples	69
Figure 3.29 : SEM images of wear tracks at various magnifications on S2 under a normal load of a-c)40mN, d-f)80mN, g-i)1000mN	70
Figure 3.30 : a)Thin debris layer with minor cracks (dark grey), b)Layered debris structure (light grey)	71

Figure 3.31: SEM images of wear tracks at various magnifications on O2 under a normal load of 1000mN 71

Figure 3.32: SEM images of wear tracks at various magnifications on O3 under a normal load of 1000mN 72

Figure 3.33: a)SEM image of wear track under a normal load of 1000mN on O3 at high magnification b)Cracks (indicated with arrows) within the same wear track on O3 72

MECHANICAL PROPERTIES AND FRICTIONAL BEHAVIOUR OF NANOPOROUS ANODIC ALUMINIUM OXIDE

SUMMARY

Anodic aluminium oxide (AAO) has various fields of use due to its unique structure. A surface consisting of well-ordered nanopores can easily be produced by anodizing which is indeed a simple and cost-effective method. AAO can be used for nanotechnology applications, protective purposes and architectural applications. Porous structure creates a possibility to use AAO in self-lubricating systems as the pores can be filled with solid or liquid lubricants.

In this study we investigated the mechanical properties of AAO using nanoindentation technique. Mechanical characterization was followed by tribological characterization by ball-on-flat test system to reveal the wear mechanism of AAO in possible application areas under dry conditions.

Prior to anodization, samples were electropolished by two different methods one of which is available for industrial use. Two-step anodization was performed for obtaining a homogeneous distribution of pores. Sulphuric acid and oxalic acid were used as electrolyte to produce AAO with different characteristics in terms of pore size, porosity percentage and chemical composition. After producing the samples with desired properties, nanoindentation tests were carried out using a Berkovich tip. Mechanical properties were investigated and imprints were also observed with SEM. No major cracks were seen. Mechanical properties showed differences in relation to porosity and chemical composition.

Tribological characterization revealed the wear behavior of AAO. Porous structure was expected to respond by propagation of cracks or shattering of tubes. But the results were otherwise without any severe damage. In the beginning of fretting tests, pores were filled with debris followed by formation of a highly adherent thirdbody consisting of fine wear particles from both the counterbody and the samples. The tubular structure was retained underneath the debris layer. Coefficient of friction was high regardless of chemical composition. It varied with porosity percentage due to change in contact pressure.

NANOPOROZ ANODİK ALUMİNYUM OKSİTİN MEKANİK ÖZELLİKLERİ VE SÜRTÜNME DAVRANIŞI

ÖZET

Anodik aluminyum oksit (AAO) özel yapısına bağı olarak çeşitli kullanım alanlarına sahiptir. Aluminyum üzerinde düzenli nano boyutta tüplü yapıdan oluşan bir oksit tabakası, basit ve ucuz bir yöntem olan anodizasyon ile kolayca oluşturulabilir. AAO nanoteknoloji uygulamalarında, yüzey koruması amacıyla ve de dekoratif uygulamalarda kullanılabilir. Poroz yapısı katı yada sıvı yağlayıcılar ile doldurulabileceğinden, kendinden yağlamalı sistemlerde kullanımına olanak sağlar.

Bu çalışmada AAO'nun mekanik özellikleri nano sertlik ölçüm tekniği ile incelenmiştir. Mekanik karakterizasyonu takiben potansiyel kullanım alanlarındaki aşınma davranışının incelenmesi amacıyla "ball-on-flat" test yöntemi kullanılarak tribolojik karakterizasyonu yapılmıştır.

Anodizasyon öncesi yüzey iki farklı metod kullanılarak elektro-parlatma işlemine tabi tutulmuştur. Bu iki yöntemden biri endüstriyel uygulamalarda kullanılmaktadır. Parlatma işlemi sonrasında, düzenli dağılımına sahip poroz yapı eldesi için iki-basamaklı anodizasyon gerçekleştirilmiştir. Farklı delik çapı, porozite yüzdesi ve kimyasal bileşime sahip AAO üretmek amacıyla anodizasyon sırasında sülfürik ve oksalik asit kullanılmıştır. Arzulanan özelliklere sahip numuneler üretildikten sonra, Berkovich elmas uç kullanılarak mekanik özellikler incelenmiştir. Sertlik izleri taramalı elektron mikroskobu kullanılarak gözlenmiş ve büyük boyutta çatlaklara rastlanmamıştır. Mekanik özellikler porozite yüzdesi ve kimyasal kompozisyona göre farklılık göstermiştir.

Tribolojik karakterizasyon ile AAO'nun aşınma davranışı incelenmiştir. Poroz yapı üzerine iki yönlü yük uygulanmasına karşın, herhangi bir çatlak oluşumu ya da tüplü yapının parçalandığı gözlemlenmemiştir. Test başlangıcında tüpler çok ince tanelerden oluşan debris ile önce dolmuş, sonra birbirine yapışan debris ile kaplanmış ve oldukça yapışkan "thirdbody" oluşmuştur. Tüplü ve poroz yapı aşınma testi sonunda, debrisin altında muhafaza edilmiştir. Sürtünme katsayısı oldukça yüksektir ve porozite yüzdesine bağı olarak değişiklik göstermiştir.

1. INTRODUCTION AND THE AIM OF THE STUDY

Anodizing is an electrochemical process which is performed to form a protective oxide layer on the surface of a metal. Basically it is a method to grow a controlled oxide layer rather than naturally formed metal oxide. Purpose of forming such a layer might be for different reasons such as corrosion or wear resistance, increasing surface hardness or even obtaining a different appearance. Utilizing this process allows us to use a metal in applications for which it might not otherwise be suitable for the area of use. Anodic film formation is mostly applied on different metals namely titanium (Ti) and aluminium (Al). However, it is known that zinc, magnesium, niobium and tantalum can also be anodized (Url-1; Choi, 2004)

Anodizing as a surface finish on aluminium has got plenty of advantages such as high durability since oxide layer with respect to the nature of the process, is highly adhered to the underlying aluminium; color stability as they provide good stability against ultra-violet rays. It is a fact that it improves wear resistance as a result of which material loss caused by wear or friction highly decreases. In addition low cost and ease of processing makes it a highly preferable option (Url-2, Url-3).

Aluminium anodizing in industrial scale is mostly performed to improve the low corrosion resistance of aluminium, increasing the material resistance to scratching and even introducing decorative finishes such as coloring. Due to the nature of aluminium metal, anodic aluminium oxide (AAO) has a unique property which makes it a great point of interest : nano porous structure. This porous structure can be randomly spread on the surface or depending on the production method, can be highly ordered. Besides the applications mentioned, this unique property allows uses in nanotechnology field since it can be employed as a template in nano-rod, -wire production as well as micro electromechanical systems (MEMS). Porous structure also creates a possibility to use AAO in self lubricating systems as the nano-pores can be filled with different materials with lubricious properties (Url-1; Url-2; Choi, 2004).

To be able to use AAO in such applications as self lubricating systems or in

applications where it is subjected to load or friction, indeed mechanical properties and frictional behaviour must be investigated. Although in the last decade plenty of researches has been carried out regarding mechanical properties of AAO, there is still lack of information about mechanical properties (Xia, 2004; Ko, 2005; Fang, 2007). Research or information concerning tribological properties are not sufficient either. As for tribological characterization, Skeldon et al. (1997) and Jiang et al. (2005) reported results regarding friction behaviour of AAO filled with solid or liquid lubricants. But the frictional behaviour of AAO itself is still a question.

In this study we investigated the mechanical properties of AAO using nanoindentation technique with Berkovich indentation tip followed by tribological characterization employing a ball-on-flat test system. Effect of pore diameter, porosity and the type of anodizing electrolyte on mechanical and tribological properties were studied. We believe that deeper investigation and understanding of physical response and wear behaviour of AAO will lead us towards new ideas as well as new application areas.

1.1 History

Anodic oxidation of aluminium dates back to the beginning of the last century when it was first used to obtain protective surface properties against corrosion or for cosmetic purposes. In the early 80's self-ordered hexagonal porous structure has been exploited. Although anodization once was done on aluminium for surface protection, with the discovery of this self-ordered structure, scientists started to use this unique material for nanotechnology applications (Choi, 2004).

Since the early years of the last century, aluminium has been anodized in different acid baths according to the needs. In time, it was realised that the properties of the oxide could be modified by adjusting anodizing parameters and electrolyte. Later it became possible to colour the anodic oxide by further treatment in electrolytes containing metal salts such as copper, nickel, silver etc. Bengough and Stuart's patent in 1923 was a break-through in anodic oxidation field which provided a way to protect Al and its alloys against corrosion by anodizing in chromic acid bath (Choi, 2004; Huh, 2007; Khan, 2010).

Many research were done in the following years about the fundamentals, modelling and optimization of anodization process. Especially after the developments made in scanning electron microscopy, information on these topics showed a great increase. O'Sullivan and Wood whose publication was one of the most cited, took an important step for a better understanding of oxidation morphology and mechanism (O'Sullivan, 1970; Choi, 2004).

What we can consider as the second break-through in anodization history was two-step anodization of aluminium found by Masuda and Fukuda in 1995. They offered a method that made it possible to obtain well-ordered nanoporous structure with high aspect ratios (Masuda, 1995).

After recent developments on well-ordered surface, state of the art AAO with honeycomb architecture is mainly used as a template in production of nano-structured materials since the dimensions can be controlled precisely. Currently, research on surface structure, mechanical and tribological properties is still being done (Sulka, 2009; Hagelsieb, 2004; Key, 2010).

2. STATE OF THE ART

2.1 Applications of Anodization and State of the Art Anodic Aluminium Oxide

Anodization, because of its nature-friendly properties and low cost, has become a point of interest in the last century. Anodization can be used in different fields or for different applications. Protection of a surface against corrosion, decorative metal finish, architectural and nanotechnology applications, electrolytic capacitors, humidity sensors, self lubricating systems and aerospace structures can be given as examples.

2.1.1 Protective applications

Anodization of aluminium can be for protection reasons. Aluminium itself is not resistant to corrosion. However, by anodization things can go the other way round and aluminium surface can gain resistance against any mean of corrosion. Chromic acid anodizing can provide high corrosion resistance relative to the thickness of the oxide. By sulfuric acid anodizing, hard oxide films can be produced as well as soft ones which are also for decorative use. Hard oxide films can be used in aerospace industry. Phosphoric acid anodizing is basically used for structural adhesive bonding in high-humidity environments. The sulphuric acid formed oxide film has a greater durability under adverse conditions than film formed in chromic acid and sulphuric acid (Url-4).

2.1.2 Architectural applications

Anodized aluminium can be employed on window, door frames and other exterior structural panels of parts. Properties of alumina make it a good option for such applications since these structures must stand against harsh atmospheric conditions and . Unlike paintings, the oxide layer is fully integrated with the aluminium base which makes it harder to be peeled. In addition, the porous structure can be filled by depositing additives such as tin or nickel at the bottom of tubes. This deposition enables surface coloring which is very important for decorative and architectural

fields of use. In addition there is a wide range of colors which are stable for a long time (Url-2; Hagelsieb, 2007).

2.1.3 Nanotechnology applications

Nanomaterials have attracted attention in the last decade for their possible applications in close future. Anodic aluminium oxide has a very important place in nanotechnology applications. Its unique well-ordered porous structure makes it a great point of interest. It is basically used as a template for production of nanorods, nanowires and nanotubes. Easy and low costly control of properties such as pore diameter, interpore distance, tube height, time and temperature are advantages of AAO in nanotechnology field since controlling these also means controlling properties of nano structured materials. Besides production of nano structured materials, nanoporous AAO is an option for applications where self-lubricating might be needed (Zaraska, 2010; Hagelsieb, 2007; Öztürk, 2009; Skeldon, 1997).

2.2 Anodization Process and Types of Aluminium Oxides

Anodization is not the only way to produce oxides. Other methods such as evaporation or plasma enhanced chemical vapor deposition (PECVD) are known to be used for oxidation. But among these, advantages of anodizing make it more attractive. Low cost, more precise thickness control and easier handling of process can be given as examples to these advantages (Hagelsieb, 2007).

Anodization is a very simple oxidation process employed in a two-electrode electrochemical cell consisting of an anode (aluminium or aluminium alloy), a cathode (stainless steel or platinum), DC or AC power supply and electrolyte (Figure 2.1). By applying direct current, a controlled growth of oxide layer on surface of the anode is achieved where the surface is in contact with the electrolyte. Anodic oxide structure is not applied onto the surface as a film. Unlike electroplating, it is a surface finish which originates from the base metal itself by turning the metal into its oxide (e.g. Al to Al_2O_3). As in case of anodic aluminium oxide (AAO), the oxide layer is fully integrated with aluminium underneath, which prevents it from being peeled or chipped. (Url-2; Hagelsieb, 2007; Choi, 2004; Paşaoğlu, 2011; Lee, 2010).

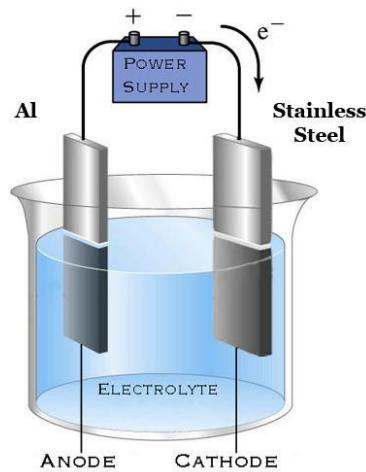


Figure 2.1: Anodizing Setup (Paşaoğlu, 2011)

During anodization of Al, O_2 evolution takes place that covers the anode and AAO is formed as a result of anodization reactions which will be discussed later. Unlike the rest of the surface treatments such as electroplating, anodizing takes place on the interchange surface between aluminium and aluminium oxide which grows inwards aluminium.

Aluminium is a unique metal among the rest of the metals those can be anodized, (e.g. niobium, tantalum, titanium, tungsten) since either a thick non-porous oxide or a coating consisting of pores in nano-scale can be achieved by anodizing.

Both type of oxide layers can be grown on aluminium depending on the electrolyte used during anodization. Nonporous (barrier) oxide film grows in solutions that alumina has very low solubility, such as solution containing ammonium borate, phosphate or tartrate compounds. pH of the electrolyte should be between 5 and 7 for such a formation. In case of using an electrolyte in which aluminium oxide has limited solubility, porous oxide film can be obtained with simultaneous formation-dissolution reactions. Dilute sulphuric, oxalic or phosphoric acids can be used for such oxide film production (Hagelsieb, 2007; Choi, 2004). In this study, we will be mainly focused on porous type AAO.

2.2.1 Types of oxides

2.2.1.1 Barrier oxides

Aluminium is well known for its high activity in air. It can easily react with air which results in formation of a barrier oxide layer on the surface. This thin barrier oxide

serves as a protective layer against further oxidation (figure 2.2). If it can be grown under control, aluminium surface can be mechanically stronger and can have higher resistance against chemicals and corrosion.

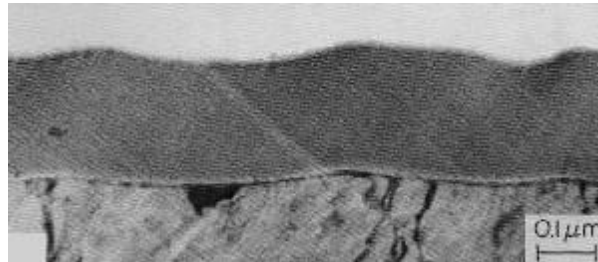


Figure 2.2: SEM image of a cross section of an amorphous aluminium oxide layer (top) grown on aluminium (bottom) in 0.16 M ammonium tartrate at 20°C with a current density of 10 mA/cm², voltage of 200 V. The oxide thickness is ~220 nm (Su, 2008)

When aluminum is covered with its native barrier oxide and used as an anode in an electrolytic cell, electrical potential can be increased without any significant change in current until the potential reaches a high level to make oxide and aluminium ions pass native barrier. Barrier type oxide is capable of resisting an electric field in a range from 10⁶ to 10⁷ V/cm. In case of using aluminium as the anode in an electrolytic cell containing a near neutral electrolyte such as ammonium tartrate, oxide layer grows at both interfaces (oxide-metal and oxide-electrolyte) of the oxide. Diffusion of oxygen-containing anions (O²⁻/OH⁻) takes place from the electrolyte to oxide-aluminium interface where they cause formation of aluminium oxide. At the same time aluminium cations (Al³⁺) diffuse through oxide layer and deposit on oxide-electrolyte interface as alumina. This diffusion is illustrated in (figure 2.3). Circuit is completed at the cathode by reduction of hydrogen ions. Hydrogen gas evolves as a result of reduction (Hagelsieb, 2007; Su, 2008; Paşaoğlu, 2011; Choi 2004).

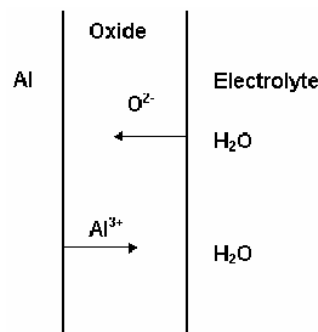


Figure 2.3: Illustration of ion transport through barrier oxide layer (Hagelsieb, 2007)

2.2.1.2 Porous oxides

Mostly, porous aluminium oxides are grown in dilute acid solutions namely sulfuric acid, oxalic acid, phosphoric acid and chromic acid. Recently, chromic acid hasn't been preferred due to its carcinogenic effects since it contains chrome (VI) which is highly toxic (Url-4).

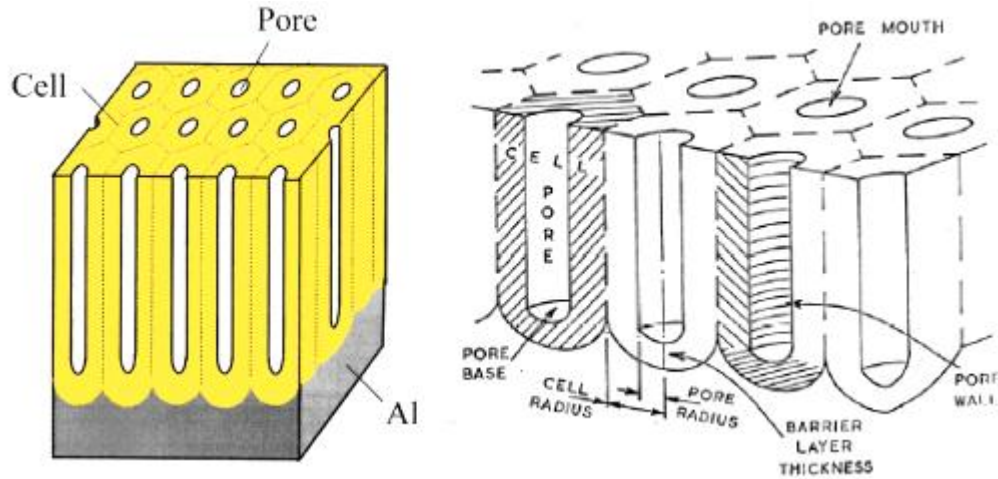


Figure 2.4: Illustration of well-ordered nanoporous AAO (Url-3; Hagelsieb, 2007)

Porous aluminium oxide consists of cellular pores those grow deep down as tubes. Each tube has a thin oxide layer at the bottom which is called barrier layer (figure 2.4). The thickness of the barrier layer is dependent on different variables such as electrolyte used for anodization or potential applied. Another important feature of the electrolyte is retaining alumina particles since a large fraction of alumina passes to the electrolyte. Unlike barrier type oxides, porous oxides form as a result of dissolution reactions. This can be considered as a source of alumina particles.

As for pore formation mechanism, following current densities until they reach a steady state, helps us understand how the pores form (figure 2.5a).. In the beginning of anodization, a thin natural barrier oxide film is present on the surface (figure 2.5b1). This barrier is a non-conductive thin oxide as mentioned previously. Under applied potential, electric field focuses on fluctuations locally, leading to temperature or/and field-enhanced dissolution of the oxide via the shortest paths between the base metal and the electrolyte. As dissolution carries on until the bottoms of the tubes reach the same level, current density decreases as shown in (figure 2.5a) region 1,2 and 3. Once each tube has the same height (figure 2.5b-4), current density becomes steady which is shown in figure 2.5a region 4. Figure 2.6a is high magnification

offigure 2.5b region 4 which shows the shortest path between the electrolyte and aluminium.

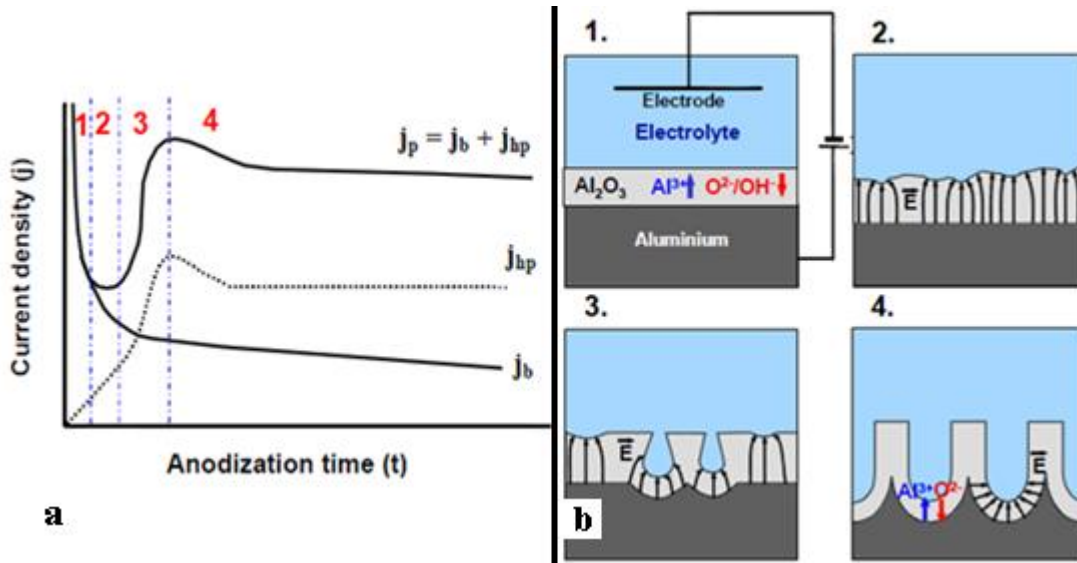


Figure 2.5: a)Current density vs. Anodization time, b)Illustration of AAO growth steps (Choi, 2004)

SEM image of the barrier layer is given in figure 2.6b. Ions move by high field conduction via this path. Oxygen containing ions O^{2-}/OH^- immigrate to the bottom of the pore from the electrolyte and reacting with aluminium, they form Al_2O_3 at metal-oxide interface as in barrier type oxides. Meanwhile, at oxide-electrolyte interface at the bottom of the tubes, alumina dissolves (Figure 2.6).

Pores grow inwards aluminium with this mechanism. The part which had been the barrier oxide at the early stage of pore formation becomes a part of the cell wall while the bottom goes deep inside making the tubes thicker. Pore diameter remains fixed. The thickness of the barrier film is also constant during this process due to formation and dissolution reactions taking place simultaneously. This lets the potential applied and the current remain stable while the film thickens (Hagelsieb, 2007; Choi, 2004; Paşaoğlu, 2011).

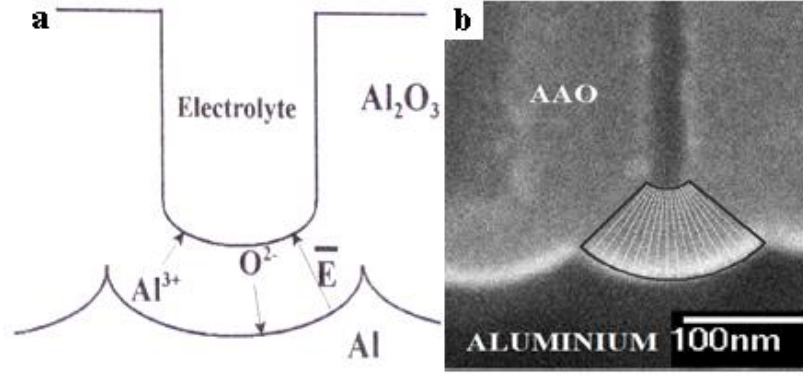
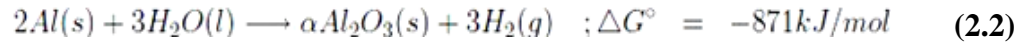
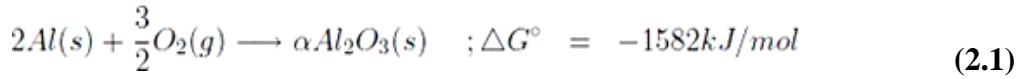


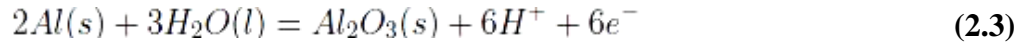
Figure 2.6: a) Illustration of ion diffusion through barrier layer, b) SEM image of the barrier layer

2.2.2 Thermodynamics and kinetics of AAO formation

The spontaneous reaction causing the formation of aluminium oxide in air atmosphere can be linked to the large negative Gibb's free energy changes.



During anodization, oxide layer grows on the anode electrode,



and hydrogen evolution is recognized on the cathode.



Current density passing via the oxide film can be written as :

$$j_i = j_a + j_c + j_e \quad (2.5)$$

In the equation j_a , j_c and j_e stand for the anion-contributing, cation-contributing and electron-contributing current density, respectively. As anodic aluminium oxide is an insulator, the electronic conductivity is very low. Therefore the ionic current density ($j_i = j_a + j_c$) is the predominant mode to transport charges. Guntherschultze-Betz equation is used to express the relationship between j_i and the electric field applied E :

$$j_i = j_0 \cdot \exp(\beta E) \quad (2.6)$$

where j_0 and β terms in the equation are temperature and metal dependent terms, respectively. For aluminum oxide, j_0 is between 1×10^{-16} and 3×10^{-2} mA/cm² and β

changes between 1×10^{-7} to 5.1×10^{-6} cm/V. E on the other hand, varies from 10^6 to 10^7 V/cm (Choi, 2004; Paşaoğlu, 2011).

2.2.3 Structure and composition of the aluminium oxide

As a result of a number of polymorphs, hydrates and incorporated ions, anodic aluminium oxide can form in different forms e.g. $\text{Al}_2\text{O}_3 \cdot (\text{H}_2\text{O})_n$ where n varies between 0 and 3. A list of different AAO forms is given in Table 2.1. Corundum is the most stable form of alumina. It is generated above 1100°C regardless of the transition course. Other types of aluminium oxides such as gibbsite and boehmite can be converted to gamma alumina consisting of irregular structure, by heat treatment. Mostly, alumina formed by anodization is reported to have amorphous structure. (Choi, 2004; Hagelsieb, 2007).

Table 2.1: List of AAO forms (Choi, 2004)

Name	Crystalline form	Density (g/cm^3) / Crystal system	Remark
Corundum	$\alpha\text{-Al}_2\text{O}_3$	3.97 / hexagonal	found in nature
Boehmite	$\alpha\text{-Al}_2\text{O}_3 \cdot \text{H}_2\text{O}$	3.44 / ortho-rhombic	
Gibbsite	$\alpha\text{-Al}_2\text{O}_3 \cdot (\text{H}_2\text{O})_3$	2.42 / monoclinic	
Diaspore	$\beta\text{-Al}_2\text{O}_3 \cdot (\text{H}_2\text{O})$	3.4 / ortho-rhombic	no occurrence in nature
Bayerite	$\beta\text{-Al}_2\text{O}_3 \cdot (\text{H}_2\text{O})_3$	2.53 / monoclinic	
Gamma alumina	$\gamma\text{-Al}_2\text{O}_3$	/	anhydrous alumina with ill-defined structure

Wang et al. annealed commercially available anodic alumina templates at various temperatures, namely 150°C , 300°C , 450°C and 600°C . It was seen that the templates had amorphous structure in the beginning. After annealing boehmite ($\gamma\text{-AlOOH}$) and nordstrandite ($\beta\text{-Al}(\text{OH})_3$) phases of alumina were observed. XRD patterns are given in figure 2.7. This showed that anodic alumina structure consists of not only pure alumina but also its aluminium hydro-oxide (Wang, 2004).

During anodization, electrolyte can also affect the composition of the oxide via contamination. Anodic aluminium oxides, both barrier type and porous type, have an outer oxide that starts at oxide-electrolyte interface and an inner oxide which starts at oxide-metal interface as shown in figure 2.8. Outer oxide consists of alumina which has incorporated anions while inner oxide is the high purity amorphous alumina (Hagelsieb, 2007; Kylan, 2011).

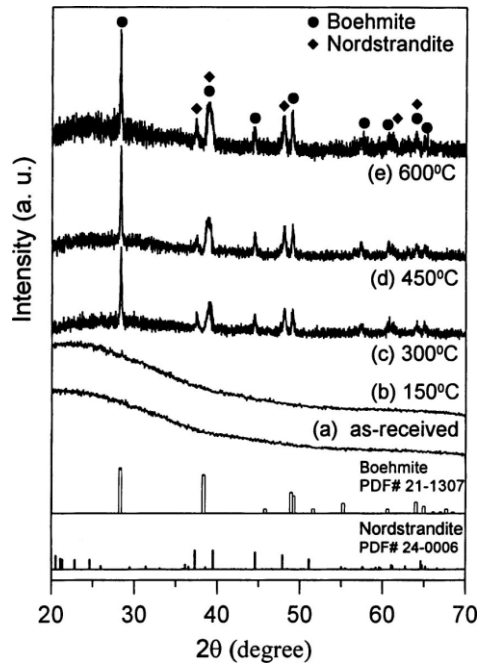


Figure 2.7: XRD patterns of AAO before and after annealing (Wang, 2004)

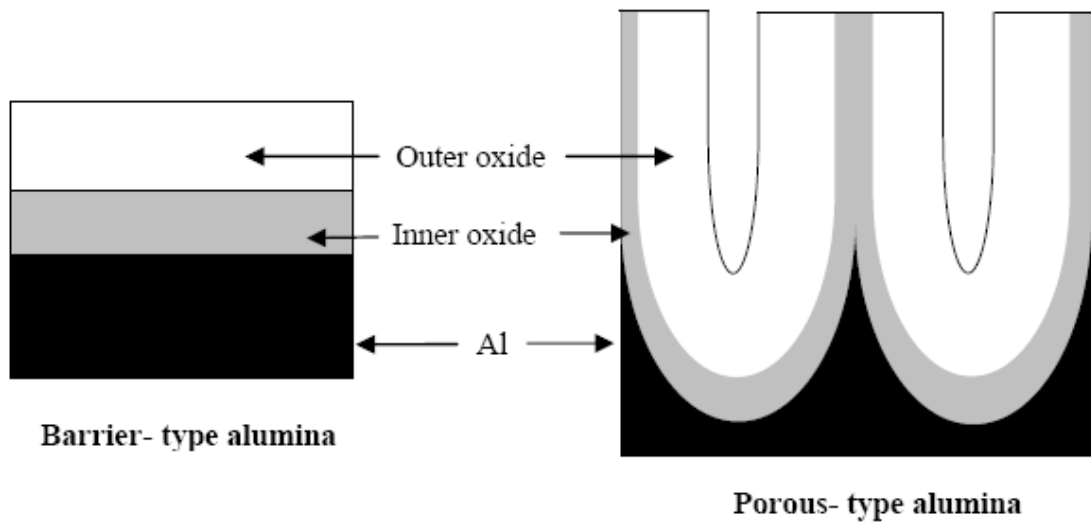


Figure 2.8: Illustration of barrier-type and porous-type AAO(Hagelsieb, 2007)

Level of contamination is strongly dependant on the electrolyte as well as the concentration of absorbed anions and the faradaic efficiency of the film growth. There are three types of electrolytes in means of mobility in the oxide ; immobile, inwardly mobile and outwardly mobile ions. Sulfate for instance, moves inward the outer oxide and causes sulphur contamination (Hagelsieb, 2007). In table 2.2electrolytes are given according to their mobility behaviour.

Bensalah et al. studied contamination of the oxide by SO_4^{2-} and $(\text{COO}^-)_2$ anions, source of which were sulphuric acid and oxalic acid used for anodization, respectively (2011). They investigated the anodic layers by GDOES technique.

Table 2.2: Mobility behaviour of anion species (Choi, 2004)

Immobile species	Outwardly mobile species	Inwardly mobile species
Silicate, Arsenate	Antimonate, Chromate, Borate, Molybdate	Phosphate, Sulfate, Selenate

The curves they obtained are given in figure 2.9. As can be seen in GDOES profiles, in case of anodizing in oxalic acid bath, C was present within the oxide while sulphuric acid anodizing caused S species to penetrate in the oxide. $(\text{COO}^-)_2$ anions were found at a short range from the surface. SO_4^{2-} anions however, migrated to inner levels of the oxide (Bensalah, 2011).

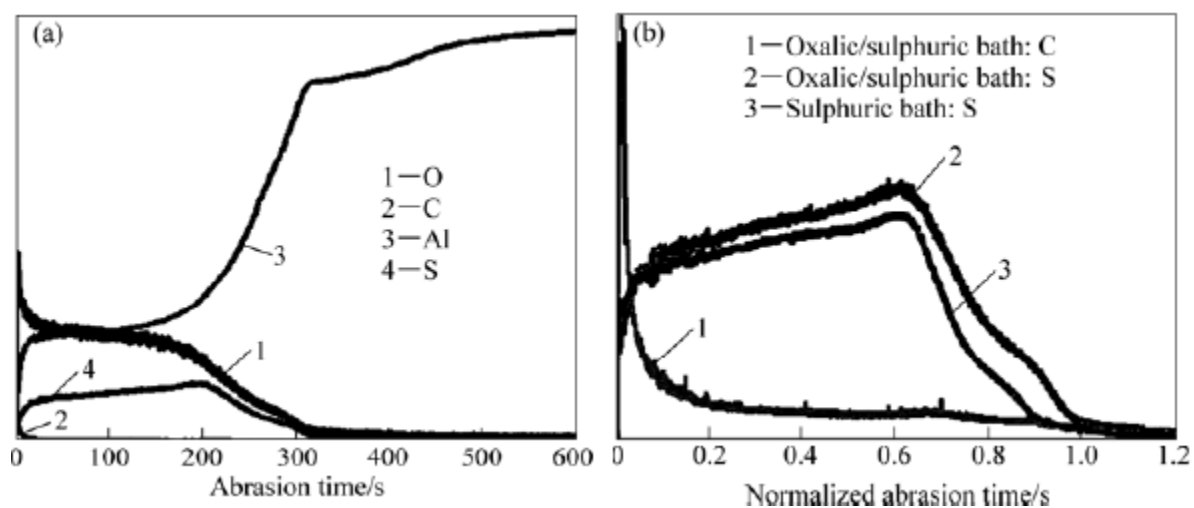


Figure 2.9:GDOES profiles of the anodized surface a)Distribution of O,C, Al and S, b)High magnification of a part of (a) (Bensalah, 2011)

2.2.4 Self-ordering

The driving force behind this self-assembly is linked to the repulsive forces between adjacent pores causing mechanical stress. These repulsive forces are suggested to occur because of the density difference between aluminium and alumina. Atomic density of aluminium in Al_2O_3 , is lower than the one in metallic aluminium by a factor of 2 which makes volume of anodized alumina expand to approximately twice the original volume. This volume expansion leads to compressive stress at oxide-metal interface pushing the pore walls vertically. If the stress is maximal, no pores are

generated. Disordered structure takes place if the stress is too small. In case of moderate forces, pores grow in an ordered manner (Choi, 2004).

In 1995, Masuda and Fukuda discovered that AAO can exhibit self-ordered porous structure in case of anodizing for long durations in 0.3M oxalic acid. They reported that the pores arranged regularly formed a honeycomb structure. This invention encouraged scientists for further research which in the end led to the development of “two-step anodization” (figure 2.10). Two-step anodization provided production of AAO with highly ordered nano-pores. Thus, anodization of aluminium became a greater point of interest especially for those who are working in nanotechnology field (Masuda, 1995; Choi, 2004; Lee, 2010).

2.2.5 Two-step anodization of aluminium

In 1995, Masuda and Fukuda discovered that AAO can exhibit self-ordered porous structure in case of anodizing for long durations in 0.3M oxalic acid. They reported that the pores arranged regularly formed a honeycomb structure. This invention encouraged scientists for further research which in the end led to the development of “two-step anodization” (Fig.2.10). Two-step anodization provided production of AAO with highly ordered nano-pores. Thus, anodization of aluminium became a greater point of interest especially for those who are working in nanotechnology field (Masuda, 1995; Choi, 2004; Lee, 2010).

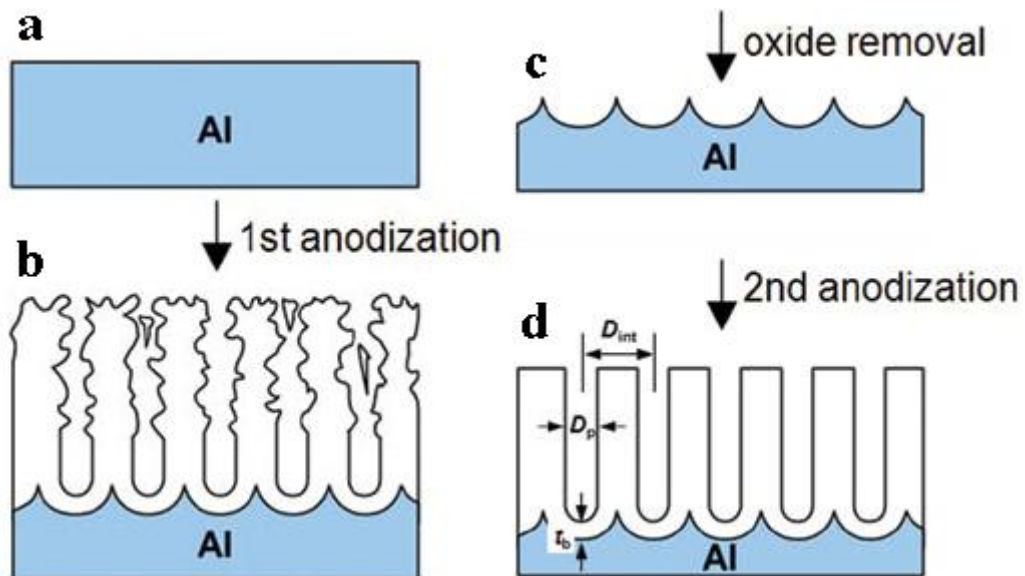


Figure 2.10: Two step anodization steps a) electropolished surface, b) 1st anodization, c) oxide removal, d) 2nd anodization (Lee, 2010)

In the first anodization step, porous structure starts to form. However no well-ordered arrangement of pores is noticed (figure 2.10b). Pores start to grow inwards aluminium base in random directions until a period when all the tube bottoms are at the same level, parallel to each other. This is when oxide removal process is carried out. By removing this oxide, a pre-pattern is produced on aluminium for the second anodization step during which well-ordered structure is obtained (figure 2.10c). Finally second anodization, which is basically the same as the first one, is performed to produce a surface consisting of well-ordered nano pores (Zhao, 2007; Sulka, 2006; Lee, 2011, Choi, 2004).

Masuda and Fukuda first performed two-step anodization in 0.3M oxalic acid bath. Since then, as mentioned previously, two-step anodization became a point of interest. Many other researchers studied on this topic. Sulka performed two step anodization in sulphuric acid (20% wt) at low temperatures ($\sim 1^{\circ}\text{C}$) at potentials between 15 and 25V. As easily noticed, it wasn't as high as applied in Masuda's research since the conduction of sulphuric acid is very high compared to oxalic acid and this may cause breakdown of the anodic oxide layer. It should be noted that each type of bath used has its own potential range. Sulphuric acid is suitable for potentials between 5 ~40V while oxalic acid can be used within a range of 30 ~120V. Phosphoric acid is capable of handling potentials varying between 80 ~200V. Lee and colleagues used both oxalic acid and phosphoric acid for the production of AAO with various pore diameters. Zhao was one of the researchers who also preferred sulphuric acid bath. Working temperature of the first step anodization varied between 0 and 30°C . (Masuda, 1995; Zhao, 2007; Sulka, 2006; Lee, 2011, Choi, 2004).

Oxide removal is generally performed by immersing first-step anodized samples in a chromic acid- phosphoric acid solution consisting of 6 wt. % phosphoric acid, 1.8 wt. % chromic acid at $60\text{-}80^{\circ}\text{C}$. Time of removal depends on the thickness of the first oxide layer. Zaraska performed oxide removal process for durations varying from 10min to 15 min for samples he produced in sulphuric acid. Paşaoğlu ran the first step in 0.3M oxalic acid bath and oxide removal was done for 1h (Zaraska, 2010; Paşaoğlu, 2011).

Finally, aluminium is anodized for the second time to produce the final AAO with acquired thickness and pore diameter. Electrolyte, potential applied, temperature and duration are the parameters affecting the final thickness and the pore diameter. Table

2.3 gives potential dependent durations required for obtaining a 90µm thick AAO on aluminium in sulphuric acid bath at 1°C.

Table 2.3: Duration of the second anodizing step at various cell potentials (Sulka, 2006)

Anodising potential [V]	15	17	19	21	23	25
Time [min]	870	560	400	185	113	45

2.2.5.1 Pretreatment of Al surfaces prior to anodization

In two step anodization, for achieving a uniform anodized surface, the surfaces must have low roughness. For this reason, electropolishing must be performed on aluminium to obtain the necessary surface roughness prior to anodization. Also anodizing large grains gives better results since in smaller grains the orientation may mislead to a loss of ordering. Thus, before electropolishing aluminium must be annealed for grain size enlargement.

Electropolishing process is a surface treatment technology. It is used to produce a mirror-finish on metal surfaces. During electropolishing, electrochemical anodic dissolution takes place on the surface of anode. In case of employing aluminium as the anode, following reactions carry out:



Since the dissolution rate at the anode is slowest during anodic dissolution, it controls the overall mechanism. The electrochemical reactions given above, are under diffusive mechanism due to which a layer is formed on the anode. As a result of the electrolyte used which mostly includes ethanol, this layer (double-layer) is viscous and has greater electrical resistivity (figure 2.11). Having a viscous layer with electrical resistivity enables controlled current flow. Current density on peaks (figure 2.11, β) is higher than that in crevices and holes (figure 2.11, α). Indeed, this difference causes the hilly spots dissolve faster. This mechanism leads to a surface-leveling effect, in the end producing a mirror like surface (Wernick, 1987; Adelkhani, 2009; Sulka, 2005).

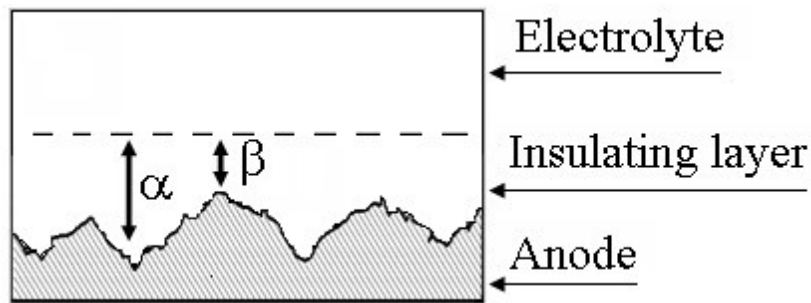


Figure 2.11: Double layer (Adelkhani, 2009)

Annealing was performed under different conditions such as at 500°C for 3h, at 400°C for 5h. Results of all were found satisfying. Sulka used a perchloric acid (60 wt %) and ethanol (abs.) mixture in a volumetric ratio of 1:4 for electropolishing. Perchloric acid was used to maintain the low pH so that Al ionizes into Al^{3+} and does not form oxides. He kept the current density constant at 500 mA.cm^{-1} and electropolished the surface for 1 min at 10°C while Korean research group and Lillo kept the potential constant at 20V for durations varying between 2-4 min. Paşaoğlu and Jiang et al. proposed another commercial, Cr free acid solution composed of phosphoric and sulfuric acid. In this electropolishing process, Al pieces were electropolished at $\sim 60^\circ\text{C}$ for 5-12 min at constant potential 17V. Electropolishing reaction is not accompanied by oxide formation. Surface smoothing efficiency is limited to coarser textures on the surface (Wernick, 1987; Sulka, 2005; Jiang, 2005; Lee, 2011; Lillo, 2008; Ma, 2009; Zaraska, 2010).

Figures 2.12 and 2.13 shows the obvious and significant effect of pretreatment on anodization of aluminium.

After producing well ordered porous AAO, pore diameter which is also the width of the tubes, can be adjusted by pore widening process. AAO is simply immersed in a solution which is capable of dissolving alumina. Pore widening can be done using various chemicals. An example which was frequently used in previous studies was 5 wt.% H_3PO_4 solution. It can be performed at various temperatures for different durations depending on the final pore diameter needed (Vojkuvka, 2007; Zhang, 2007).

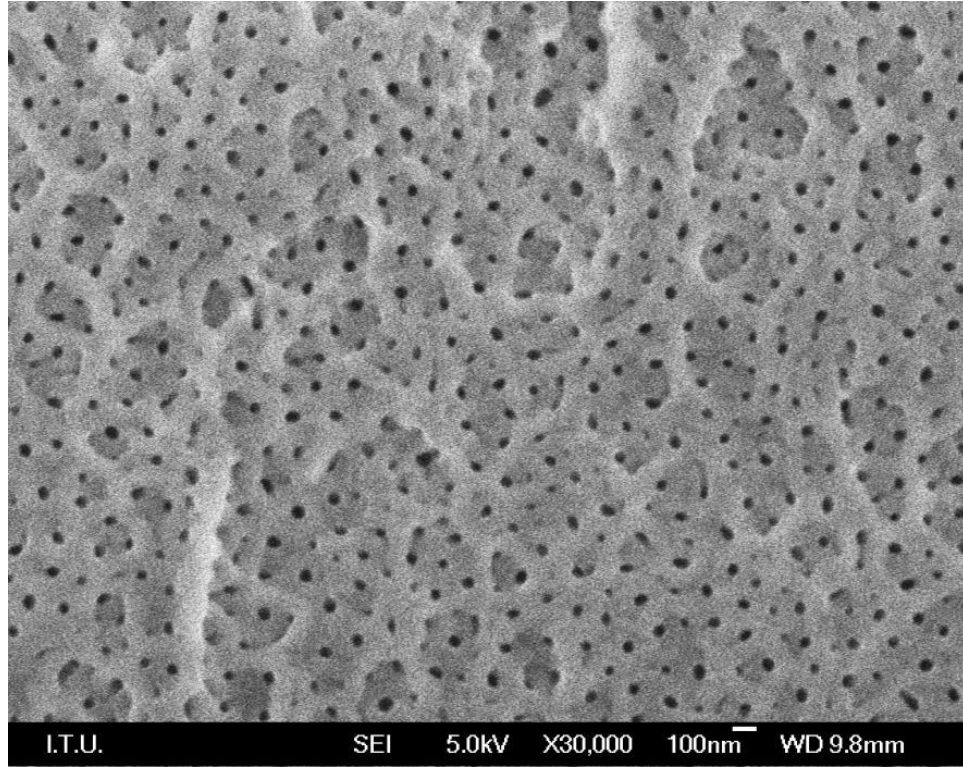


Figure 2.12: FEG-SEM image of AAO surface without electropolishing (Paşaoğlu, 2011)

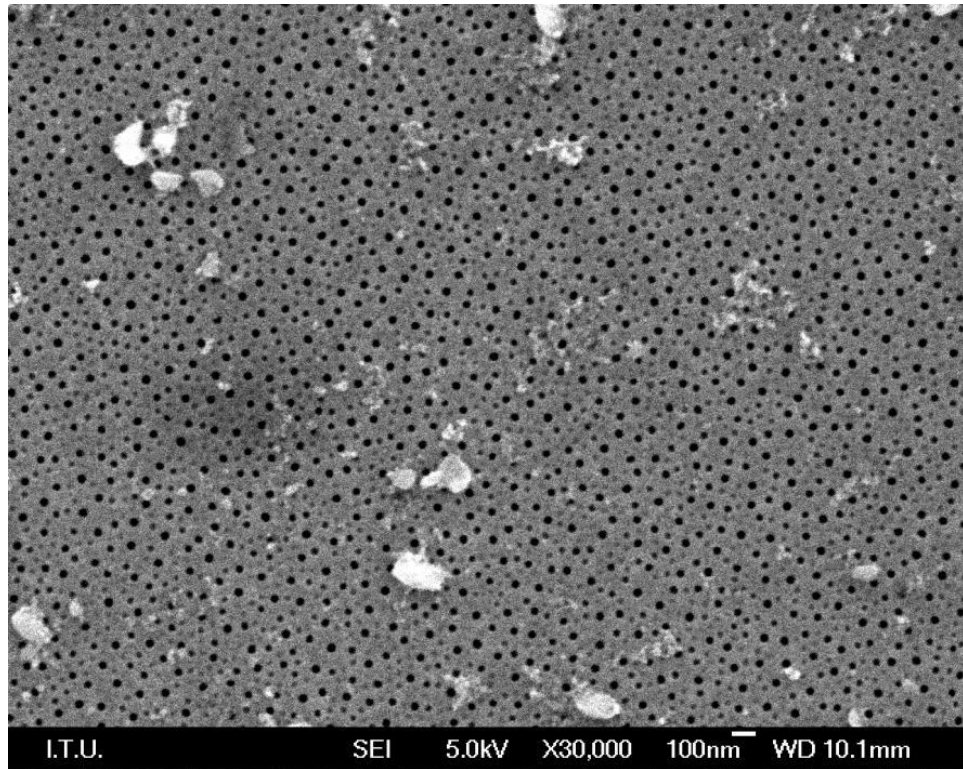


Figure 2.13: FEG-SEM image of AAO surface produced on electropolished aluminum (Paşaoğlu, 2011)

2.2.5.2 Pore widening and surface porosity

Vojkuvka et al. studied the change in pore diameter in relation with porosity. They produced AAO by two step anodizing in 0.3M oxalic acid and dipped the specimen (figure 2.14) in 5 wt.% H₃PO₄ for 10, 20, 30 and 40 min at room temperature. SEM Images of the surface after pore widening are given in figure 2.15(Vojkuvka, 2007).

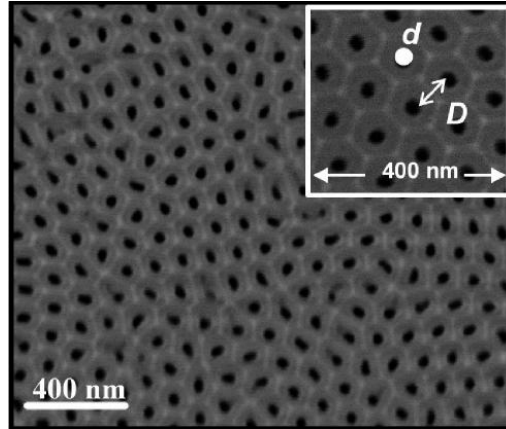


Figure 2.14: SEM image of specimen with ~30nm pore diameter(d) and ~95nm inter-pore distance(D) (Vojkuvka, 2007)

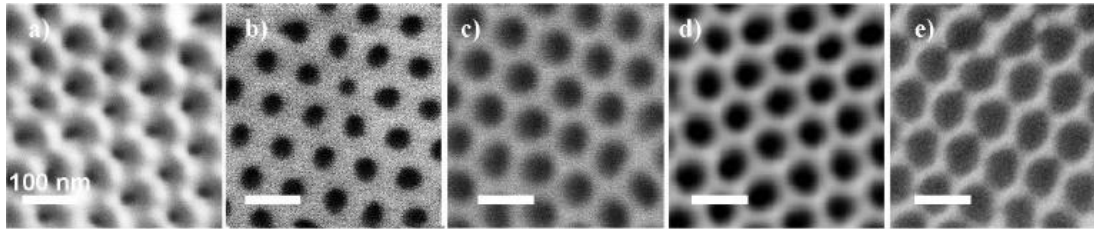


Figure 2.15: SEM images of AAO surface a) as-produced, b) after pore widening for 10 min, c) 20 min, d) 30 min, e) 40 min (Vojkuvka, 2007)

Inter-pore distance was constant for all samples and was approximately 100nm. Pore diameter increased with time from 30nm (as-produced) to 42nm, 52nm, 60nm and 70nm for samples etched for 10, 20, 30 and 40 min., respectively. Considering that the surface consisted of pores which are hexagonally ordered, porosity (P) was calculated with the following equation (Vojkuvka, 2007; Sulka, 2006):

$$P = \frac{2\pi}{\sqrt{3}} \times \left(\frac{d}{2D}\right)^2 \quad (2.10)$$

Calculated porosities were 8%, 15%, 21%, 33% and 46% for samples with pore diameters of 30nm, 42nm, 52nm, 60nm and 70nm respectively. Linear behaviours of pore widening time vs. porosity and pore diameter are shown in figure 2.16 (Vojkuvka, 2007).

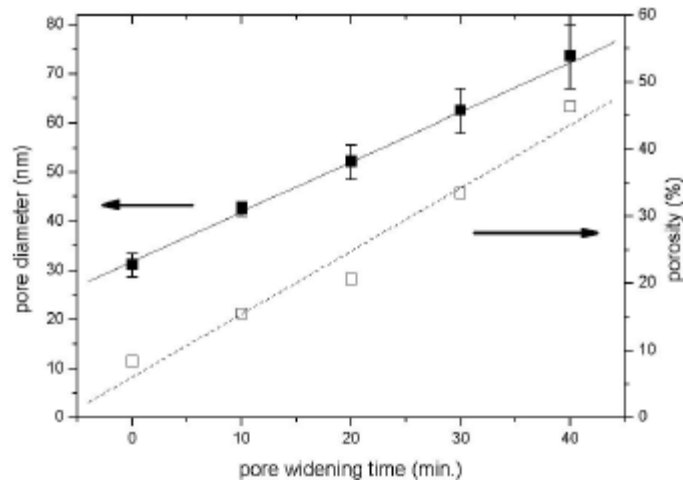


Figure 2.16: Pore diameter and porosity as a function of widening time (Vojkuvka, 2007)

According to the results of this study, it was found that pore widening took place almost with a linear behaviour. Although we have limits for the maximum pore diameter that can be obtained; by changing anodizing parameters in the beginning and with the help of pore widening, AAO with a huge variety of pore diameters can be produced.

2.3 Mechanical Properties of AAO

Based on the applied loads, the indentation hardness tests can be divided into macro-, micro- and nano hardness tests (figure 2.17).

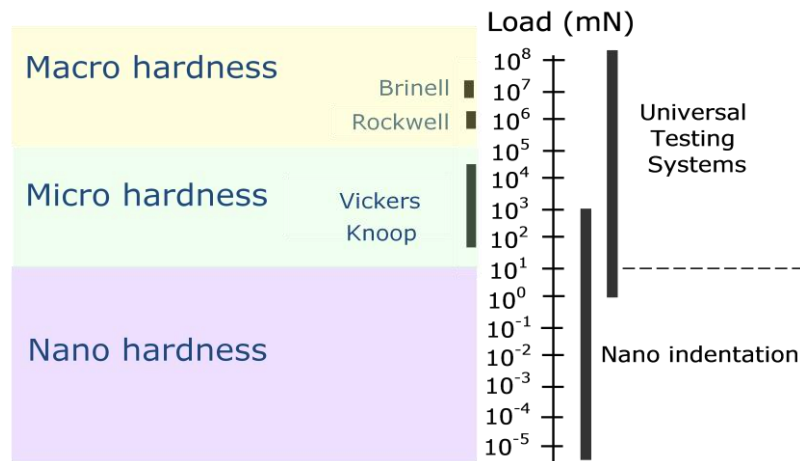


Figure 2.17: Loading ranges of hardness testing methods (De Wolf, 2011)

Among these, simplest and the state of the art method for measuring mechanical properties of nanostructured materials is indeed nanoindentation technique. It is especially designed for mechanical characterization of materials with small

dimensions since the penetration depth is measured in nanoscale rather than microns. Load applied can be quite low e.g. 1, 2 mN. Phase changes, air gaps, imperfections or impurities etc. can easily be noticed via this technique (Yang, 2008; Fischer, 2002; Url-1).

The unique feature and a big advantage of this technique is that it enables indirect, thus instant measurement of the contact area between the indenter and the specimen. Main drawback of this technique is observing the imprints as they are in nanoscale. To overcome this disadvantage, an indenter tip with a pre-known geometry is employed. During nanoindentation, loading-penetration depth curves are drawn which monitors whole indentation process. By analysing these graphs in relation with indenter tip's geometry, mechanical properties such as young's modulus, hardness, fracture toughness, stiffness and stress-strain can be calculated. Therefore, different indenter tips are used e.g. Berkovich, knoop and cube corner. Berkovich tip is the one which is mostly used (figure 2.18). Modified Berkovich indenter is designed to have the same ratio of projected area to indentation depth as the Vickers indenter (Yang, 2008; Fischer, 2002; Url-1).

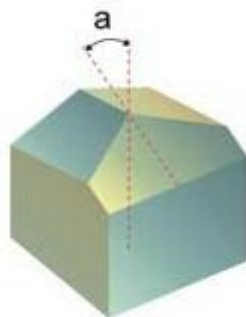


Figure 2.18: Berkovich indentation tip, $\alpha = 65.3^\circ$ (Url-1)

2.3.1 General Theory of nanoindentation

A load-penetration depth curve in an indentation test mostly consists of loading and unloading parts (figure 2.19a). Elastic-plastic deformation of the test material is included in loading curve. Unloading curve defines the elastic recovery of the material after load is released.

An important step to determine the hardness and elastic modulus of materials by analysing the load-penetration depth curves, is the calculation of the area of the indentation imprint under maximum load. There are two major parameters which

must be known to calculate the projected contact area. One is the geometry of the indenter. The other parameter is the contact depth at the peak load which we can easily read from the loading-penetration depth curve. Projected contact area is calculated by equation (2.11)(Fang, 2007; Ko, 2005; Fischer-Cripps, 2002),

$$A_c = f(h_c) \quad (2.11)$$

where h_c is the contact depth. For a berkovich indenter, the relationship between the projected contact area and contact depth is given by equation (2.12).

$$A_c = 24.5h_c^2 \quad (2.12)$$

Hardness is defined as the resistance to local deformation. It is expressed as the maximum indentation load, L_{max} , divided by the contact area, A_c which is given in equation (2.13).

$$H = \frac{L_{max}}{A_c} \quad (2.13)$$

The real contact area, A_c , differs according to the indentation tip used. Ko and others used a cube corner tip while Fang preferred a berkovich indenter with a radius of 200nm (Fang, 2007; Ko, 2005).

Loading and unloading graph, Load versus penetration depth is given in figure 2.19a. Figure 2.19b. shows crosssectional view of a sample after nanoindentation.

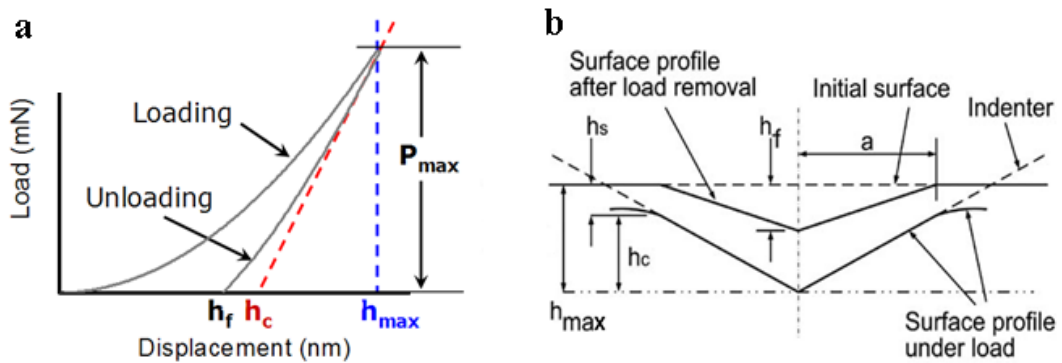


Figure 2.19:a) Load versus penetration depth for elastic-plastic loading followed by elastic unloading. h_c is the depth of the residual impression, h_f is the depth from the original specimen surface at load P_{max} , h_c is the elastic displacement during unloading. b) Crosssectional representation of the indentation process showing distances used for analysis (Fischer-Cripps, 2002; Ko, 2006).

According to the general theory of nanoindentation, with the projected area determined, elastic modulus of the material can be calculated by equation (2.14), (2.15) and (2.16) in case it is the value in the indentation direction.

$$\frac{1}{E_r} = \frac{1-\nu_s^2}{E_s} + \frac{1-\nu_i^2}{E_i} \quad (2.14)$$

$$S = \frac{dL}{dh} = \frac{2}{\sqrt{\pi}} \beta E_r \sqrt{A_c} \quad (2.15)$$

$$E_r = \frac{1}{\beta} \frac{\sqrt{\pi}}{2} \frac{S}{\sqrt{A_c}} \quad (2.16)$$

In formula (2.14) ν stands for the Poisson's ratio. Subscripts s and i are the specimen and the indenter tip respectively. In equations (2.15) and (2.16), E_r is the reduced elastic modulus, A_c stands for the real contact area, L for the load. h indicates the indentation depth and β is the indenter tip shape factor. For a diamond tip E_i is 1140 GPa and ν_i is 0.07. This calculation is based on characterization of a non-porous material with no stress. However, strains in other directions must be taken into consideration as for materials with porous structure or having tubes as in anodized aluminium oxide (Ko, 2005; Ko, 2006; Fang, 2007; Yang, 2008).

Loading-penetration depth curves indicate different types of properties as mentioned previously. figure 2.20 shows examples of behaviours those can be realised by examining these curves.

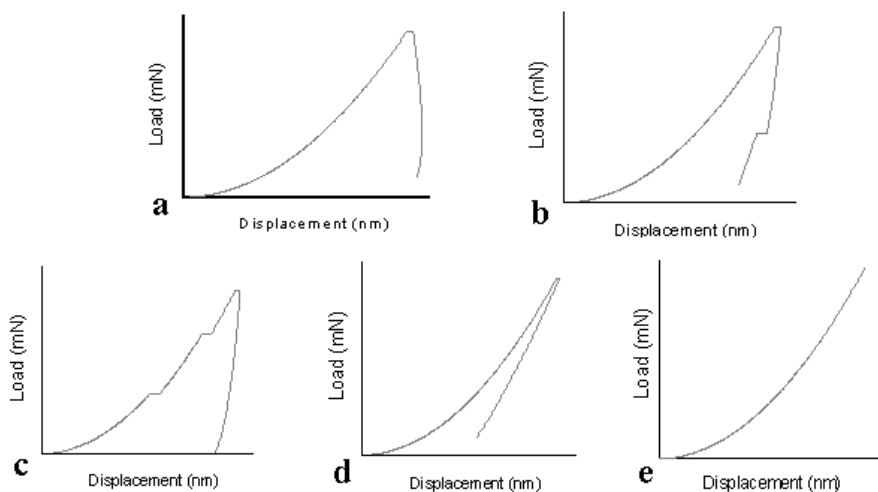


Figure 2.20: Examples of load-penetration depth curves a) Creep, b) Pop-out event, c) pop-in event, d) Elastic recovery, e) Full elastic recovery (De Wolf, 2011)

2.3.2 Characterization of mechanical properties of AAO by nanoindentation

Mechanical properties of AAO have been studied by various researchers in the last decade. Especially due to its use in micro electromechanical systems (MEMS) and nanocomposites produced by reinforcing AAO with different materials, investigation of AAO itself regarding its mechanical properties has gained attention.

Xia et al. investigated young's modulus and hardness of AAO membranes in 2004. Their research was focused on effect of residual stress on mechanical properties of AAO. In this research mechanical properties were characterized by nanoindentation and Vickers micro-indentation. AAO with 50-60nm pore diameter with 20 and 90 micrometer thicknesses were produced. Loads chosen for cube-cornered nanoindentation were 20-650 mN while for Vickers micro-indentation load applied was 500g. Samples were tested before and after heat treatment at 650°C. It was seen that heat treatment did not affect the Young's modulus while it increased the hardness of alumina with the mentioned pore diameter from 5.2GPa to 6.3GPa.

Another study which was quite similar with that of Xia et al., was made by Ko and colleagues. They investigated the effect of residual stress on mechanical properties in relation with porosity percentage. Pore diameters and porosity percentage of samples are given in Table 2.4.

Table 2.4: Porosity percentages of samples (Xia, 2006)

Pore diameter of samples (nm)	Porosity(%)
30	8
40	15
50	23
60	33
70	44
80	58

Nanoindentation was performed on as-produced samples as well as those heat treated at 500°C. Change in mechanical properties with heat treatment is given in figure 2.20 (2006).

Heat treatment did not change elastic modulus effectively (figure 2.22a). However, an increase in hardness was observed (figure 2.21b). It was noticed that with increase in porosity, both properties showed a rather linear decrease. Ko's results were in agreement with Xia et al. It must be noted that the results presented are raw data obtained directly from the test machines and can be considered as qualitative values as the hardness measuring method did not take the effect of porosity into consideration. Modifications in the measuring method is discussed by Ng et al. later (2006).

Mechanical response and deformation behaviour was also investigated by Fang et al. in 2007 and 2008. They realised a sudden drop off of the indentation load on the loading curve (figure 2.22a) around 300-400nm which represents a pop-in behaviour. According to their opinion, this pop-in response is because the nanopore walls crash and collide with one another. SEM image of nanoindentation imprint is given in figure 2.22b. Pop-in is indicated with a circle in figure 2.22a.

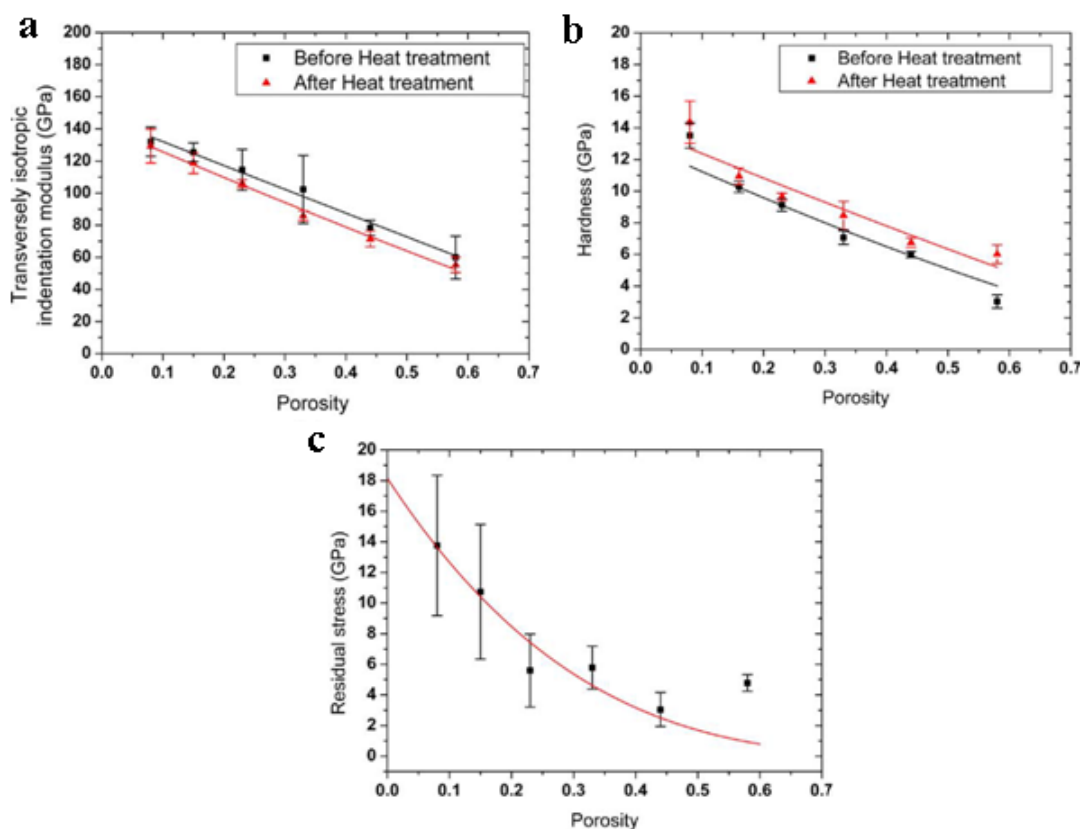


Figure 2.21: a) Transversely isotropic indentation modulus, b) hardness, c) residual stress as a function of sample porosity before and after heat treatment (Ko, 2006)

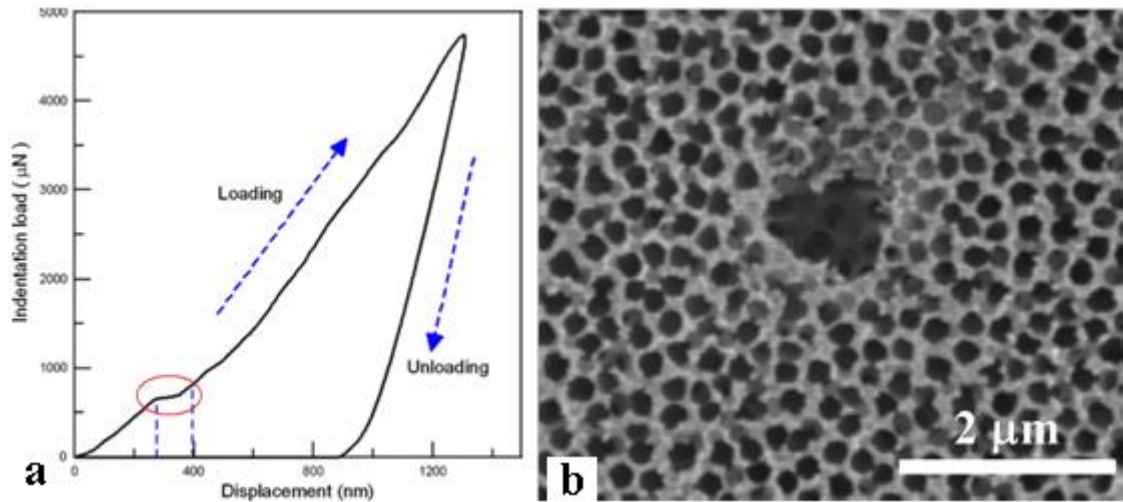


Figure 2.22: a) Load–displacement curve of AAO and b) SEM image of the nanoindentation imprint on AAO using a Berkovich indenter (Fang, 2008)

Ng et al. revealed crack formation during nanoindentation on well-ordered nanoporous AAO. They used 0.3M oxalic acid for the synthesis of $\sim 106\mu\text{m}$ thick alumina on pure aluminium with $\sim 70\text{nm}$ pore diameter. For mechanical characterization, Berkovich tips were employed during nanoindentation. Various maximum loads, namely 0.1, 0.5, 1, 3, 6, 10, 20, 40, 60 and 80 mN were used at fixed 1.5 mN min^{-1} loading rate. To see the effect of loading rate, they also used different loading rates of 0.5, 5 and 50 mN min^{-1} at 120 mN maximum load. Once the loading reached its peak value, it was maintained for 1 min followed by a reduction to 10% of the preset maximum load at an unloading rate of 40 mN min^{-1} . Load was held at the 10% value for 1 more min and eventually complete unloading was performed (2009).

Data they obtained for the hardness at 120mN peak load, is given in table 2.5. Since Oliver-Pharr method is accounted for bulk materials with solid continuum, so-called true hardness must be calculated by taking the actual contact area into consideration. They measured the real contact area from the SEM image of the imprint. The estimated solid area was 55.4%. Table 2.5 also shows the true hardness values of AAO at 120mN max. load and various loading rates. Although Oliver-Pharr method showed a decrease in hardness values with increasing loading rate (table 2.5), actual hardness calculated was rather steady, regardless of the loading rate. This difference showed that the Oliver-Pharr method was not satisfying for hardness measurements of porous materials.

Table 2.5: Comparison of hardness by Oliver-Pharr method and true hardness (Ng, 2009)

Applied max load	120 mN	
Applied loading rate (mN min ⁻¹)	0.5	5
Apparent hardness (MPa) (measured by Oliver-Pharr method) Apparent contact area (load/ apparent hardness)	162 ± 9 (743 ± 41 μm ²)	146 ± 14 (829 ± 79 μm ²)
Apparent hardness (MPa) (measured from the gross area of the residual indent as imaged by SEM)	120 ± 5 (998 ± 41 μm ²)	118 ± 3 (1013 ± 30 μm ²)
True hardness (MPa), (measured from the true solid area of the residual indent, with solid area ratio of 55.4%, as imaged by SEM)	217 ± 9 (553 ± 23 μm ²)	214 ± 6 (561 ± 16 μm ²)
Unloading stiffness (mN nm ⁻¹)	0.584 ± 0.005	0.492 ± 0.010

As mentioned previously, the interesting point they came across was the crack formation within the imprint without any noticeable pile-up or sink-in behaviour (figure 2.23). They named these cracks as median and bilinear cracks. Median crack system had three cracks starting from the bottom of the imprint, going along the median lines of the triangular indent while bilinear cracks occurred on each of the sloping surfaces (figure 2.23a).

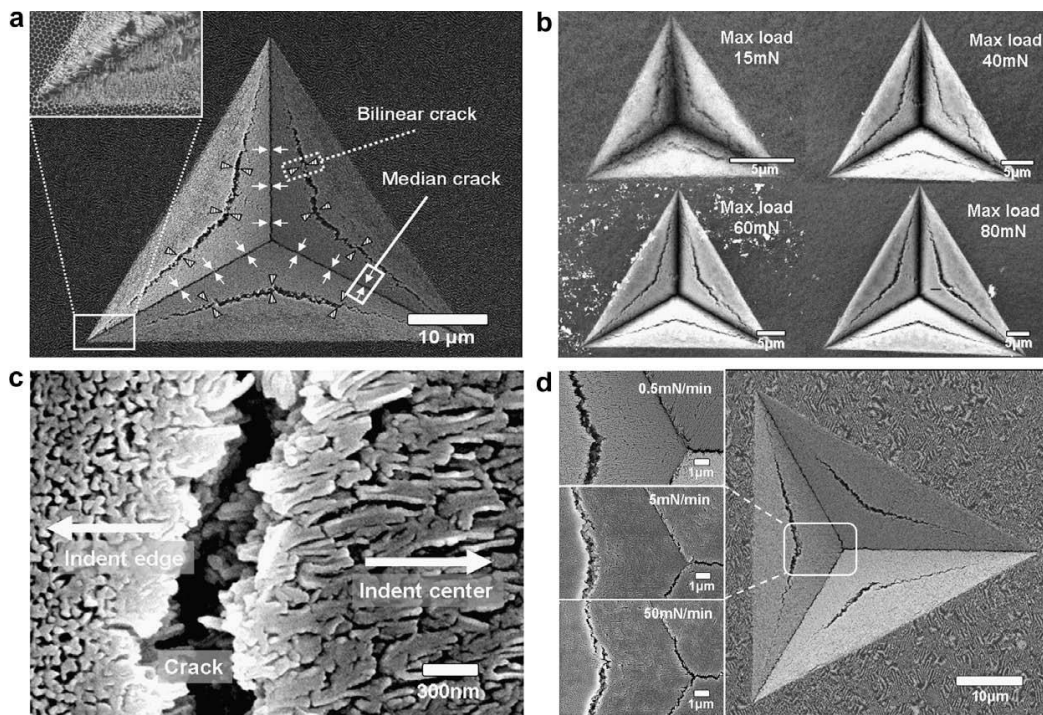


Figure 2.23:a) Top-view SEM images of the Berkovich indent revealing two systems of cracks. Maximum load 120mN, loading rate 1.5 mN min⁻¹ and unloading rate 40 mN min⁻¹. b) Comparison of Berkovich indents made at increasing peak loads with a loading rate of 1.5 mN min⁻¹, showing similarity between the crack systems. c) High magnification SEM image of a bilinear crack d) Magnified views of cracks formed during indentations with different loading rates as 0.5, 5 and 50 mN min⁻¹ from top to bottom respectively (Ng, 2009).

Median cracks were already expected to be formed on contact lines of the indenter tip with AAO. Bilinear cracks on the other hand, were unexpected which were suggested to have occurred and propagated during loading, because of internal

residual stress. The width of the bilinear cracks was affected by loading rate. The higher the loading rate was, the narrower the cracks were. SEM images (both top and cross sectional view) showed that both crack formations were locally effective and had very sharp elastoplastic boundaries (Ng, 2009).

In another research made in 2009, AAO with a pore diameter of $\sim 20\text{nm}$ and $\sim 80\mu\text{m}$ thickness was filled with carbon nanofibres and changes in mechanical behaviour by this reinforcement were investigated using a nanoindenter, equipped with a berkovich tip. Commercially available AAO with 200nm pore diameter was also filled and characterized for comparison. Loading-Unloading curves were analyzed with the procedure developed by Oliver and Pharr which was found weak to analyze porous materials by Ng et al (Kothari, 2009).

The hardness and elastic modulus values of AAO with empty tubes, are somewhat in agreement with those reported by Xia et al previously (2004). As Kothari used 5657 Al alloy instead of high purity Al, composition of the oxide was likely to have effects on differences in results. Looking at the SEM images of indentation imprints on reinforced commercial AAO with 200nm pore diameter, crack propagation with a starting point at the corners of the triangular imprint was easily recognised (figure 2.24a). This behaviour was different than that Ng et al. showed in 2009. No bilinear cracks were observed. Pile-up behaviour was apparent on reinforced AAO produced in laboratory with 20nm pore diameter (figure 2.24c). Indeed, the existence of carbon within AAO was the main reason behind the difference in results (Kothari, 2009).

A noticeable difference between reinforced AAOs in relation to their pore diameters (20 and 200nm), was the absence of crack formation shown in Fig 2.24c. Although maximum load was 3N , AAO didn't shatter while reinforced AAO (200nm pore diameter) cracked under 400mN normal load (Fig 2.24a)(Kothari, 2009).

Fundamentally, homogenous and heterogeneous ceramics behave in different ways against normal loading. Homogenous ceramics respond to the intense confined shear under the sharp indenter tip by anelastic deformation. And as a result of elastic and anelastic deformation mismatch, radial cracks occur and propagate. As for heterogeneous ceramics, it is known that they also undergo anelastic deformation. But if they are weak enough in shear, it is very likely that they might suppress formation of long cracks which was the case for reinforced AAO with 20nm pore

diameter (Fig2.24c). This pore diameter-dependant behaviour of reinforced AAO could present new applications for ceramic composites (Kothari, 2009)

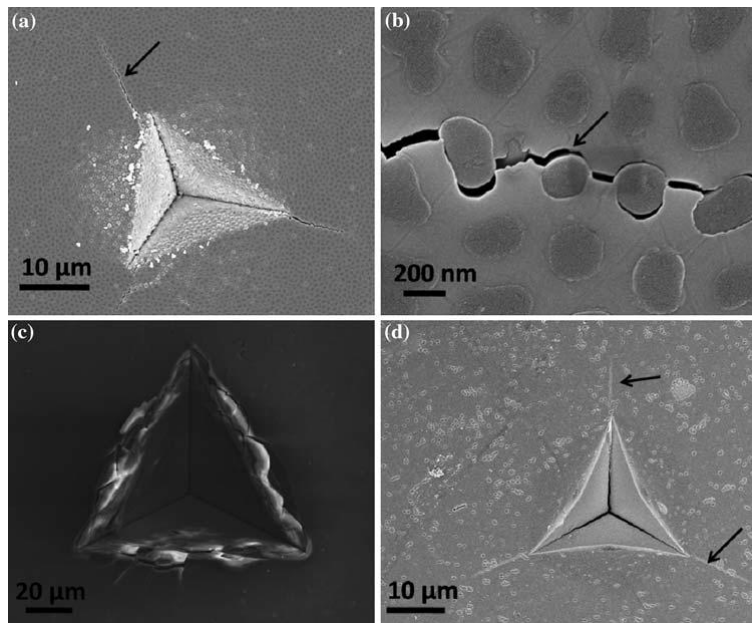


Figure 2.24:a) Indentation imprint on reinforced AAO with 200nm pore diameter under 400mN load, b)High-mag. of the crack indicated with the arrow in (a), c)SEM image of reinforced AAO with a pore diameter of 20nm, pile-up on the edges of the imprint, absence of cracks emanating from residual indent impression, d)cracks emanating from the residual indent impression on AAO (Kothari, 2009)

2.4 Tribological Properties and Wear Behaviour of AAO

2.4.1 Tribology and wear

Tribology is derived from the Greek word “tribos” which means rubbing or sliding. It is a branch of science which focuses on friction, wear and lubrication of surfaces in interaction. Main goals of tribology are reduction of material wear and increasing lifetime of materials in return, controlling or optimizing friction according to area of application. Wear can be described as wastage or loss of material due to any sort of effect. Friction is expressed as the resistance to relative motion of surfaces, fluid layers or any type of material sliding against each other and lubrication is the process or technique to reduce friction and to control wear by adding lubricants (Takadoun, 2008; Stachowiak, 2001).

During sliding, either of the surfaces in contact can be worn in different mechanisms. 4 major wear mechanisms are abrasive, adhesive, erosive and corrosive wear. In the

previous researches, abrasive and adhesive wear could be seen on AAO (Baxi, 2008; Kim, 2010; Lee, 2011).

Abrasive wear which can be very rapid, occurs in case either of the interacting surfaces is harder than the other (figure 2.25). This type of wear can cause scratches or/and wear grooves. Abrasive wear has sub-mechanisms namely ploughing (figure 2.25a), cutting (figure 2.25b) and cracking (figure 2.25c). If the softer material is shifted to the sides of the wear groove, it is called as ploughing in case of which material is not removed from the surface. Cutting occurs material is removed from the surface in a volume equal to the volume of the wear track. In case the material cracks in the subsurface surrounding the wear track, the sub-mechanism is called cracking (Takadom, 2008; Stachowiak, 2001, Url-5).

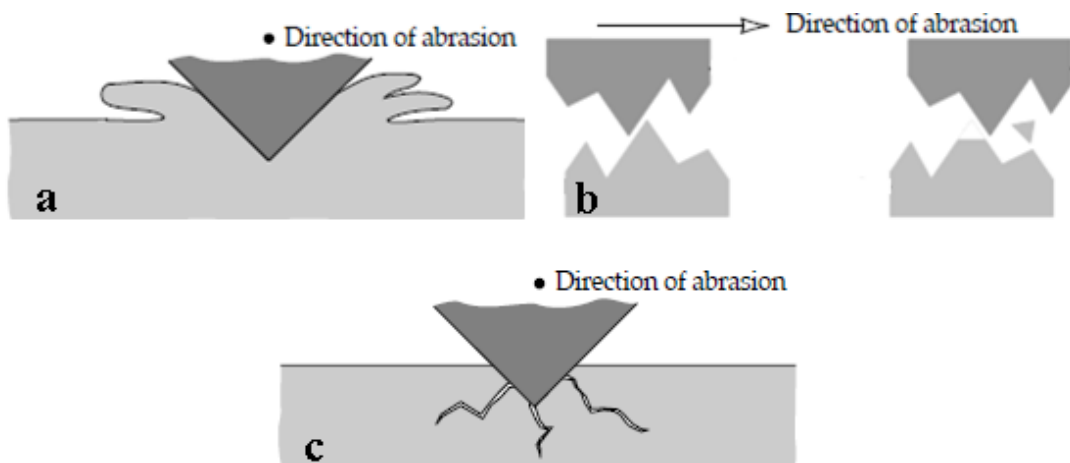


Figure 2.25: Sub-mechanisms of abrasive wear a)Ploughing, b)Cutting, c)Cracking (Stachowiak, 2001; Url-5)

Adhesive wear can be realised by microwelds or joints between the surfaces subjected to friction. Some of the material is transferred to the counterbody (figure 2.26). Adhesive wear may even prevent sliding motion due to high adhesion between two bodies which causes high friction.

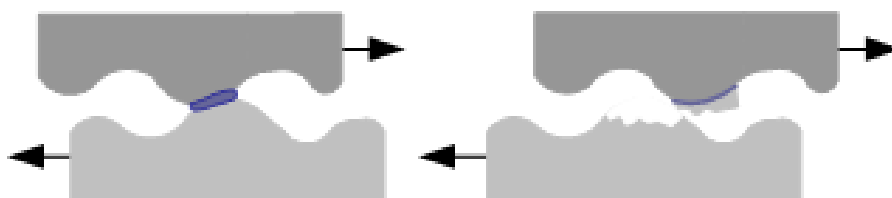


Figure 2.26:Adhesive wear (Url-5)

2.4.1.1 Fretting

Fretting is one of the tribological processes used for the characterization of a material. It is basically described as a relative cyclic motion between two oscillating bodies. The amplitude of the motion is in micrometer or even nanometer scale (Url-1; Suciu, 2010).

Fretting hysteresis loops are obtained during the tests which give us information about the wear mechanism and frictional force. Shape of the loops represent fretting regimes. Coefficient of friction can be calculated from the tangential force. 4 fretting regimes are full stick regime, partial slip regime, gross slip regime and reciprocating sliding regime. At full stick regime, the counterbody sticks on the surface of the sample forming a straight line instead of a loop (figure 2.27a). In case of partial slip, some parts of the contact perform relative motion while other parts do not move due to adhesion. Hysteresis loops such as shown in figure 2.27b can be obtained when partial slip occurs. Hysteresis loop of a gross slip is illustrated in figure 2.27c. Gross slip occurs when the amplitude of fretting increases due to which relative motion takes place. If the displacement exceeds contact dimensions, it means that the relative motion is in reciprocating sliding regime, hysteresis loop of which is given in figure 2.27d (Gallego, 2007; Suciu, 2010).

Area of the a hysteresis loop gives the energy dissipation due to friction. Since there is no relative motion in full stick, no energy dissipation is present. From full stick towards reciprocating sliding regime, relative motion increases which in return increases the energy dissipation as a result of friction (Fouvri, 1997).

Full stick regime reveals an elastic deformation on the bodies in contact. Partial slip causes increment the stress making crack propagation very likely. In case of gross slip, damage is more severe and causes wear on the surfaces. Due to very short displacement, wear particles (debris) generally stays on the surface. Reciprocating sliding piles up the wear particles and pushes them either to each end of the wear track or to the sides. By taking these into consideration, hysteresis loops can be correlated with the wear mechanism and type of fretting (Suciu, 2010).

For a better understanding of the hysteresis loops, slip ratio, s , can be used. Slip ratio is the ratio of displacement to the actual sliding distance. It varies between 0 and 1. Table 2.6 shows the relation between s and fretting regimes (Url-7; Suciu, 2010).

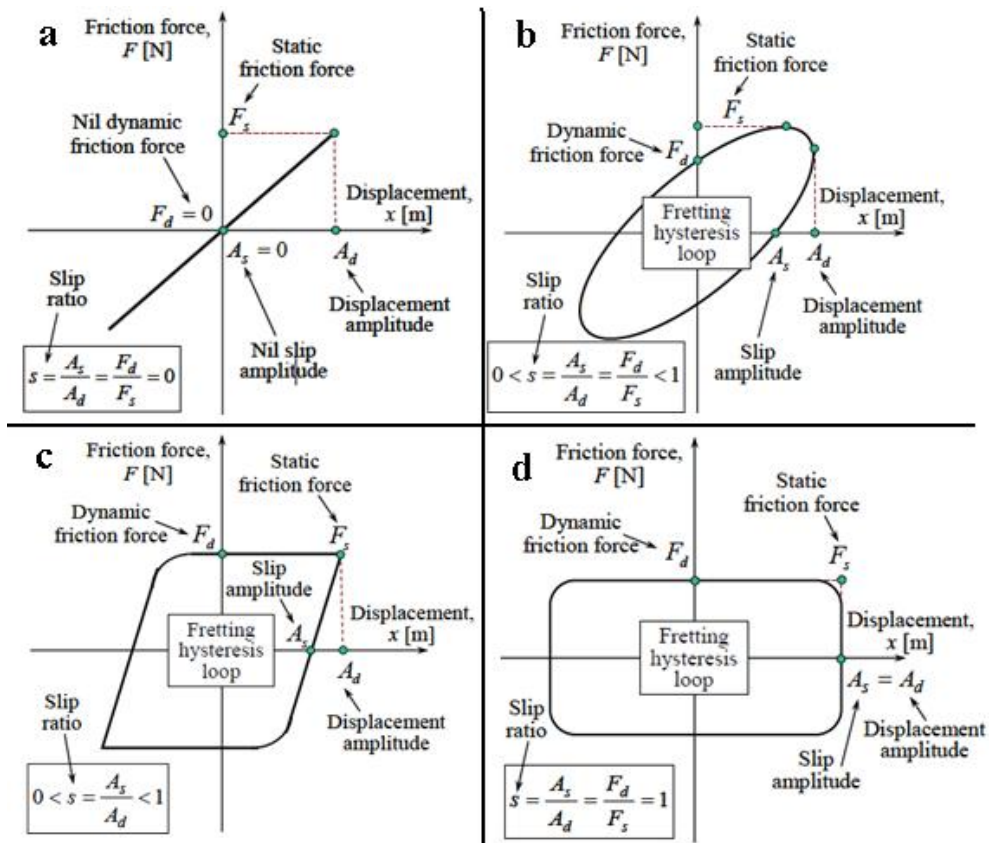


Figure 2.27: Fretting Regimes a) Full stick regime, b)partial slip regime, c)gross slip regime, d)reciprocating sliding regime (Suciu, 2010)

Table 2.6: Slip ratio – Friction regimes (Suciu, 2010)

Slip ratio, s	Friction regime
$s=0$	Stick
$0 < s < 0.17$	Partial slip
$0.17 < s < 0.38$	Transition from partial to gross slip
$0.38 < s < 0.95$	Gross slip
$0.95 < s < 0.955$	Transition from gross slip to reciprocating sliding
$0.955 < s < 1$	Reciprocating sliding

2.4.2 Tribological behaviour of non-porous AAO

Baxi investigated the wear behaviour of non-porous micro arc oxidized AAO coated on aluminium considering its use in biomaterials in human body. 3 samples were produced using an AC power supply at 3 current densities as 0.100, 0.125 and 0.150 A/cm². She employed a ball-on-disk tribometer (CSM Instruments) with silicon nitride ball (6 mm diameter). AAO coated disks were reciprocated at a linear speed

of 2.5 cm/s. Wear track was 6mm long. Tests were run at 5 N normal load for 8 hours at 25°C (2008).

Coefficient of friction (COF) for the sample produced at a current density of 0.100A/cm² was 0.349 in the beginning which in the end dropped down to 0.192. For the one produced at 0.125 A/cm², maximum friction coefficient was 0.246 followed by a decrease to 0.175. Last specimen (0.150 A/cm²) had a maximum coefficient of friction value of 0.243 while it was 0.167 at the end of the tests. Curves involving these results are given in figure 2.28 (Baxi, 2008).

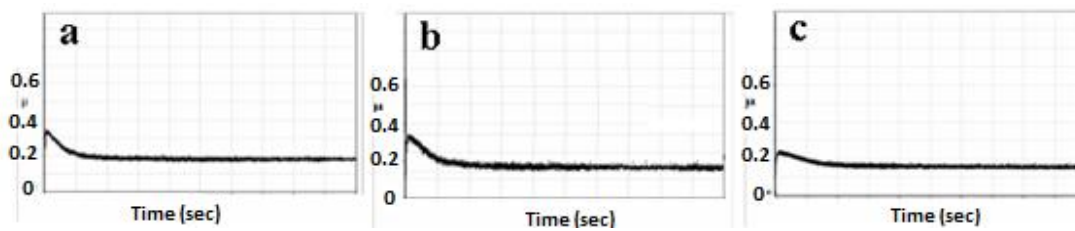


Figure 2.28: COF values for samples produced at a current density of a)0.100 A/cm², b)0.125 A/cm², c)0.150 A/cm² (Baxi, 2008)

Running in (period until COF reaches a steady state) was present in all tests. COF had high values in the beginning but then decreased to lower values and became constant with time. These high values are linked to the high surface roughness. As easily recognised, with increasing current density, less COF was obtained. This was due to the presence of different phases (α -Al₂O₃ and γ - Al₂O₃) within the coating itself which resulted in higher density and hardness. Amounts of the phases were dependent on current density and time. 0.150 A/cm² had both phases while 0.125 a/cm² had only gamma phase. 0.100 A/cm² had neither of the phases which had the highest COF among all. As for the wear mechanism, ploughing effect was observed as well as few cracks in wear tracks. This indicated that the mechanism was abrasive wear with micro fractures. No tribochemical reactions were observed. (Baxi, 2008).

In another study, tribological properties of magnetron sputtered AAO with different ratios of alpha alumina : gamma alumina, were investigated with the same method. Normal load applied was 0.25 N and linear turning speed was kept constant at 0.02 m/s. Counterbody was a steel ball with 6mm diameter. COF values measured (varying between 0.4 and 0.95) depending on phase ratios were higher than Baxi's results. This difference can be linked to coating conditions and test parameters.

Despite the numerical difference in values, the conclusion was the same. Alpha phase alumina had lower COF (Aryasomayajula, 2008).

2.4.3 Tribological characterization of porous AAO

Studies regarding wear behaviour of both filled-in and as-produced AAO under dry or lubricant-added conditions were carried out by various research groups. As mentioned previously, porous AAO is potentially advantageous as lubricant reservoir since the pores can be filled with other materials. Although preliminary studies were done on filled-in AAO, lack of information motivated researchers to investigate the wear behaviour of as-produced AAO to reveal the effect of these fillings.

Skeldon et al. studied on formation of MoS₂ precursor films on anodized aluminium in terms of film morphology, composition and basic mechanical properties (1996). Method used for precipitating MoS₂ was re-anodizing porous AAO in an appropriate electrolyte which results in no significant change in the thickness of the oxide film. figure 2.29 illustrates the precipitating model of solid lubricant.

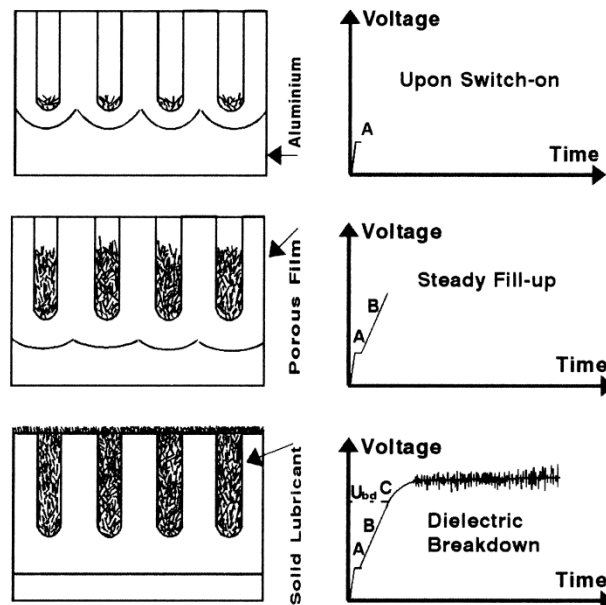


Figure 2.29: Illustration of solid lubricant precipitation within and over the porous film (Skeldon, 1996)

As they reported, wear coefficients measured from pin-on-flat tests, for aluminium are $3.5 \times 10^{-10} \text{ m}^2$ without any self-lubricating film and $4 \times 10^{-12} \text{ m}^2$ in the presence of such film. Obviously, self-lubricating film improved wear properties (Skeldon, 1996)

Maejima et al. reported impregnation of molybdenum sulfide compounds in porous AAO to investigate tribological properties (2000). A similar approach was reported by Takaya et al. They impregnated iodine compound within the tubes of AAO (2003). Instead of pure aluminium, aluminium alloys (A1050 and A6061, respectively) were anodized in both studies. After tribological characterization of both impregnated and as-produced samples using a ball-on-disk type fretting machine with 5mm balls as counterbodies (94% Wc and 6%Co; and SUJ2 bearing steel, respectively), it was noticed that impregnated oxide films had lower COF (figure 2.30).

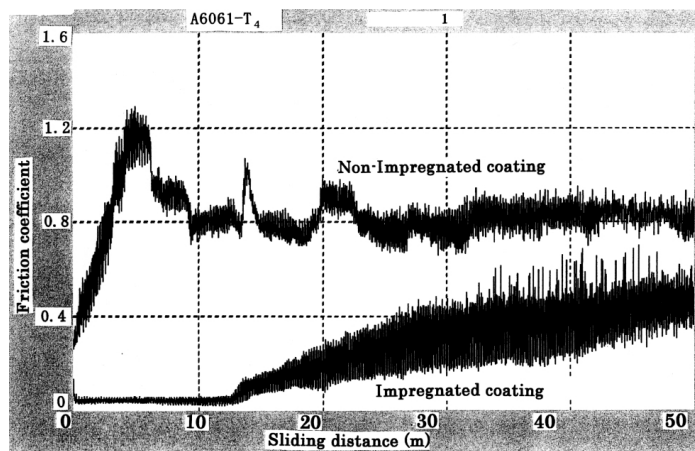


Figure 2.30: Evolution of COF on anodized A6061-T₄ alloy with and without impregnation with iodine compound (Takaya, 2003)

Jiang et al. studied frictional properties of AAO after infiltrating mineral oil in the pores. High COF values of as-produced AAO were reported previously. This study showed how COF changes by adding mineral oil as a lubricant. They produced well-ordered nanoporous AAO in oxalic acid and following anodization, pores were widened in phosphoric acid solution. As-prepared AAO was dipped into mineral oil at 17°C for 36h and the oil was infiltrated in the pores. Friction tests were carried out following scratch tests. Tribotester used was a ball-on-disk test machine equipped with a 3mm steel ball (GCr15). Normal loads varied between 490 and 2950mN with velocities between 0.1 and 0.5m/s. figure 2.31a shows evolution of COF with fretting cycles under 980mN normal load with 0.2m/s sliding velocity. As for as-produced AAO, COF showed a quite unstable behaviour with sharp deflection while for oil infiltrated AAO, COF values fluctuated less. Oil infiltration had significant effects on frictional properties. Mean COF values of oil infiltrated AAO under various normal loads vs. sliding velocity are given in figure 2.31b(Jiang, 2005).

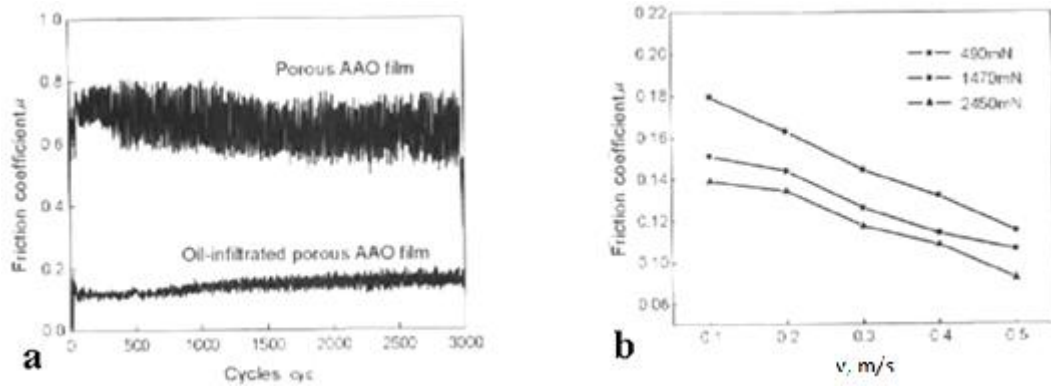


Figure 2.31: a) Evolution of COF of as-produced and oil infiltrated AAO, b) variation of mean COF of oil infiltrated AAO vs. sliding velocity (Jiang, 2005)

Oil was suggested to be squeezed out of the pores upon loading, forming a slippery layer between the counterbody and the surface of AAO. SEM images of wear tracks of both as-produced and oil infiltrated AAO are given in figure 2.32. It could be clearly seen that wear track of as-produced AAO has grooves and flakes. But the wear track on oil infiltrated samples was obviously smoother. Indeed mineral oil infiltration in porous AAO could reduce COF improving the wear resistance (Jiang, 2005).

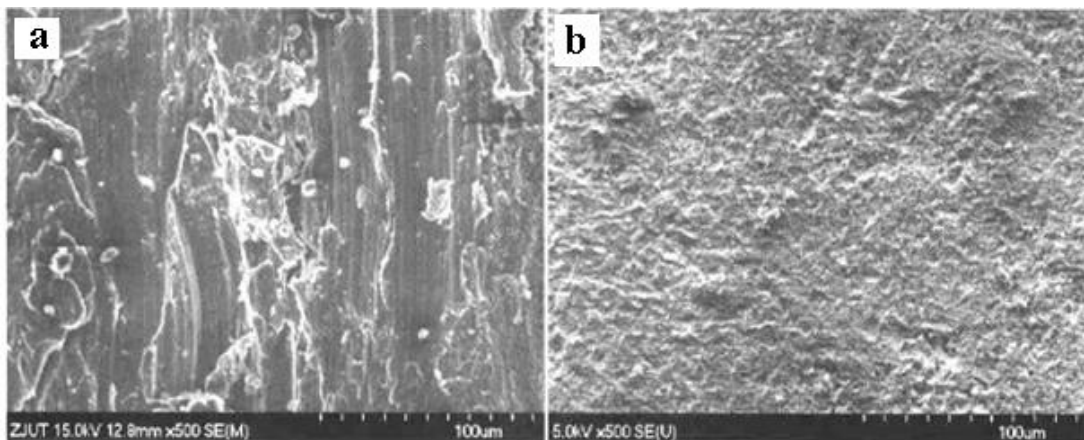


Figure 2.32: SEM images of wear tracks formed under 980mN normal load with 0.2m/s velocity on a) as-prepared AAO, b) oil-infiltrated AAO (Jiang, 2005)

Lee et al. carried out a similar work with that of Jiang and his colleagues. They produced AAO with 50nm, 260nm and 470nm pore diameters which corresponded to porosities 10-15%, 25-30% and 45-50%, respectively (figure 2.33) and used them as a reservoir for distilled water to discuss changes in friction properties.

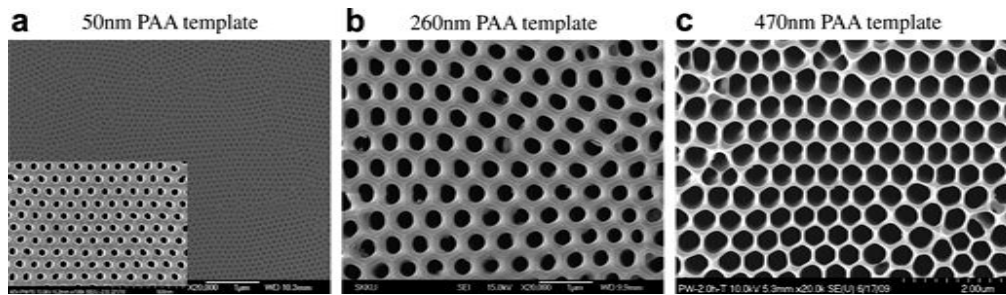


Figure 2.33: Porous Anodic Alumina (PAA) with a pore diameter of a)50nm, b)260nm, c)470nm (Lee, 2011)

Friction tests were performed with ball-on-disk type machine, against a counterbody made of AISI52100 bearing steel with a pore diameter of 6mm, under 4.55N normal load for dry condition (condition 1) and 3.58 N for watery conditions. Watery conditions were described as running tests with water lubrication after immersing AAO in distilled water for 30min (condition 2) and without water lubrication after submerging in distilled water for 30min (condition 3). According to the curves obtained from the tests (figure 2.34), it was clearly seen that water had a lubricious effect, lowering COF.

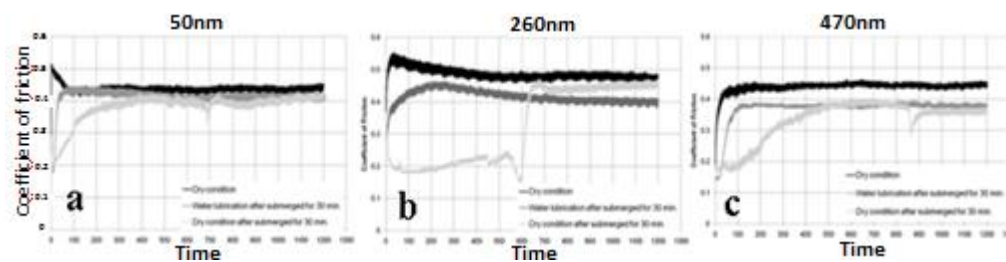


Figure 2.34: Evolution of COF on AAO with a pore diameter of a)50nm, b)260nm and c)470nm. Black curves indicate condition 1, dark grey: condition 2 and light grey: condition 3

All the tests confirmed that dry conditions had the highest COF values. Although the difference was slightly less, distilled water lowered COF. It could be seen that after about 600 sec, condition 2 and 3 had approximately same COF values despite the fact that there was no water lubricant added in condition 2. This was linked to the water release from the pores which formed a lubricious layer between the surface and the counterbody illustrated in figure 2.35. Similar mechanism could also be possible for oil infiltrated condition studied by Jiang et al. in 2005 (Lee, 2011).

Kim et al. studied wear behaviour of AAO only under dry conditions by reciprocating fretting tests without any additives as lubricant (2010).

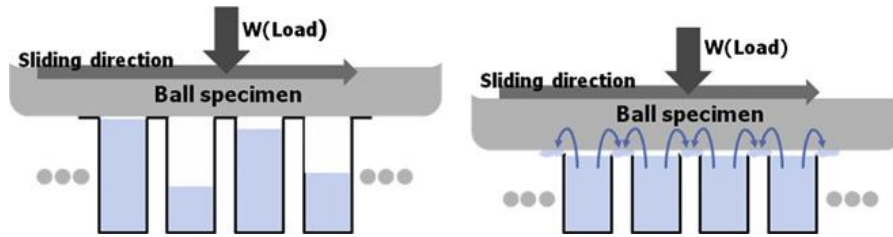


Figure 2.35: Illustration of releasing mechanism of water (Lee, 2011)

They investigated frictional behaviour of AAO in relation to the pore diameter (28nm, 45nm, 95nm and 200nm) by keeping porosity percentage approximately the same (~9%) for all samples they produced in various baths. They employed a 1 mm diameter 440C stainless steel ball as the counterbody with 4 different loads namely 1mN, 10mN, 100mN and 1N. Stroke length was 3mm and the counterbody reciprocated at 0.5 mm/s during 100 cycles. Evolution of COF under 10mN load and COF of samples with various pore diameters is given in figure 2.36. COF of pore-free surface was the same as Baxi reported in 2008 (Kim, 2010).

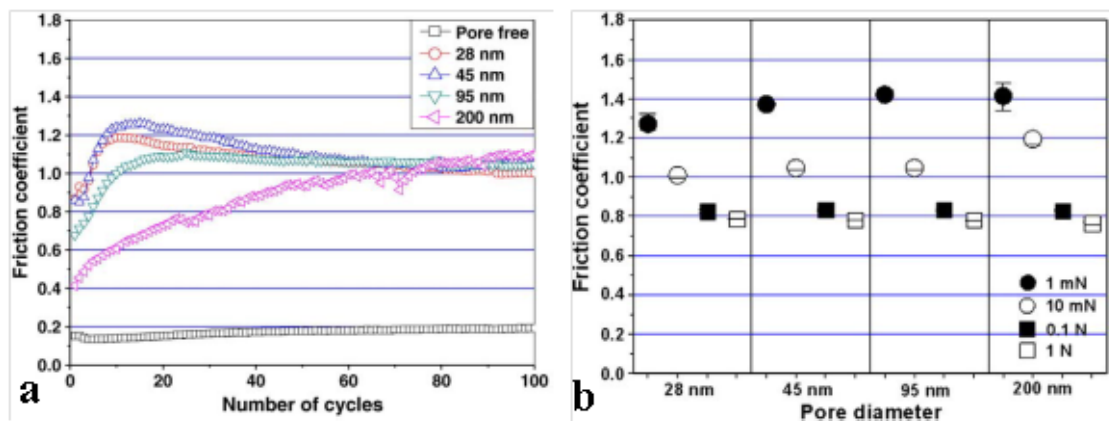


Figure 2.36: a) Evolution of COF with fretting cycles under 10mN load, b) COF of nanoporous AAO at various loads in relation to the pore diameter (Kim, 2010)

A running in period was present in the previous works reported (figure 2.30 and figure 2.34). Likewise, in this study, running in was followed by a steady state during which COF was approximately the same for all samples. COF values varied according to load applied. A considerable reduction of COF with the increase of load was noticed. Pore diameter did not have significant effects on the results (Kim, 2010).

SEM investigation of wear tracks (figure 2.37) revealed the wear mechanism which could be considered as abrasive wear. It was observed that the surfaces were covered

with thin layers which got thicker by increasing load. AAO had ignorable damage as can be seen in wear tracks formed under 1mN load. Pores were still visible after fretting tests at 1 and 10mN normal loads while those under 100 and 1000mN had agglomerated debris particles forming a layer covering the pores underneath making them invisible (Kim, 2010).

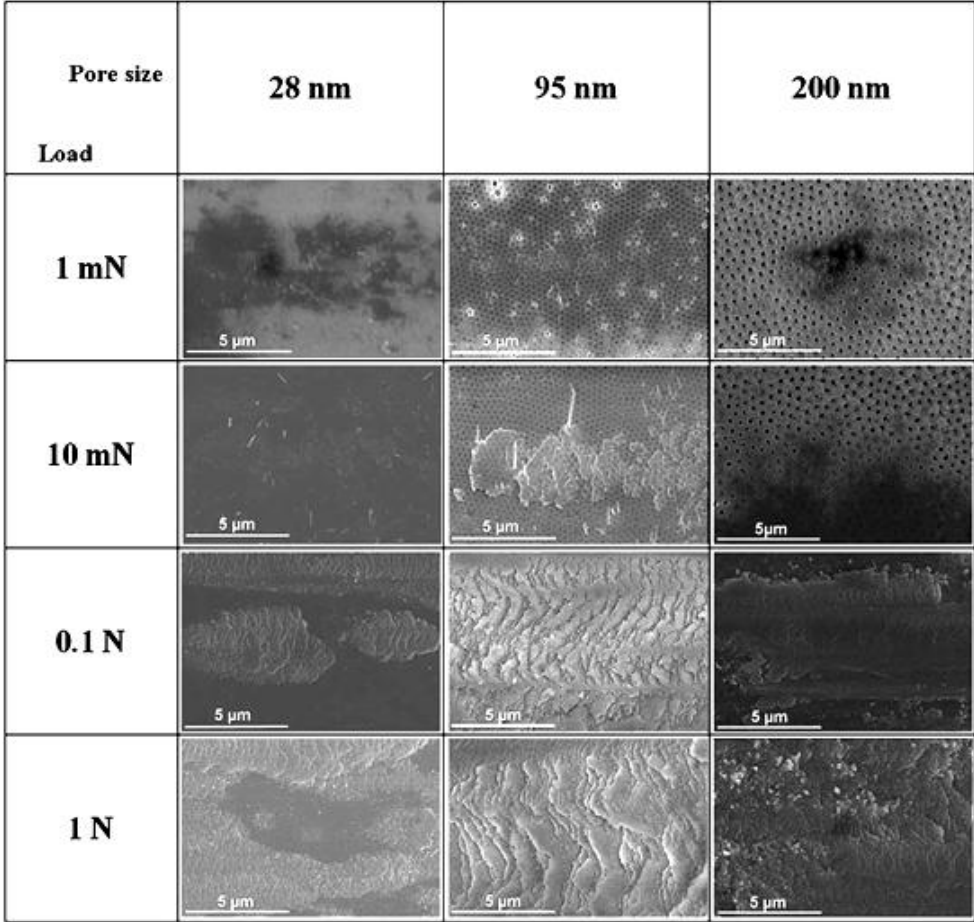


Figure 2.37: SEM images of tribolayer formed on the worn surfaces of nanoporous AAO films (Kim, 2010)

The tribolayers observed in the SEM images were in agreement with the illustration of possible wear mechanisms as a result of ductile deformation seen in figure 2.38 (Stachowiak, 2001). In Fig A, especially debris formed under 1N load had smeared wear particles and ductile grooving spreading fine debris particles nearby.

Finally, EDS results showed that there were tribochemical reactions those took place during sliding at rather high loads namely 100mN and 1000mN, between AAO and the steel counterbody. Debris was contaminated with Cr and Fe atoms (Kim, 2010).

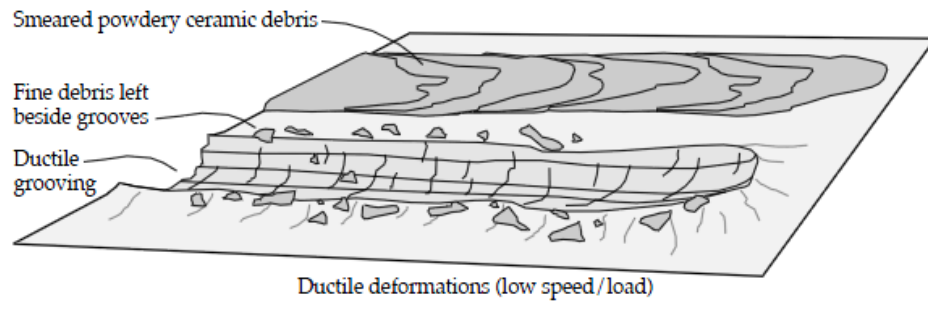


Figure 2.38: Wear track forming as a result of ductile deformations (Stachowiak, 2001)

3. EXPERIMENTAL METHODS

3.1 Production and Characterization of Samples

Experiments were carried out according to the scheme given in figure 3.1. in order to obtain well-ordered nanoporous AAO with various pore diameters in different baths namely sulphuric and oxalic acid. After production of the specimen, mechanical and tribological characterization tests were performed.

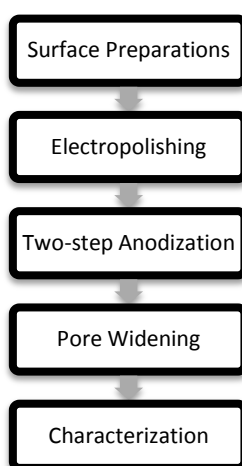


Figure 3.1: Experiment flow chart

3.1.1 Surface preparations

Pure aluminum plates (%99.99) with a thickness of 0.5 mm were cut in the dimensions of 2x4 cm. Samples were then annealed at 500°C for 4 hours for enlarging grain sizes. This annealing process is required for obtaining ordered AAO. Annealed plates were subjected to standard alkaline etching and desmutting procedure in 10 wt% NaOH solution for five seconds in 55°C for etching and in 10% HNO₃ solution for five minutes at room temperature for desmutting.

Pure aluminium plates provided by Alfa Aesar Johnson Matthey GmbH had already been subjected to annealing and there was no need for any alkaline etching and desmutting prior to electropolishing since they were already treated.

3.1.2 Electropolishing

After annealing and surface cleaning on Al sheets, samples were ultrasonically degreased in acetone and ethanol followed by a rinsing with deionised water. electropolishing was performed on the samples. Two types of electropolishing processes were used, namely:

- method I: Aluminium sheets (% 99.99, Alfa Aesar Johnson Matthey GmbH) were cut in smaller pieces and electropolished at a constant current density of $500 \text{ mA} \cdot \text{cm}^{-1}$ for 1 min in an electrolyte consisting of HClO_4 (60 wt %) and $\text{C}_2\text{H}_5\text{OH}$ (abs.) in a volumetric ratio of 1:4. Temperature was kept at $\sim 10^\circ\text{C}$. It must be noted that the sample edges were isolated. Surface area was no bigger than 1 cm^2 due to current limitations of the DC power supply.

- method II: Pure aluminum sheets were electropolished in a commercial (Politoksal EB-35 from Politeknik Metal San. ve Tic. A.Ş.), Cr free solution based on phosphoric –sulphuric acid mixture which was proposed by Paşaoğlu (2011). Polishing was conducted for $8 \div 10$ minutes, at a temperature of $65 \div 70^\circ\text{C}$ using a potential of 17 V. Electropolishing bath was stirred at a rate of 700 rpm. It is important to note that this method is and can be used in industrial applications. Therefore, it was performed to study the difference and the possible effect of this method on mechanical properties and frictional behaviour of AAO.

3.1.3 Anodizing

The anodizing of electropolished samples was carried out in two electrolytic baths in order to produce AAO with different properties. As we wanted to reveal the effect of electrolyte type on mechanical and tribological properties, two different electrolytes were chosen. The baths used were:

Sulphuric acid bath: A two step anodizing was performed in a 20 wt % sulphuric acid electrolyte using a two electrode electrochemical cell set up with a magnetic stirrer rotating at 500 rpm. The temperature was kept at $\sim 1^\circ\text{C}$ during anodization. Electropolished samples were cleaned in de-ionized water and anodised at a potential of either 15 or 21 V for 10 min. After a first anodizing step, samples were rinsed with de-ionized water and immersed in a solution of CrO_3 (1.8 wt%) and H_3PO_4 (6 wt %) for 10 and 15 min respectively, at $\sim 60^\circ\text{C}$ for the removal of the oxide layer obtained after the first anodizing. In this way, we achieved a pre-patterning of the aluminium

surface for growing regularly arranged pores during the second anodizing step. Second anodization was conducted at constant potential of either 15 or 21 V for 97 and 20 min respectively at $\sim 1^\circ\text{C}$.

Oxalic acid bath: Oxalic acid anodization was used for obtaining pore diameters varying between 25 and 80 nm. Two step anodizing was also used in these series of experiments. As electrolyte, 0.3 M oxalic acid was used. The electrolyte was stirred at 800 rpm. Parameters such as temperature, potential, and time were selected according to the results obtained by Paşaoğlu in 2011. First step anodizing was performed at 25°C for 1h. The potential applied was 40 V. The oxide removal was performed in the same solution as for samples anodized in sulphuric acid, only the time was longer (1h). After oxide removal, samples were anodized at 5°C at 70 V for 1h. Time was adjusted to produce approximately the same AAO thickness as in sulphuric acid bath. Finally, pores were widened at room temperature ($\sim 25^\circ\text{C}$) by immersion of as-received AAO in H_3PO_4 (5 wt %) for different durations namely 45, 60, 75, 90 and 110min to see the evolution of widening and to pick the precise durations needed to obtain accurate pore diameters.



Figure 3.2: Anodization setup used for oxalic acid anodizing

3.1.4 Mechanical characterization

Nanoindentation was performed at four different loads between 5 and 100 mN using Berkovich nanoindenters (CSM Instruments, CH). Loading and unloading rates were as twice as the maximum load, per minute. Indentation marks were examined by optical microscope and SEM.

3.1.5 Tribological characterization

Tribological tests were performed in the KUL-MTM fretting mode I apparatus and Modular Universal Surface Tester (MUST, Falex NV.). The counterbody was a 5mm corundum ball reciprocating on AAO samples at a frequency of 1 Hz. Steel balls were employed in previous studies and Kim et al. reported tribochemical reactions those took place during fretting (2010). To avoid such reactions, a counterbody made of the same material as the base material was used since the particles formed or material transfer during fretting would not change the composition of the debris. A stroke length of 100 μm , under a normal load of 40mN, 80mN and 1000mN, the test temperature and humidity was kept constant at 23°C and 50 % RH, respectively. Samples were degreased before the fretting tests, while after fretting tests they were ultrasonically cleaned in ethanol for 7-10 min to remove debris. Samples were examined using white light interferometer (VeeCo), scanning electron microscopy (SEM, Philips XL-30), Field Emission Gun SEM (FEG-SEM) before and after wear tests. Chemical composition was identified by energy-dispersive spectroscopy (EDS).

3.2 Results and Discussion

3.2.1 Electropolishing

Samples were examined using SEM and white light interferometer (VeeCo) before and after electropolishing. Results showed the great influence of electropolishing on surface roughness. Using white light interferometer, Ra and Rz values were measured. Ra and Rz correspond to average roughness and average maximum height of the profile, respectively. Prior to electropolishing Ra and Rz of as received Al sheets were $\sim 740\text{nm}$ and $\sim 7\mu\text{m}$, respectively. After electropolishing by method I these values dropped down to $\sim 250\text{nm}$ and $\sim 3.2\mu\text{m}$. After electropolishing by method II these values were $\sim 337\text{nm}$ and $\sim 2.54\mu\text{m}$. SEM image of the surfaces with and without electropolishing are given in figure 3.3.

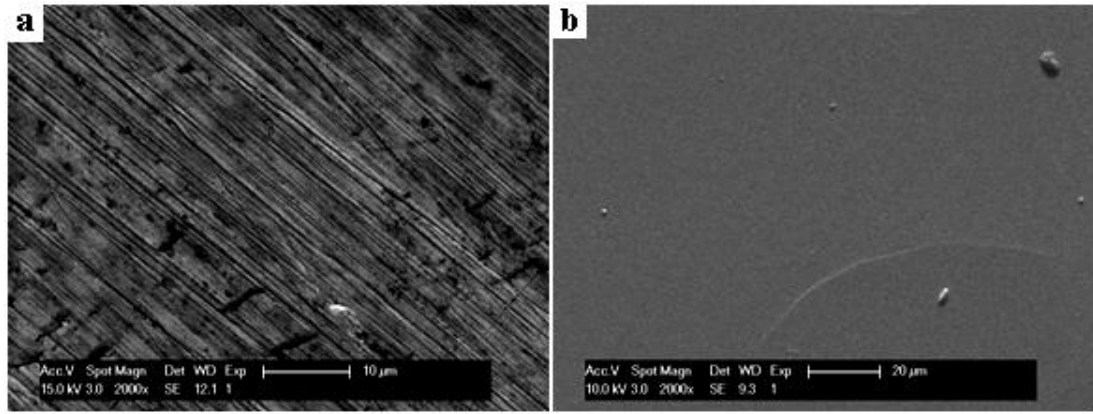


Figure 3.3: SEM image of Al surface a) prior to electropolishing; b) after electropolishing

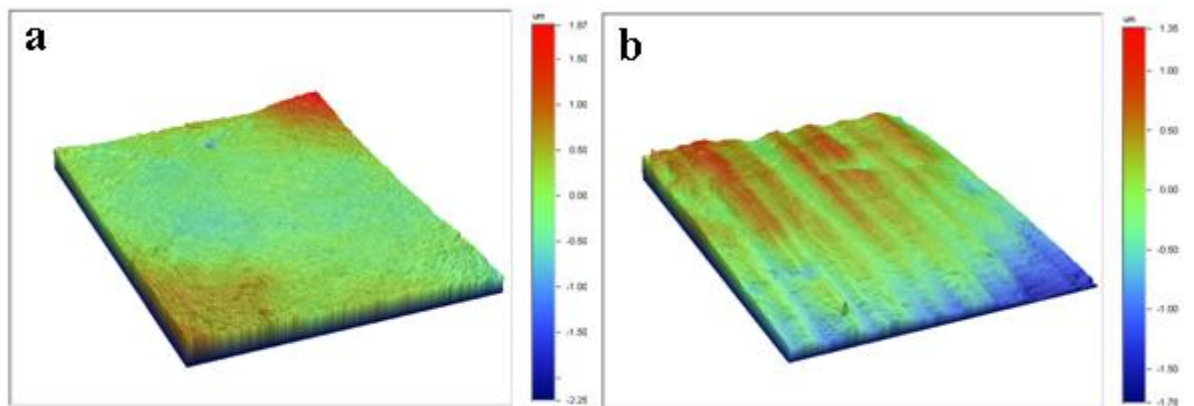


Figure 3.4: Surface profiles. a) method I, b) method II

Surface profiles, depending on the electropolishing method, were different at the end of the process. Although Rz values were lower for method II, an undulated surface was observed. Method I produced a smoother surface (figure 3.4a) with lower Ra value which is more important for reciprocating fretting tests at short displacements which is 100 μ m in our case.

3.2.2 Composition, pore size and thickness of the oxide layer

Prior to two step anodization samples were first anodized by single step anodization in sulphuric acid at 21V using the same parameters mentioned previously. SEM (PhilipsTM XL30 and JEOLTM JSM-7000F) characterization revealed the necessity of two step anodization since a well ordered porous structure was desired in our experiments. Examples of surface structures after single step anodizing are presented in figure 3.5. Both images were taken from the same sample after anodization. figure 3.5a belong to a spot on the surface of the sample while figure 3.5b was taken from another spot from the same surface. Pores in figure 3.5a show a relatively ordered

distribution whereas those in figure 3.5b are not ordered. Bumps can be noticed in figure 3.5b which ruin the homogeneity of the surface. Thus, two step anodization was indeed necessary to produce AAO with homogeneously distributed pores with equal diameters.

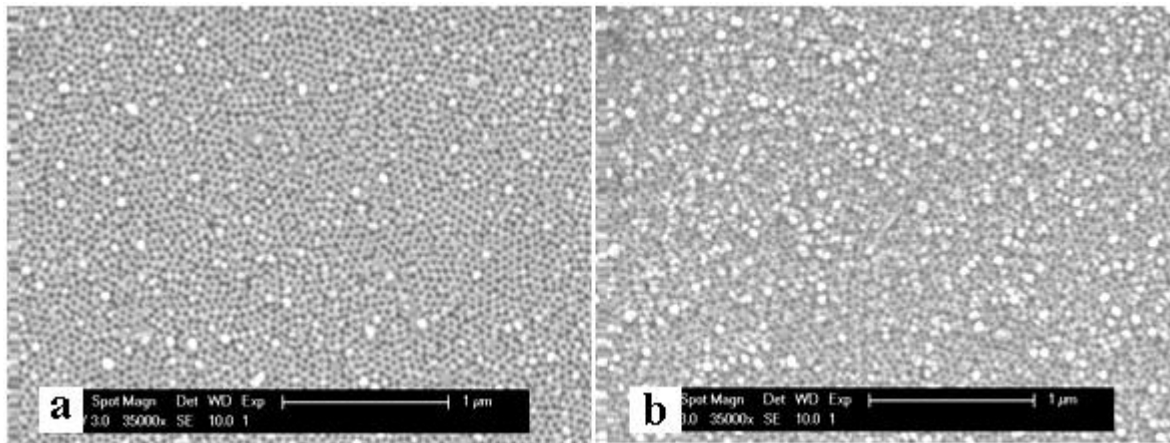


Figure 3.5: SEM images taken from different spots on the surface of anodized aluminium after a single step anodization at 21V

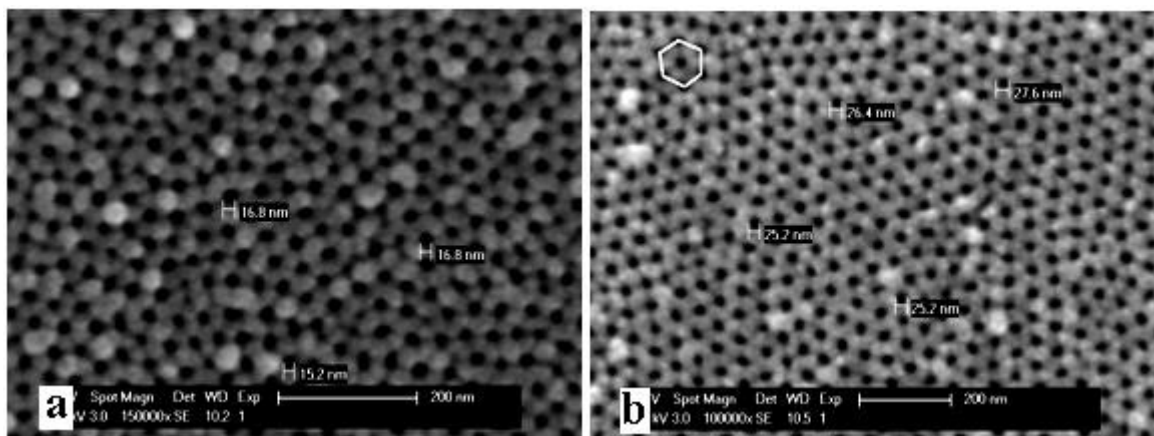


Figure 3.6: Hexagonally distributed (indicated by white hexagon, b)well-ordered nanoporous AAO produced in sulphuric acid at a potential of a)15V, b)21V, for 97 and 20 min, at a temperature of $\sim 1^{\circ}\text{C}$ with pore diameters of a) $\sim 16\text{nm}$, b) $\sim 27\text{nm}$

Aluminium was first anodized in sulphuric acid since it was known that sulphuric acid is used to produce pores with the smallest diameters. Two step anodization was successful as can be seen in SEM images given in figure 3.6 which belongs to samples anodized in sulphuric acid. Well-ordered and hexagonally distributed pores were obtained with two different pore diameters.

Effect of the applied potential on pore diameter can be noticed. Pore diameter obtained by sulphuric acid anodization at 15V, was $\sim 16\text{nm}$ figure 3.6a) while that

produced at 21 V was ~27nm (figure 3.6b). For the sample anodized at 15V, wall thickness was ~23nm while interpore distance was ~39nm. As for the specimen with ~27nm pore diameter, wall thickness was ~30nm and interpore distance was ~57nm. A remarkable difference of the two samples produced at 15V and 21V about their appearance was the roughness. The surface of the sample anodized at 15V had bumps and the walls did not seem as smooth as those of 21V sample. Thickness of the oxide layer was measured using FIB-SEM (FEI™ Co.). It was known that anodization rate increased with increment in applied potential. Thus, durations of the second step anodizing were adjusted to 97min and 20min at potentials of 15V and 21V, respectively. Achieved thickness was 17µm (figure 3.7). Durations were estimated from previous studies made by Sulka (2006). For sulphuric acid anodization, estimated oxide growth rates at ~1°C depending on applied potential are given in Table 3.1. It must be noted that growth rate differs at long anodization durations due to lower diffusion of the electrolyte in the pores. Although oxide growth is fast in the beginning, by time it slows down as a result of diffusion limitations.

Table 3.1: Linear growth rates of AAO during anodization in sulphuric acid (Sulka,2006)

Potential (V)	Linear Growth Rate(µm/min)
15	0,103
21	0,486

We confirmed the existence of S atoms in the structure by EDS. Bensalah et al. had studied anion contamination more precisely (2011). Our EDS analysis is given in figure 3.8.

Two step anodization in oxalic acid ended up with well-ordered structure of pores with ~27nm pore diameter. Wall thickness was measured as ~65nm (figure 3.9). Pore diameter was similar to that we produced in sulphuric acid at 21V but there was an obvious difference between the wall thicknesses.

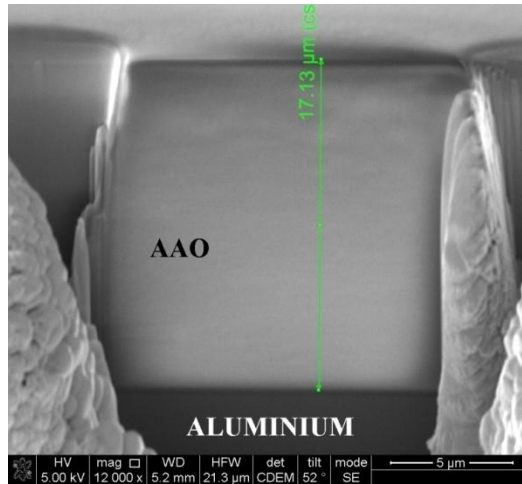


Figure 3.7: Crosssectional FIB-SEM image of AAO produced in sulphuric acid

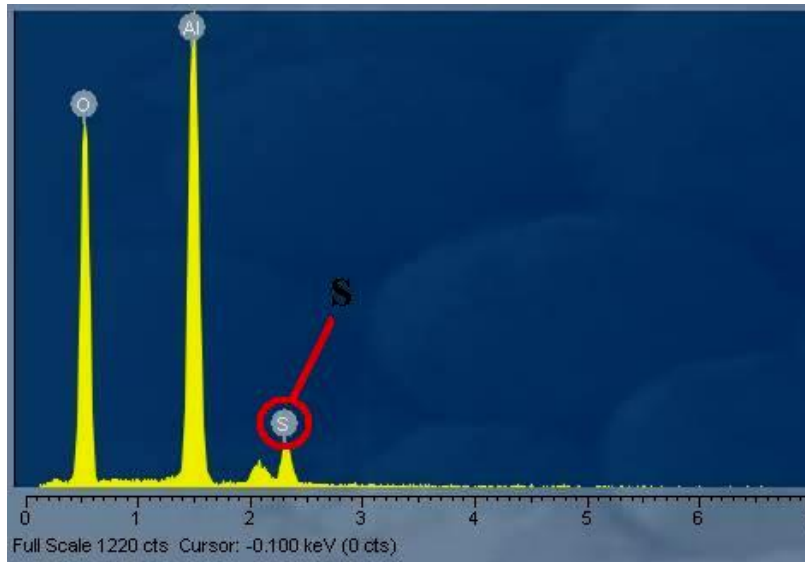


Figure 3.8: EDS results of AAO produced in sulphuric acid

EDS analysis (figure 3.10) proved there was C in the oxide layer. This was in agreement with results of Bensalah et al. (2011).

After observing as-produced AAO in oxalic acid, pore widening was performed for different durations namely 45, 60, 75 and 90 and 110 min. SEM investigations showed that after about 80 min widening, walls started to vanish, ruining the homogeneous distribution. Evolution of widening with time can be seen in figure 3.11. Vanishing of cell walls can be realised in figure 3.11d which is after 90min. After 110min dissolution of walls take place deeper inside the tubes leaving some pieces those are not yet dissolved.

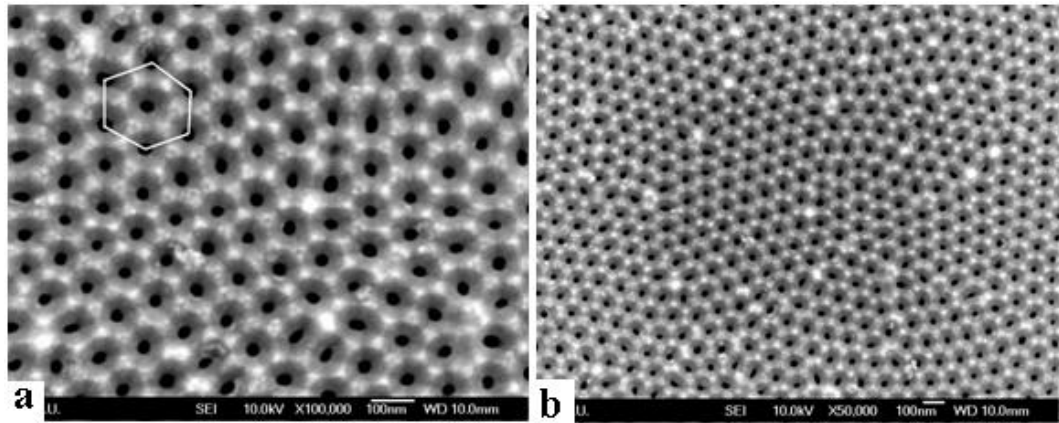


Figure 3.9: SEM images of hexagonally (indicated with white hexagon) arranged pores of AAO produced in oxalic acid at 40V (first step) and 70V (second step) a)high magnification, b)lower magnification

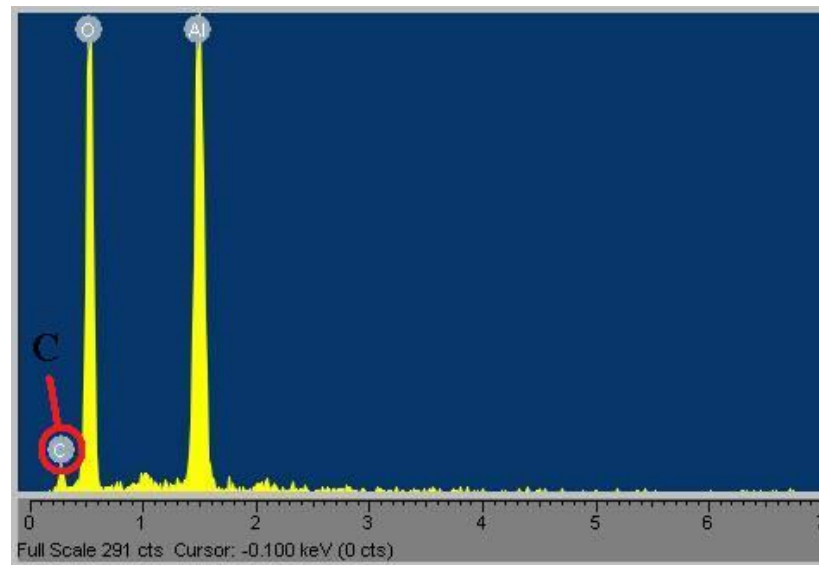


Figure 3.10: EDS results of AAO produced in oxalic acid

As a result of first widening trials on as-produced oxalic acid samples and taking previous studies (Vojkuvka, 2007) into account, pore widening durations were fixed at 32min and 75min to obtain pore diameters of $\sim 45\text{nm}$ and $\sim 75\text{nm}$. SEM images of samples after widening are given in figure 3.12. Samples were anodized for 1h at 70V (second-step) so that the thickness would be $\sim 17\mu\text{m}$ (Fig I) which was the same as those anodized in sulphuric acid.

Samples produced in sulphuric acid with pore diameters of $\sim 16\text{nm}$ and $\sim 27\text{nm}$ will be called hereafter as S1 and S2, respectively. Those anodized in oxalic acid and porewidened afterwards, with $\sim 27\text{nm}$, $\sim 45\text{nm}$ and $\sim 75\text{nm}$ pore diameters, will be recalled as O1, O2 and O3 (Table 3.2).

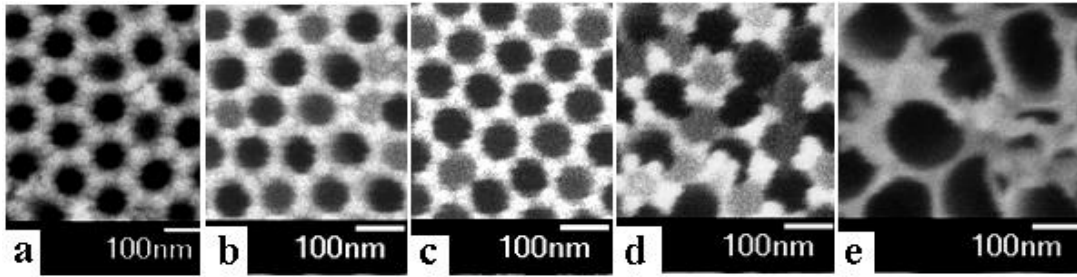


Figure 3.11: SEM images of AAO after pore widening for a)45min, b)60min, c)75min, d) 90min, e)110min

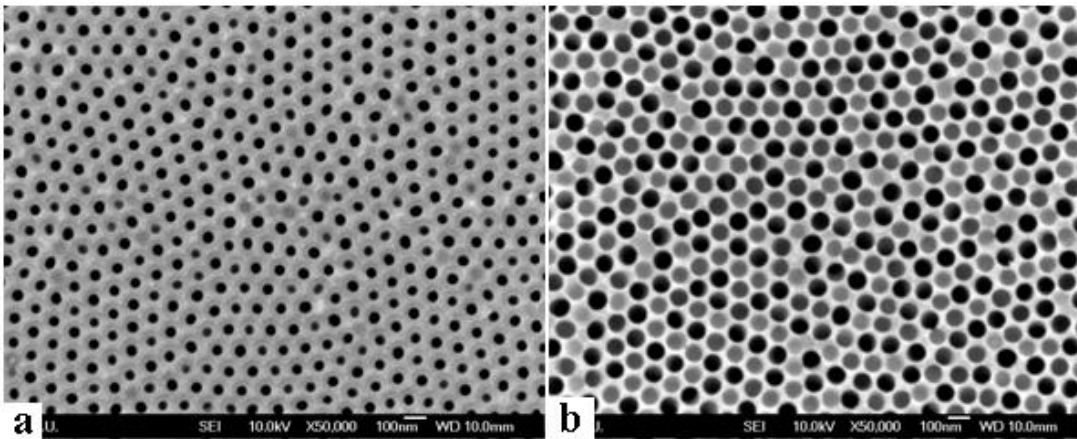


Figure 3.12: AAO produced in oxalic acid and subjected to pore widening for a)32min, b)75min

Appearance of the cell walls of all samples produced in oxalic acid did not have significant difference as we saw on S1. Porosities were calculated according to equation (2.10) given in 2.2.5.2 using the following parameters in Table 3.2. Since pore diameters of O2 and O3 were finished by pore widening, interpore distances were the same as the AAO before widening (O1).

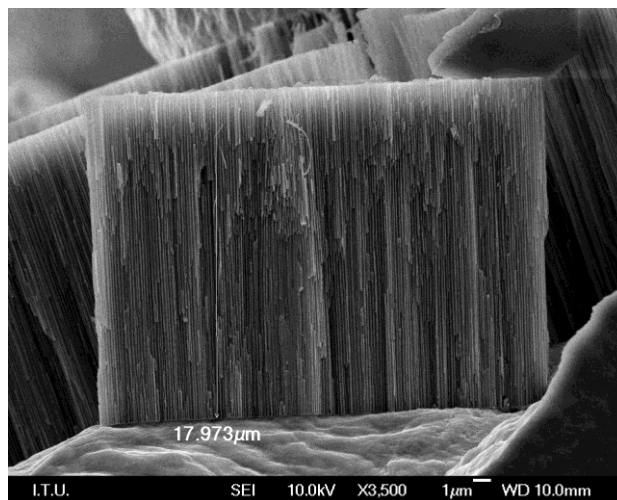


Figure 3.13: Crosssectional FEG-SEM image of ~17μm thick AAO produced in oxalic acid

Table 3.2: Sample names with pore diameters and porosity percentages

	Pore diameter (nm)	Interpore distance (nm)	Porosity (%)
Sample No	Sulphuric acid		
S1	~16	~39	15,26
S2	~27	~56	19,54
	Oxalic acid		
O1	~27	~94	8,45
O2	~45	~94	20,34
O3	~75	~94	64,31

3.2.3 Mechanical characterization by nanoindentation

Nanoindentation tests were performed over a wide range of normal loads (5 to 100 mN) to study the mechanical behaviour of anodized aluminium oxides. Loading rates were as twice as the peak load applied per minute (e.g. 10 mN.min⁻¹ for 5mN max load) Indentation imprints were observed by SEM. Loading vs. penetration depth data was recorded. Hardness values were measured by Oliver & Pharr method. Representative SEM images of the imprints are given in figure 3.14.

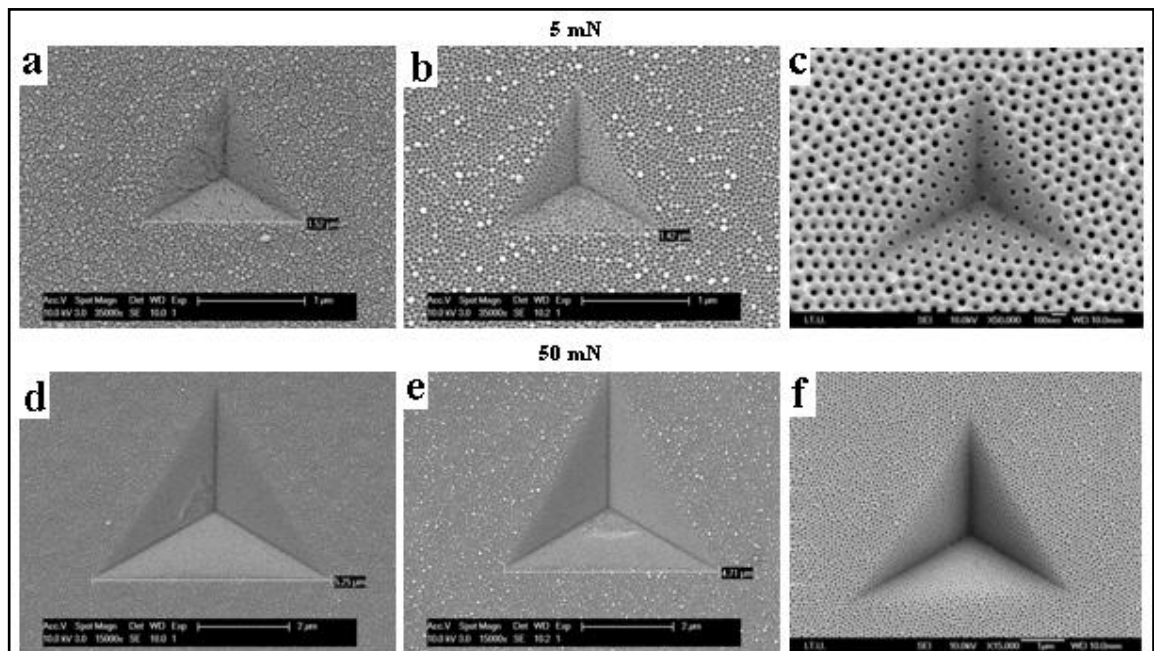


Figure 3.14: SEM images of nanoindentation imprints done on AAO with a pore diameter of ~16 (S1) (a,d), ~27 (S2)(b,e) and 45 nm (O2) (c,f). The anodizing was done in sulphuric acid (a-e) and oxalic acid (c,f)

Since AAO is a ceramic material, crack formation and propagation was expected as a result of nanoindentation. But SEM images revealed an interesting response. Oxide layer was only deformed locally only where the indenter was in contact with the surface. AAO did not respond by formation of major cracks either inside or outside the imprint which was a different result from Ng et al. reported (2009) that was mentioned in the previous chapter. So-called bilinear cracks (Ng, 2009) were not observed neither on sulphuric acid samples nor those produced in oxalic acid. Although we applied loads varying between 5-100 mN which included loads that Ng and co-workers applied, other nanoindentation parameters such as loading-unloading rates and pausing duration were different than those Ng et al. used. Therefore, we believe that test parameters can effect the the deformation mechanism of the oxide layer.

Another reason for these imprints without major cracks can be related to the structure of AAO. The anodized layers show differences in structure when compared to bulk Al_2O_3 . They contain substantial amounts of OH which was shown by Wang and colleagues (2004). XRD patterns of AAO were given in the previous chapter. OH compounds might have increased plastic behaviour.

S1 and S2 had minor crack formations within the imprint area while O1, O2 and O3 were plastically deformed (figure 3.15). figure 3.15a and figure 3.15b show SEM images of S1 and S2 at relatively high magnifications. White circles show the minor cracks mentioned. Comparing S1 and S2 we could see that minor cracks were present on both of the samples. However the amount of the cracks formed as a result of indentation with same parameters, were less on S2 which had wider pores. This showed that pore diameter effected formation of cracks. Afterall, sulphur contamination and the structure of AAO produced in sulphuric acid might have made the oxide more brittle. In case of comparing O1 (figure 3.15c) and S2 (figure 3.15b) which had approximately the same pore diameters we did not observe similar cracks on O1. This difference may be related to the differences between the structural composition of AAO films produced in sulphuric and oxalic acids. No cracks were observed either on O2 or O3 (figure 3.15d and e).

Loading – penetration depth curves are given in figure 3.16. Indeed, having a close look at the loading and unloading curves (figure 3.16), it appears clearly that the elastic recovery of AAO produced in sulphuric acid (figure 3.16a, b) regardless of its

pore diameter or porosity, is larger than those produced in oxalic acid (figure 3.16 c-e).

A more precise comparison can be done by comparing the penetration depth under maximum load and the final depth after load was released. These values with calculated recovery percentages are given in Table 3.3.

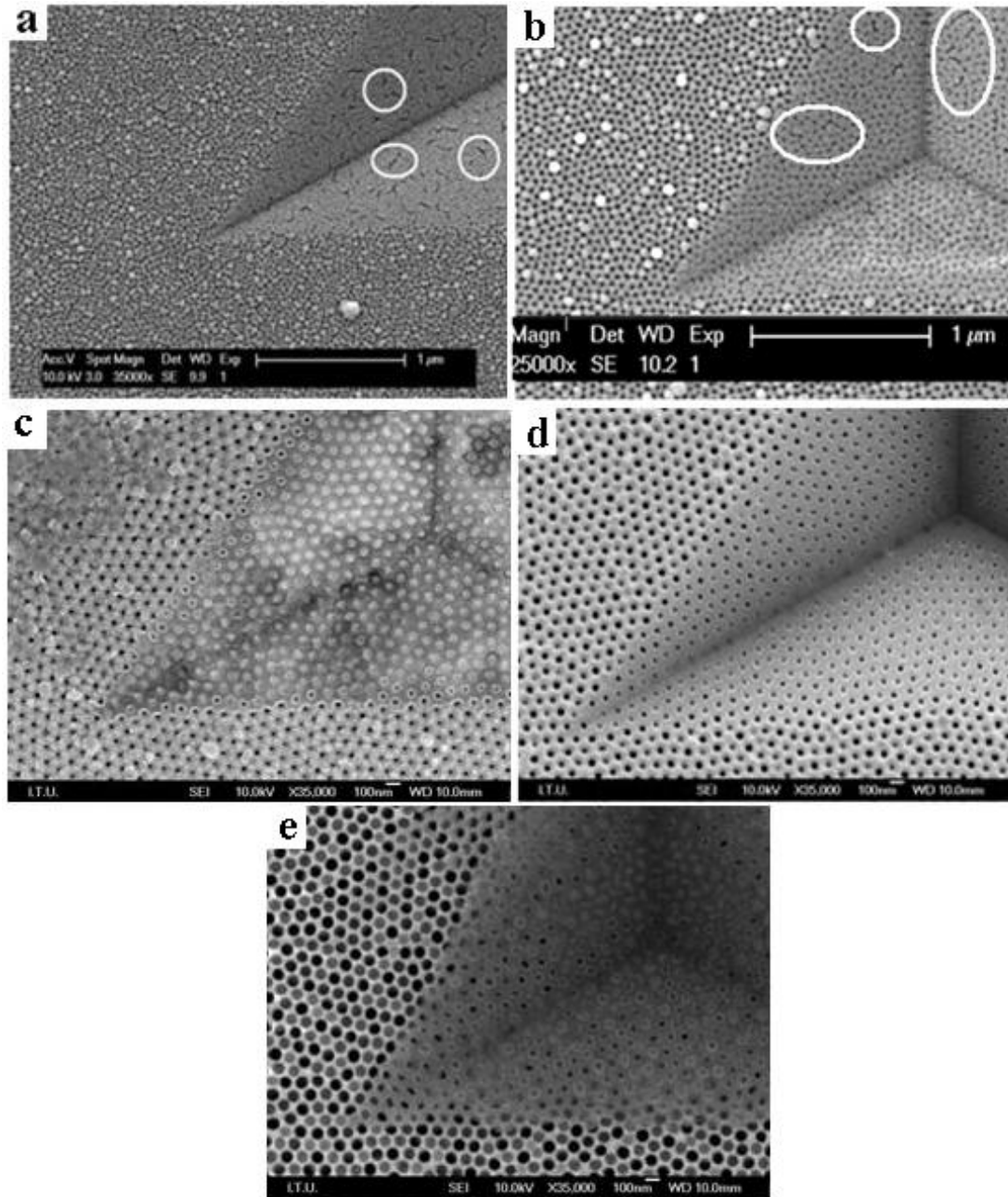


Figure 3.15: SEM images of nanoindentation imprints under 50mN on a)S1, b)S2, c)O1, d)O2, e)O3

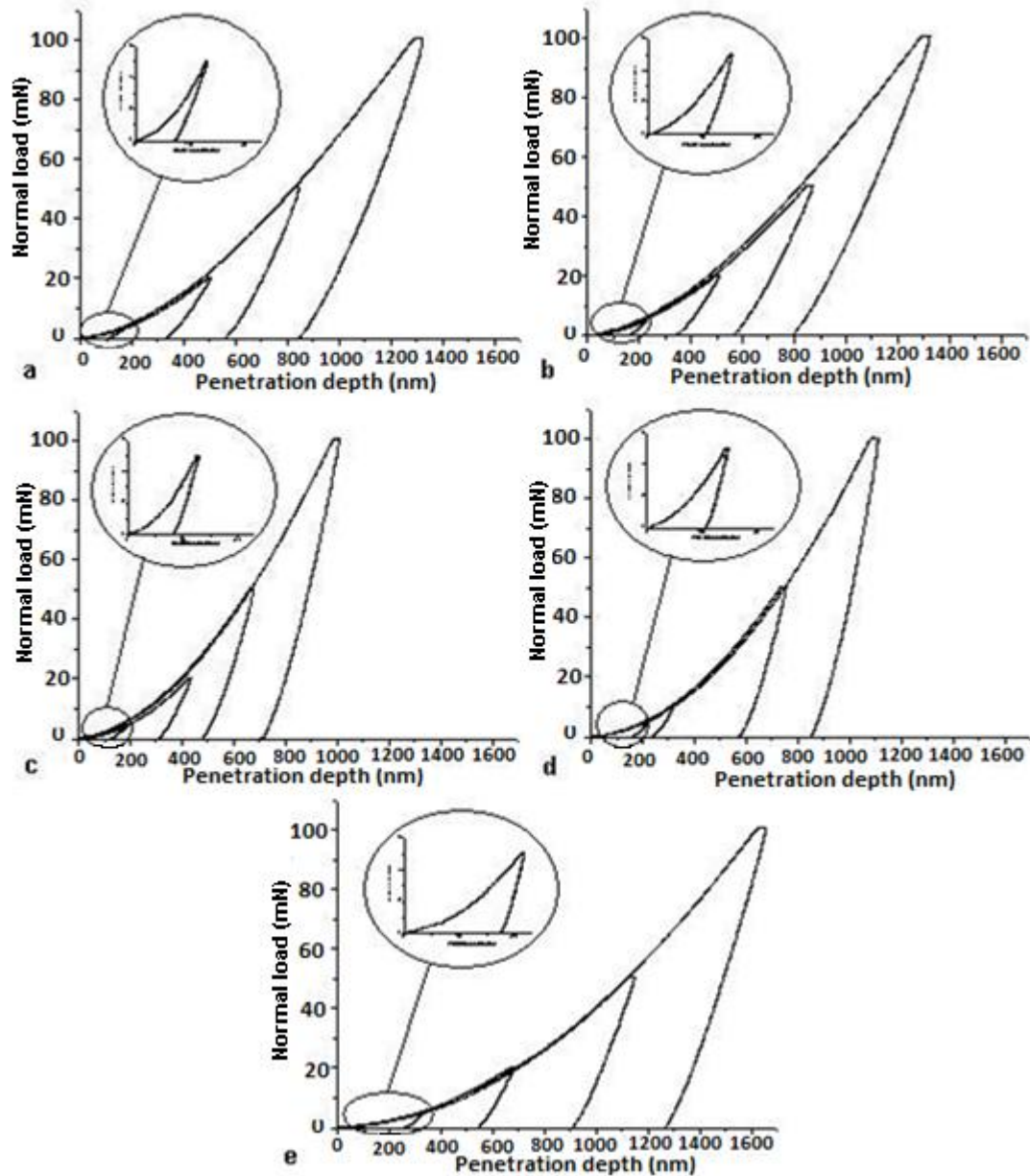


Figure 3.16: Loading-unloading nanoindentation curves on AAO at 5 (magnified), 20, 50 and 100mN normal loads a)S1, b)S2, c)O1, d)O2, e)O3

O2 and S2 had similar porosity percentages. They were compared so that the effect of porosity percentage could be ignored. A significant difference was noticed. While O2 had a recovery of ~24%, recovery of S2 was ~41%. As O1 and S2 had similar pore diameters, same comparison was done between these two samples for ignoring possible effect of pore diameter. Again, recovery of the sample produced in oxalic acid was less than that in sulphuric acid. Samples produced in oxalic acid electrolyte had similar recovery percentages among themselves. Same case was present for those produced in sulphuric acid. In addition, although final indentation depths were almost same for O1, O2, S1 and S2, maximum penetration depths were deeper for S1

and S2. The effect of the film structure as explained in the previous section showed its effect also on indentation behaviour. Thus, the films formed in sulphuric acid are softer than those formed in oxalic acid. Hardness and elastic modulus are discussed followingly.

Table 3.3: Maximum penetration and final depths of the nanoindentation imprints under 100mN maximum load

	Maximum penetration depth (~nm)	Final Depth (~nm)	Recovery (~%)
S1	1320	840	36
S2	1325	780	41
O1	1010	710	29
O2	1110	845	24
O3	1650	1260	24

Finally, O1 and O3 were compared to see the effect of porosity. It is hard to miss the difference between loading-unloading curves (figure 3.16c and e). Under same conditions, O1 was more resistant to plastic deformation while O3 was drastically deformed. This difference was directly linked to the porosity effect which is much higher for O3.

As noticed on all loading-unloading curves, no major cracks, pop-in or phase changes took place according to the curves. The curves were smooth without any obvious sudden changes during tests. However, if the tests were run at very small loading rates, pop-in might have been observed as reported by Ng et al. (2009).

Curves “nanohardness vs. penetration depth” obtained during indentations at normal loads of 5mN, 20mN, 50mN and 100mN of samples S1, S2, O1, O2 and O3 are given in figure 3.17. Nanohardness values are raw data calculated by nanotester software using Oliver&Pharr method and Berkovich indenter tip.

S1 and S2 had relatively similar hardness values varying between ~4.5 and ~6GPa. It was probably due to the very small difference in porosity percentage. However, at a rather low load (5mN), a scatter was observed on S1. Hardness went up to ~10GPa which could easily be distinguished from the other hardness values measured at higher loads. This unexpected increase can be linked to the rough surface with bumps which was previously mentioned. Thus, this hardness value can not be considered as a representative value and should be ignored.

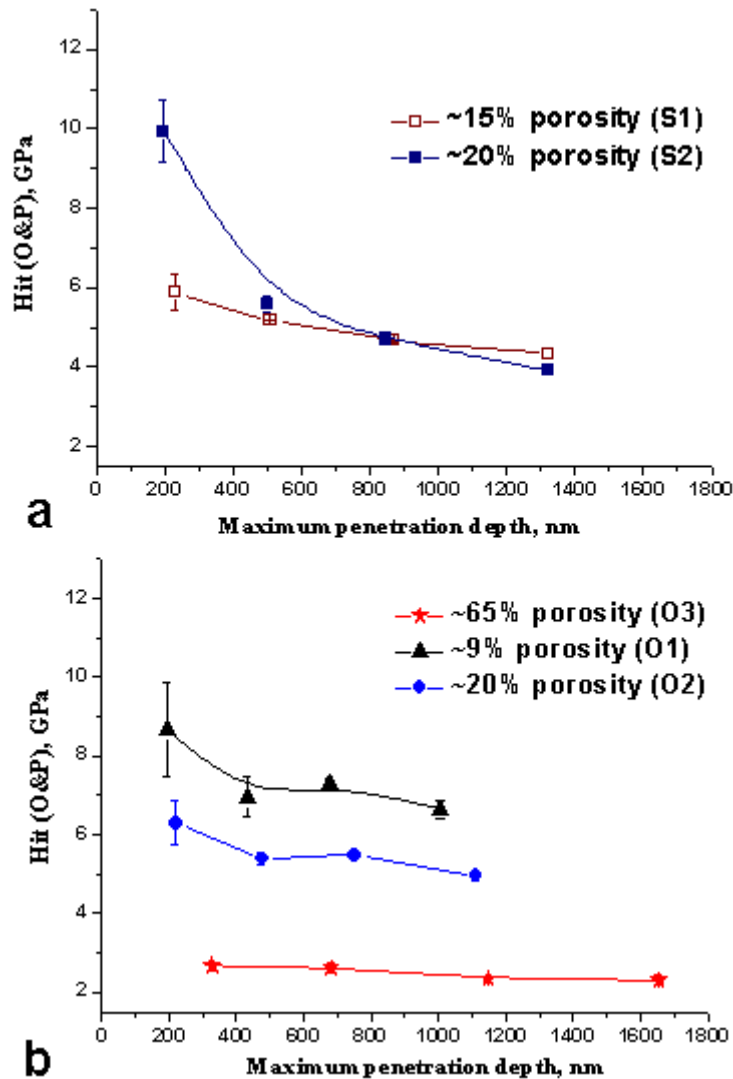


Figure 3.17: Hardness- Penetration depth curves of AAO produced in a) sulphuric acid, b) oxalic acid

To be able to see the effect of porosity on mechanical properties, hardness values of samples produced in oxalic acid were compared. As the composition of these samples were the same, it was assured that the composition effect would be ignored. Porosities of O1, O2 and O3 had distinct differences between each other. This difference also influenced hardness values as seen in figure 3.17. O1 had the highest hardness while O3 had the lowest. The higher the porosity was, the lower the hardness got. Such behaviour was expected since the decrease in solid area would lead to higher penetration depth which in return gave a bigger contact area. Hardness was calculated by equation (2.13) given in the previous chapter(2.3.1)

During calculation of given hardness values by Oliver&Pharr method, porosity was not taken into account. Thus, the hardness of overall structure (porosity + solid area)

was calculated. If the hardness calculations are made by removing porosity effect and by only taking the solid area into consideration, contact area, A_c , decreases in relation to solid surface percentage. After multiplying the contact area by porosity percentages given previously, hardness values showed a considerable change. By this recalculation, surfaces were assumed to be non-porous. Hardness values belonging to oxalic acid samples O1, O2, O3 and sulphuric acid samples S1 and S2 after recalculation (so-called corrected hardness) are given in figure 3.18. Surface roughness was mentioned to be effective on results of tests at low loads. To have more interpretable curves, hardness values of 5mN tests, which were scattered, were put out in figure 3.18c.

The porosity percentages of S1 and S2 were close to each other. In figure 3.18a corrected hardness values, despite a little increase, did not appear to have a significant change. Similar change was observed in hardness values of O1 and O2. O3 however, showed a great increase after correction, from ~2.5GPa to ~7GPa (figure 3.18b). Corrected hardness of O3 is quite close to that of O1 and O2. Assuming possible errors during nanoindentation and also at calculations, corrected hardness curves did not precisely match onto each other but instead they were really close to each other (figure 3.18b). Thus, if the solid area of AAO is taken into consideration only, it can be seen that the hardness of the anodic aluminium oxide as a material is actually the same for all samples. Porosity effects the hardness of the whole structure.

Curves drawn with dashed lines in figure 3.18c belong to oxalic acid samples while those with solid lines indicate sulphuric acid samples. These curves were drawn to compare the corrected hardnesses of samples produced in different baths to clarify the effect of anion contamination. O1, O2 and O3 were slightly different from each other. Likewise, S1 and S2 had the same manner. In case of comparing the two bands which include dashed and solid lines separately (figure 3.19), it can be seen that carbon contamination within the oxide caused higher hardness than sulphur anions. Corrected hardness values for oxalic acid samples varied between ~8GPa and ~7GPa.

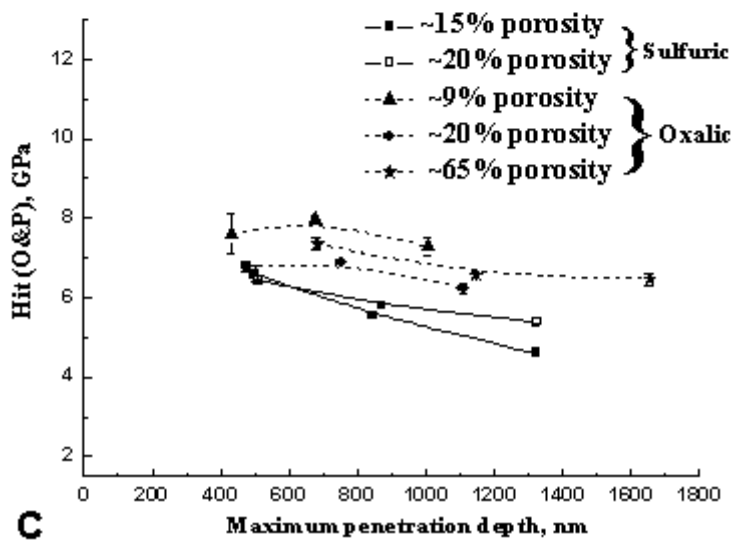
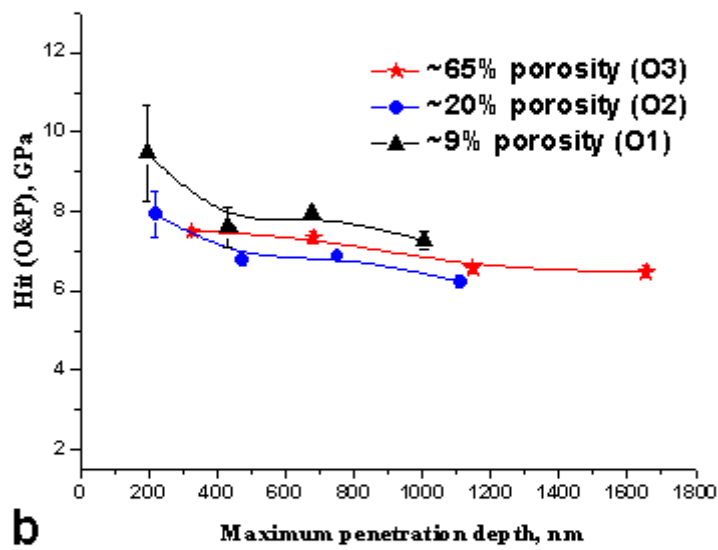
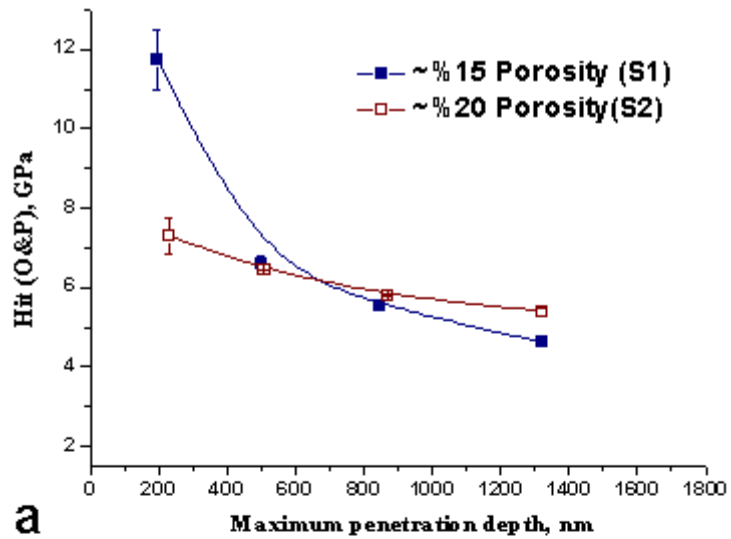


Figure 3.18: Corrected hardness-Penetration depth curves of a)S1 and S2, b)O1, O2 and O3, c)all samples

Sulfuric acid samples had hardness values between ~6GPa and ~5GPa. Regardless of porosity, anion contamination or pore diameter, hardness followed a decreasing trend in accordance with penetration depth.

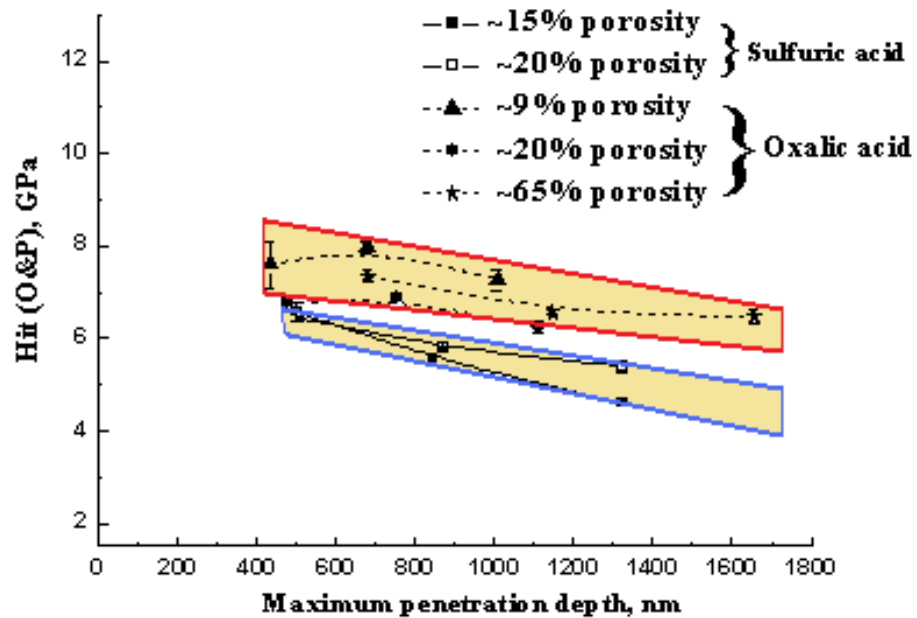


Figure 3.19: Comparison of corrected hardness curves

Elastic modulus was effected by both porosity and anion contamination. Evolution of elastic modulus with penetration depth is given in figure 3.20. O1 and O2 had a relatively high E varying between ~100 and ~110 GPa. Due to high porosity, E of O3 was low and decreased from ~60GPa to ~40GPa with increment in penetration depth. Evolution of E was relatively steady. As the composition of these samples were the same, the remarkable difference between O1,O2 and O3 was linked to the difference in porosities. S1 and S2 on the other hand, followed a decreasing trend. Their porosities were close to each other and to O2 as well. Therefore, by ignoring porosity percentage, the results were compared in relation to the composition of AAO. Sulphur contamination caused the material become more elastic. Decrease rate of E of S1 and S2 was more than that of O2.

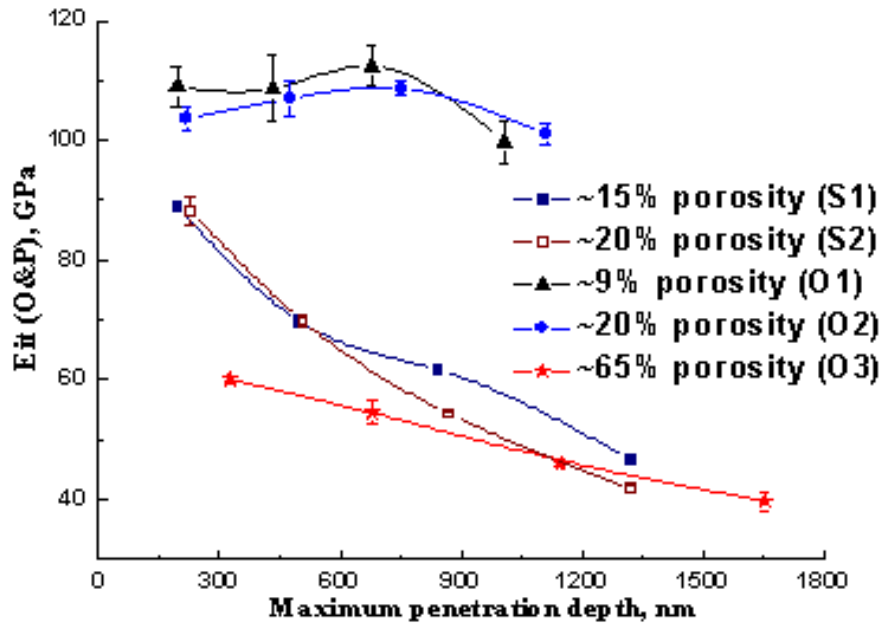


Figure 3.20: Elastic modulus-penetration depth curves

3.2.4 Tribological characterization

Nanoindentation tests revealed that AAO could stand against normal loading. It didn't respond by propagation of cracks or any other catastrophic damage. Tribological characterization was performed to see how AAO would behave under biaxial loading. Ball-on-flat tests were run to apply bidirectional loading. Wear mechanism was investigated in relation to pore diameter, porosity percentage and oxide composition.

As mentioned previously, to avoid possible tribochemical reactions, a ball counterbody made of corundum with 5mm diameter was employed. Since previous studies made by other researchers were carried out using a steel ball, before agreeing on our test parameters, pilot tests were run on S1 and S2 to see how the behaviour would be. These tests were run at 1Hz, for 1000 cycles with a displacement of 500µm. Normal loads were chosen as 40 and 80mN(meso-scale). Hertzian contact pressure could not be calculated precisely due to porosity. After fretting tests, samples were ultrasonically cleaned in absolute ethanol. SEM images are given in figure 3.21.

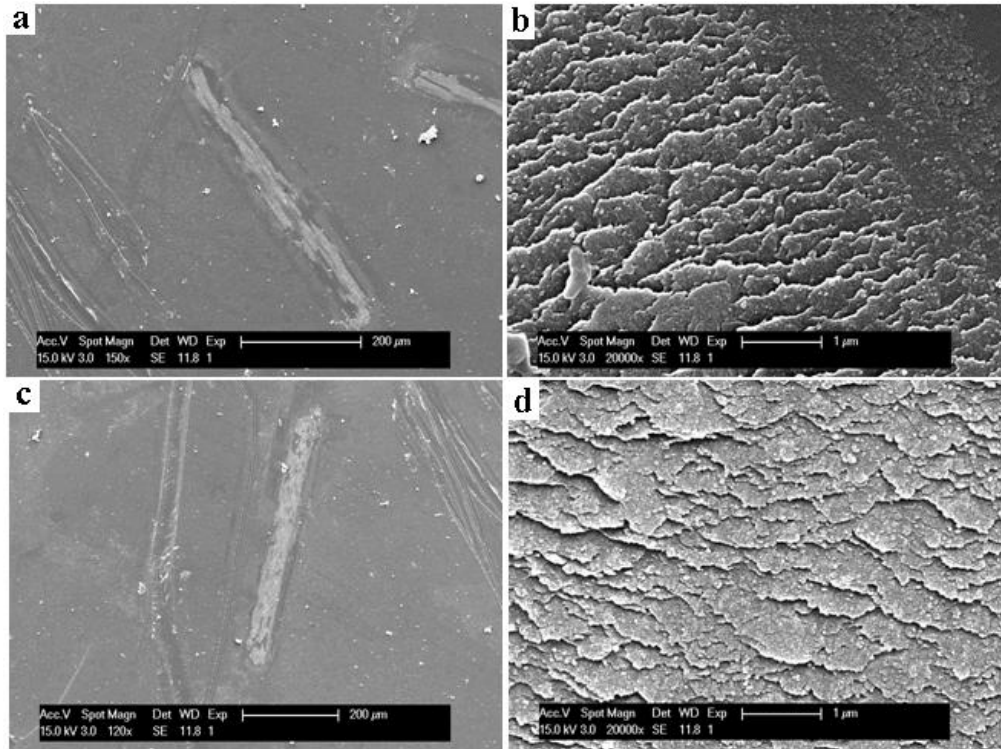


Figure 3.21: SEM Images of wear tracks on S1 (1Hz, 500μm, 1000 cycles) a,b) under 40mN normal load; overall view, center respectively and b)under 80mN; overall view and center, respectively

Evolution of friction coefficient was measured and it was seen that after running-in, a steady state was reached in both cases (figure 3.22). During steady state COF was approximately 0.9. Running-in period was a point of interest. Thus, fretting tests were run for 50 cycles with the same parameters to reveal the wear mechanism and how it evolved. Wear tracks were examined using SEM (figure 3.23). At high magnifications an interesting response was realised (figure 3.23d, f). Pores started to be filled in by fine debris particles without any cracking. This behaviour proved that the tubes were strong enough to resist bidirectional loading.

For the rest of the tests, displacement was shortened from 500μm to 100μm to decrease the possible effect of surface imperfections. Loads were selected as 40, 80mN (meso-scale) and 1000mN (macro-scale). After 1000 cycles, surface was covered by a thick debris with same appearance independent from the load applied.

COF was calculated from the fretting loops using the following equation;

$$\mu = \frac{F_t}{F_n} \quad (3.1)$$

where σ is the friction coefficient, F_t is tangential force and F_n is the normal force. Representative loops obtained from meso-scale fretting tests are given in figure 3.24. Fretting hysteresis loops showed that the tests were carried out in gross slip regime. Slip ratios which also showed that the fretting was in gross slip regime, are given in Table 3.4. The relation between the slip ratios and the slip regimes were given in the previous chapter, under 2.4.1.1.

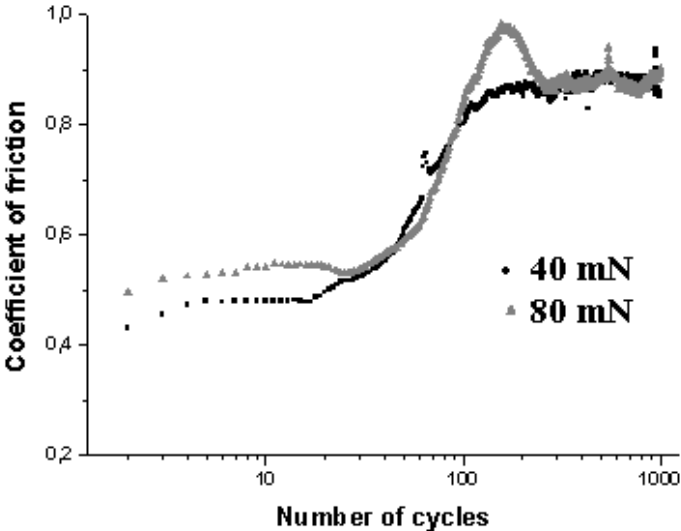


Figure 3.22:Evolution of COF of S1(1Hz, 500µm, 1000 cycles)

Table 3.4: Slip ratios of S1 and S2

Normal Load (mN)	Slip ratio	
	S1	S2
40	0.75	0.75
80	0.45	0.5
1000	0.8	0.82

In the running in period of meso scale tests, it was observed that the tangential force was lower which later on increased. This shows that abrasive wear in the beginning caused formation of wear particles as third body which made the relative motion harder due to an adherent behaviour. Thus, wear mechanism was a combination of abrasive and adhesive wear resulting in a high COF. Increasing normal load from 40mN (figure 3.24a and c) to 80mN (figure 3.24b and d) with the same displacement amplitude caused a decrease in sliding distance with fretting cycles. This can also be linked to the adherent manner of the debris or the penetration of the ball into the wear track.

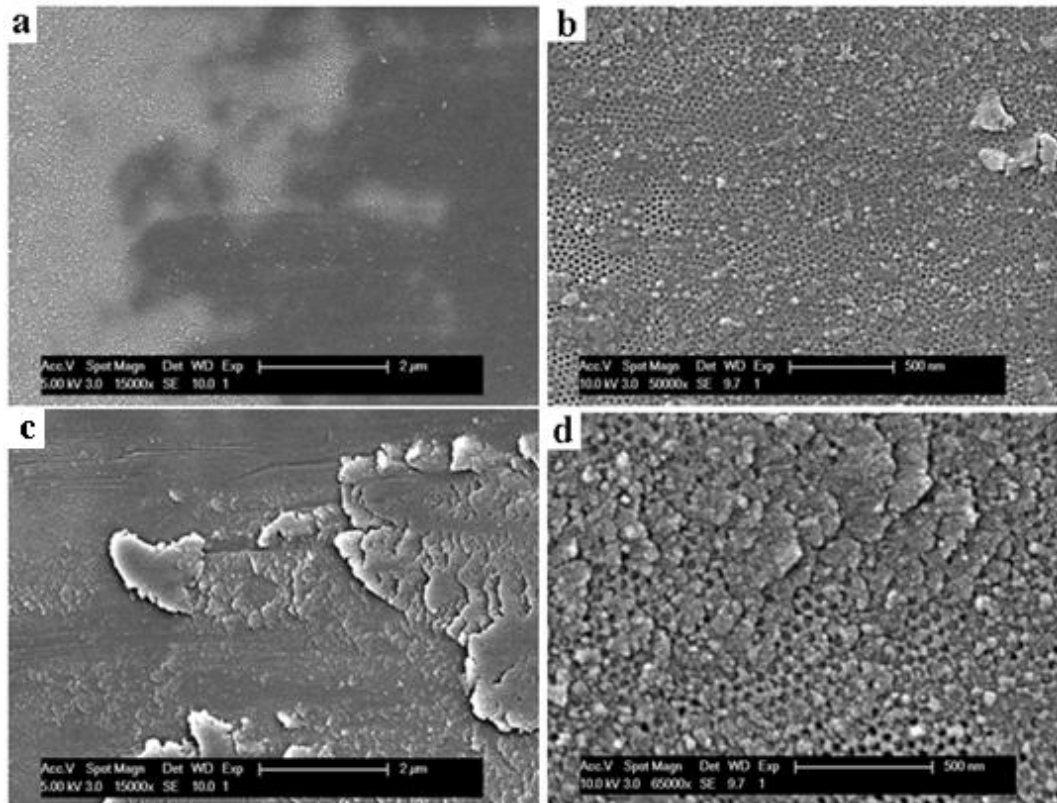


Figure 3.23:SEM Images of different wear Tracks (50 cycles, 1 Hz, 100 μm displacement) on AAO anodized at 21 V: Normal load of a,b)40mN, c,d) 80 mN

As for macro scale loading (figure 3.24e and f), tangential force showed a decrease with fretting cycles. The difference between evolution of loops under 1000mN and meso-scale loading loops can be linked to the penetration depth of the counterbody which was deeper under higher normal load. Once the ball created a wear track by abrasive wear, it was easier to carry out a relative motion decreasing tangential force. The stiffness of the macro-scale fretting machine was more than that of meso-scale fretting tester. Thus, the obvious effect of adhesive wear we realised under meso scale loading, was not that apparent under macro scale loading.

O1, O2 and O3 were tested under the same conditions. Tests were run for 500 fretting cycles at 100 μm displacement. Under 40mN and 80mN normal load, fretting tests did not reveal reliable results due to roughness. As mentioned previously, after electropolishing by method II, an ondulation was observed. Although surface had a mirror-finish, contact between the counterbody and the surface was not proper due to this undulated surface. This was also confirmed by SEM observation of the wear tracks. Therefore, only the results of the tests performed under 1000mN were taken

into account for comparison. Representative loops of O1, O2 and O3 under 1000mN load are given in figure 3.25.

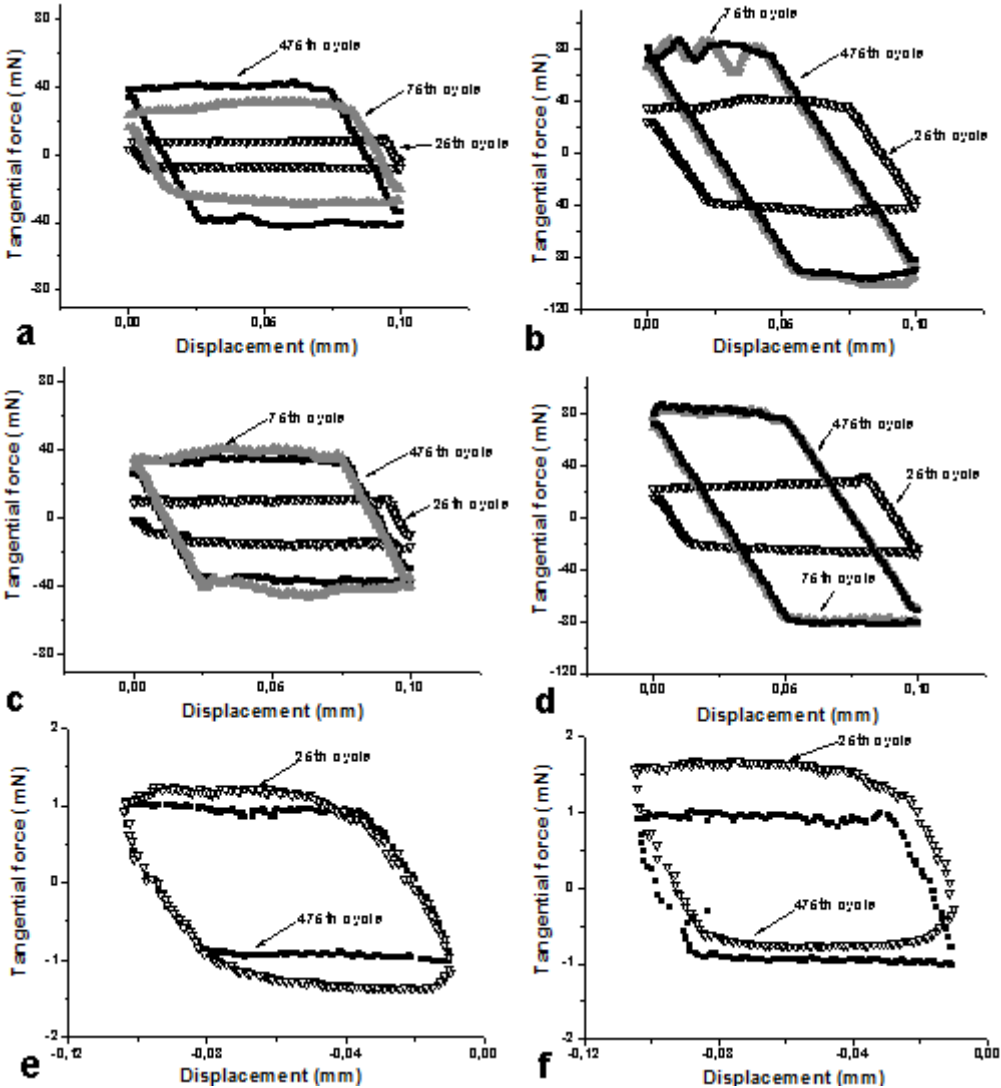


Figure 3.24: Representative fretting loops of a,b)S1 under 40, 80mN, respectively, c,d)S2 under 40, 80mN respectively e,f) S1, S2, respectively under 1N

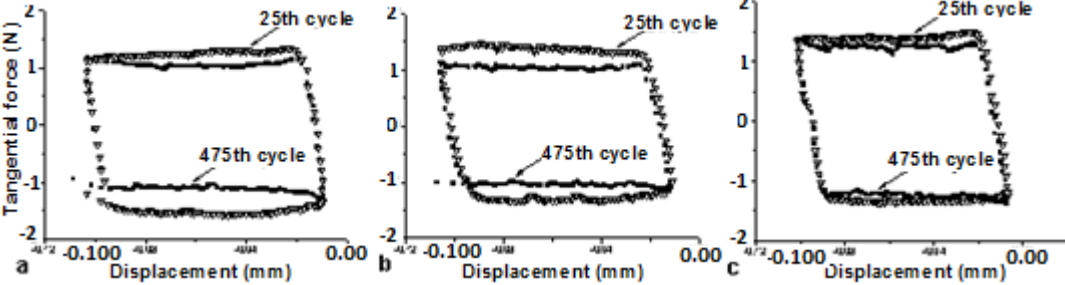


Figure 3.25: Fretting loops of a)O1, b)O2, c)O3 under 1000mN loading

Slip ratios are given in Table 3.5:

Table 3.5: Slip ratios of O1, O2 and O3

Normal Load (mN)	Slip ratio		
	O1	O2	O3
1000	0.9	0.9	0.85

Fretting loops were in gross slip regime and wear mechanism was abrasive wear which was in combination with adhesive wear. Evolution of dissipated energy with respect to tangential force was similar to the evolution we saw in hysteresis loops of S1 and S2. Tangential force decreased with fretting cycles. AAO structure also exerted a similar effect on wear behaviour as that we observed in nanoindentation tests.

3.2.4.1 Evolution of coefficient of friction

Evolution of friction coefficient with number of cycles under various loads for both S1 and S2 is given in figure 3.26. Under meso-scale loads, running in period followed an increasing trend. Mechanism during running in period was explained previously. At steady state COF reached approximately 0.9. Under macro-scale loading, running-in followed a decreasing trend and at steady state COF was approximately 1, which was quite close to that measured under meso-scale loading. Results showed a slight difference in relation to loading scale but this can be linked to possible errors during tests since the test machines used were different.

COF of samples produced in oxalic acid was calculated from the previously given loops and unlike hardness, there wasn't a steady increase or decrease in relation with porosity percentage. O3 with the highest porosity had the highest COF namely ~1.45. O2 had the lowest values. These values were ~1.4 during running in period then decreased to ~1.1 at steady state. COF of O1 was ~1.5 at the beginning but at steady state it was around 1.3. Evolution of COF of O1, O2 and O3 with number of cycles is given in figure 3.27.

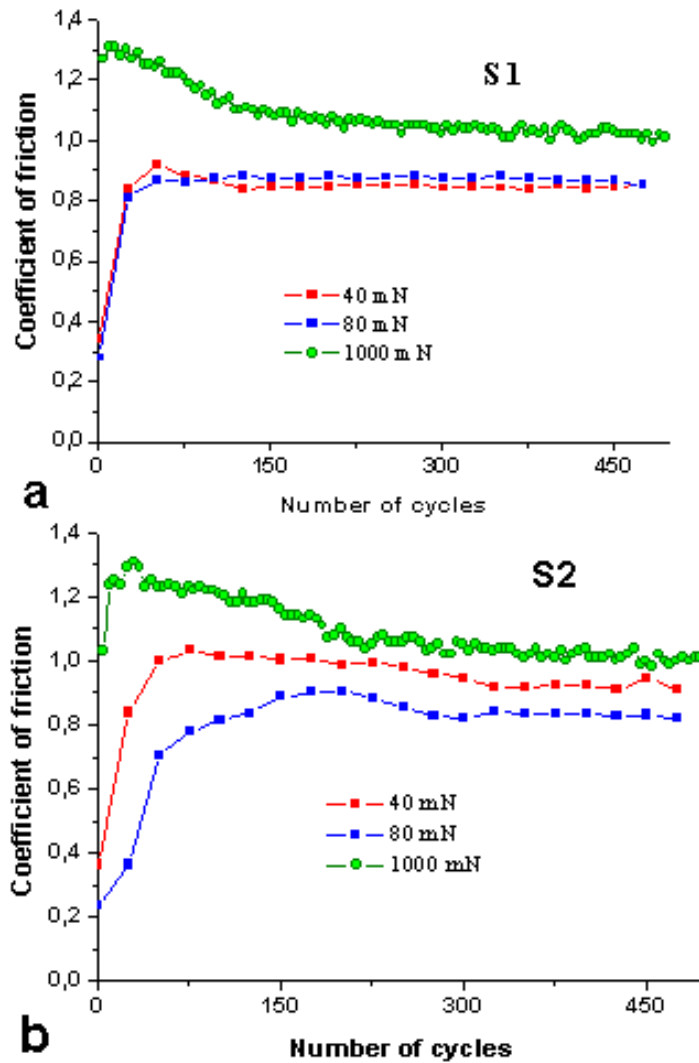


Figure 3.26: Evolution of friction coefficient with number of cycles under various loads a)S1 b)S2

Evolution of COF values of all samples under 1000mN normal load are given in figure 3.28. It must be noted that high COF was expected for all samples as we employed a corundum counterbody which was the same material as the base material. Similar COF evolution was noticed on O2, S1 and S2 which had rather close porosity percentages to each other. COF of these samples were ~1.35 at the beginning followed by a decrease to ~1.1 at steady state. Similarity of the results might be as a result of close porosity percentages which in a way effects the absorbed debris amount and penetration depth of the ball. COF of O1 was higher probably due to more contact area. It can be noticed that the decreasing rate of O1 and O2 are almost the same. This similarity is most likely to be as a result of compacted debris formation on both samples. According to the theory, less porosity more contact area; O3 with highest porosity should have had the lowest COF. It also absorbed most of

wear particles. At this point high penetration depth on O3 showed its significant effect. As the ball goes deeper down inside the oxide layer, it is surrounded by more tubes as if it was buried within AAO and this requires more tangential force to carry out a reciprocating motion. This might be the reason behind high COF, namely ~ 1.5 . By formation of layered debris, we realised a decrease in COF leading to a steady state on O1, O2, S1 and S2. As for O3, such thirdbody was slightly formed after 500 cycles (This will be discussed in the next part). Thus, COF in the beginning of the test was almost the same as that in the end.

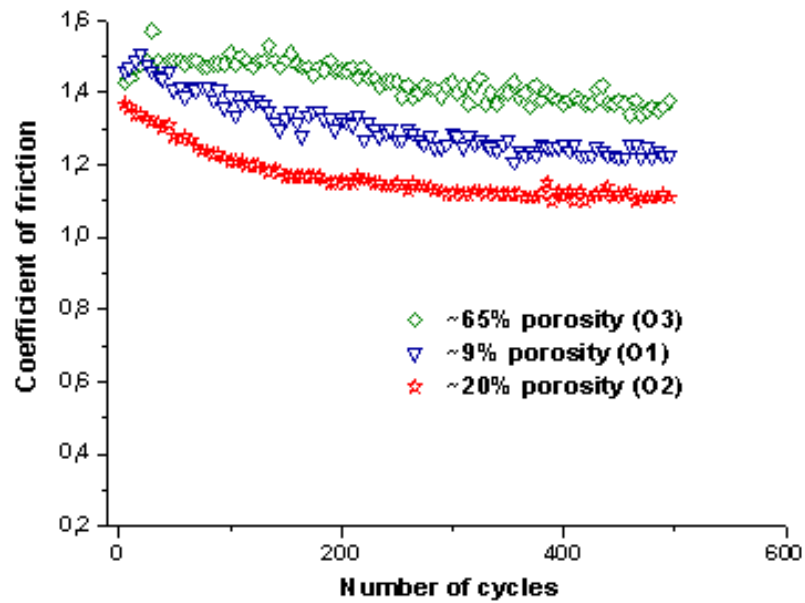


Figure 3.27: Evolution of COF of samples produced in oxalic acid under 1000mN

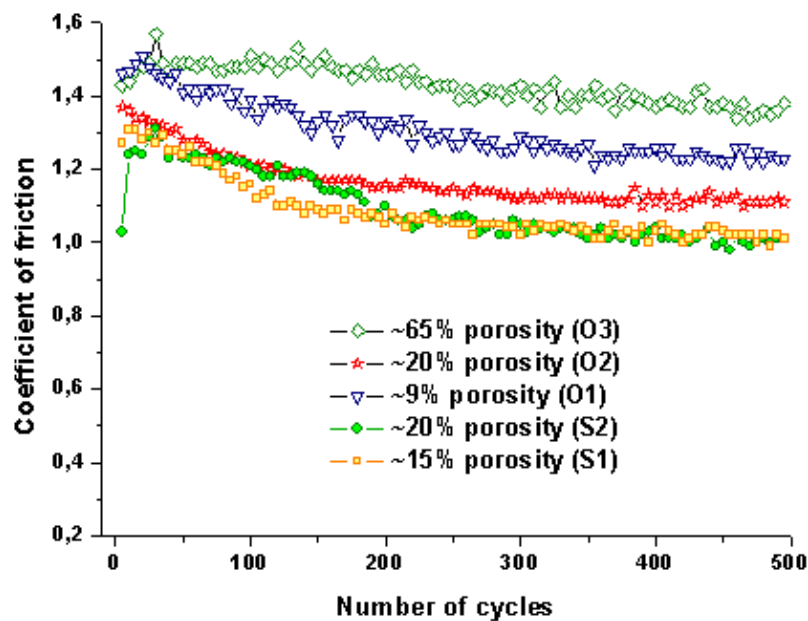


Figure 3.28: Evolution of COF of all samples

3.2.4.2 Wear tracks

SEM images of wear tracks on samples produced in sulphuric acid are given in figure 3.29. Debris was sparsely distributed on the surface in piles forming a tribolayer (thirdbody). This distribution can be seen in figure 3.29a,d,g. Light grey areas are the thick debris packs while dark grey represents worn surface covered with a very thin layer including minor cracks which was similar to the ones seen after nanoindentation (figure 3.30). The tribolayer consisting of compacted wear particles (combination of AAO and corundum), exhibits a layered structure as seen in figure 3.29b,e,g. As well as the amount of layered structure, density of the layers seems to increase as the normal load increases. The debris adhering locally at some parts in the wear track causes a complex wear mechanism, namely a combination of abrasive and adhesive wear together with a high coefficient of friction (figure 3.26). Considering that the wear tracks were ultrasonically cleaned in absolute ethanol prior to SEM observation, we can say that debris is highly adherent.

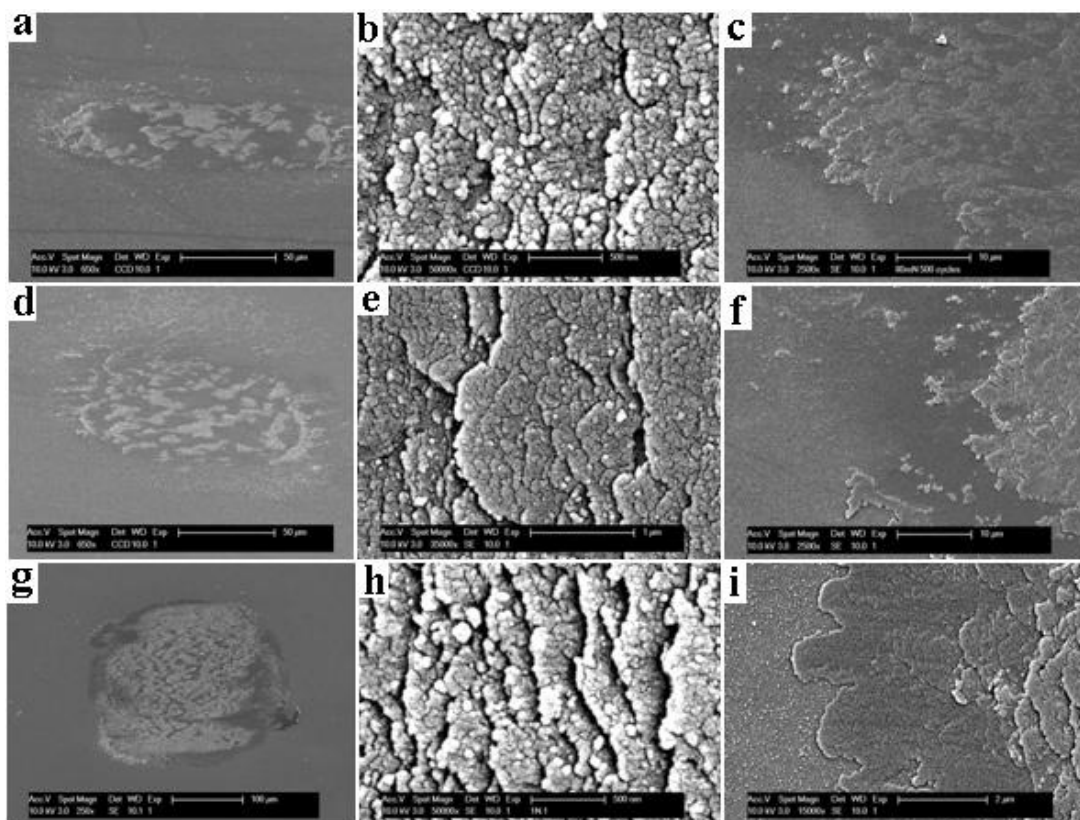


Figure 3.29: SEM images of wear tracks at various magnifications on S2 under a normal load of a-c)40mN, d-f)80mN, g-i)1000mN

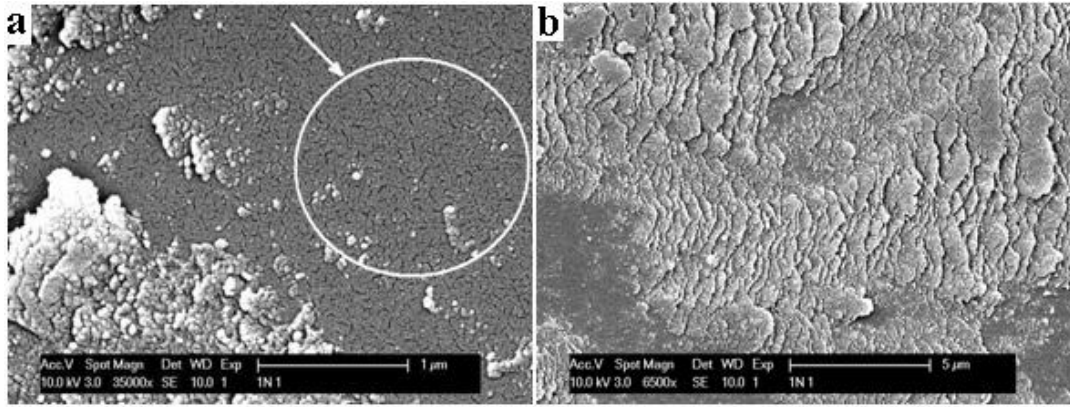


Figure 3.30: a)Thin debris layer with minor cracks (dark grey), b)Layered debris structure (light grey)

Wear tracks of O1 and O2 were similar to those produced in sulphuric acid. Inside the wear track, there were compacted debris particles. Layered structure was observed and debris was sparsely distributed. Indeed, same complex wear mechanism as that of sulphuric acid samples was present resulting in high COF. Some pores in areas where compacted debris did not adhere, were still visible even after 500 cycles. They were partially filled with debris. SEM images of wear track on O2 are given in figure 3.31.

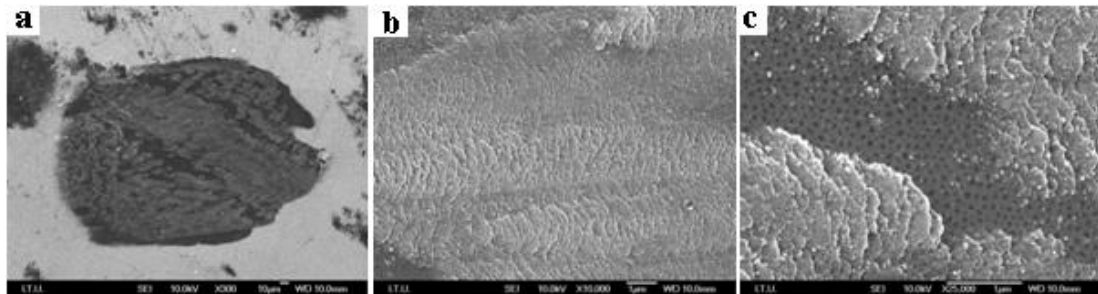


Figure 3.31: SEM images of wear tracks at various magnifications on O2 under a normal load of 1000mN

On a closer look at the wear track on O3 (figure 3.32), a significant difference was realised. At low magnifications (figure 3.32a) light greyish areas on O1 and O2 were not present on O3. At high magnification (figure 3.32b) it was observed that layered and compacted debris was neither as dense nor as thick as that seen on O1 and O2. Pores were more visible. Tubes were filled with most of the debris and formation of the dense and thick layered structure was partially inhibited by this mechanism. As can be guessed from the look of the wear track, tubes were just overfilled and in case of running the test for longer durations, similar layered structure would be achieved.

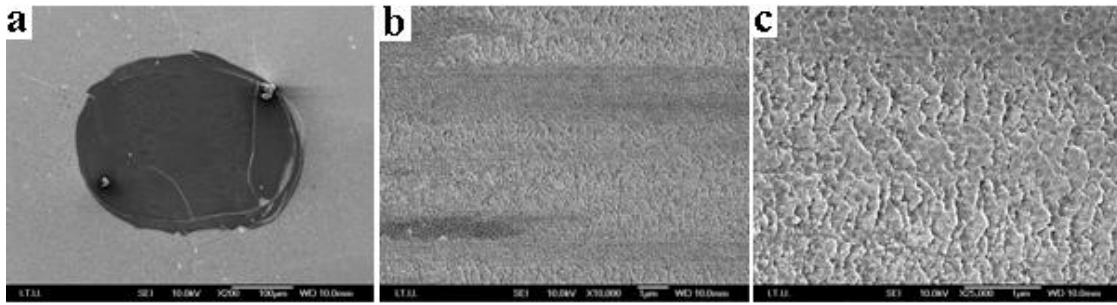


Figure 3.32: SEM images of wear tracks at various magnifications on O3 under a normal load of 1000mN

In figure 3.33a, areas indicated with white circles are the layered structures which had just started to form and black circles show filled-in pores. Like the previous oxalic acid samples, tubular structure was not damaged. However, crack propagation was noticed both inside and outside the wear track (pointed with arrows in figure 3.33b). This behaviour can be linked to the high penetration depth of the ball on O3. Since the solid area fraction was low, applied load caused a very high pressure which resulted in a deep penetration. High pressure together with fretting was relatively destructive for O3. Yet, despite the cracks, majority of pores were durable.

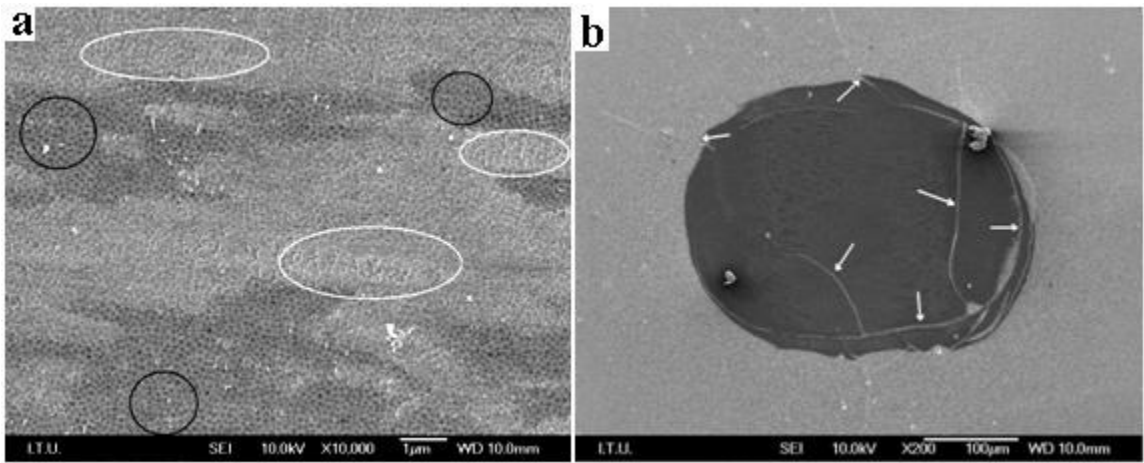


Figure 3.33: a)SEM image of wear track under a normal load of 1000mN on O3 at high magnification b)Cracks (indicated with arrows) within the same wear track on O3

Finally, rigid behaviour of AAO produced in oxalic acid was more obvious after comparing SEM images. No minor cracks were formed on AAO produced in oxalic acid which can be seen in figure 3.31c and figure 3.33a. On the other hand, having a

relook at figure 3.30a, it was clearly seen that minor cracks were formed as those previously seen after nanoindentation.

Despite all the wear and debris formation under harsh fretting conditions, the most interesting result was that the tubular structure was retained after a filling-in.

4. CONCLUSIONS

In this study, we produced anodic aluminium oxide in different electrolytes. Pore diameters were modified. Mechanical properties and frictional behaviour of AAO were investigated depending on porosity percentage and anodization bath used.

- Effect of different electropolishing methods were revealed by interferometer and SEM investigations. Method I revealed a better surface profile. Method II caused a relative undulation on the surface.
- It was observed that two-step anodization improved the well-ordered arrangement of pores.
- Pore diameter was proportional to applied potential. Anodization speed increased with increment in potential. As well as potential, electrolyte was an important parameter for anodization rate. Sulphuric acid anodizing was faster than oxalic acid.
- Pore diameters were adjusted according to the needs by pore widening which was performed in a diluted H_3PO_4 solution. Widening speed was slow and it made controllability of the process much easier.
- Normal loading by nanoindentation did not reveal any major crack propagation on AAO. Penetration depth was highly effected by porosity percentage. Type of electrolyte used for anodization had influence on deformation mechanism. Although no major cracks were observed, minor cracks were present on samples produced in sulphuric acid. On the other hand oxalic acid anodizing revealed a more rigid behaviour. Presence of aluminium hydroxide compounds in both cases might have effects on the results. Thus, possible effect of chemical composition should be deeply studied.
- Hardness varied in accordance with porosity. Increment in porosity percentage caused a decrease in hardness of the surface.

- Sulphuric acid anodizing led to a slight decrease in hardness compared to oxalic acid anodizing.
- Elastic modulus of AAO depended on both porosity and anodizing bath. Elastic modulus decreased with applied normal load. Oxalic acid anodizing produced an oxide layer with higher elastic modulus which followed a rather steady trend with penetration depth.
- AAO had a very high COF against a corundum body independent from its composition. Wear caused formation of a thick, compacted and sparsely distributed debris. It smeared on the surface and showed a highly adherent behaviour. Pores were partially filled with debris in the beginning of the fretting test. Increment in porosity increased the absorbance of fine wear particles.
- Effect of electrolyte type was also observed after fretting tests. Surface of oxalic acid samples did not reveal any of those minor cracks seen on sulphuric acid samples.
- Well-ordered porous structure was retained under the compacted debris layer.

REFERENCES

- Adelkhani, H., Nasoodi, S. and Jafari, A.H.**, 2009, A study of the morphology and optical properties of electropolished aluminium in the Vis-IR region, *International Journal of Electrochemical Science*, **4**, pp. 238-246
- Aryasomayajula, A., Randall, N.X., Gordon, M.H. and Bhat, D.**, 2008, Tribological and mechanical properties of physical vapor deposited alpha alumina thin film coating, *Thin Solid Films*, **517**, pp. 819-823
- Baxi, J.**, 2008, Tribological Characterization of Liquids and Nanofluids, *MSc. Thesis*, Texas A&M University, Texas, USA
- Bensalah, W., Feki, M., Wery, M. and Ayedi, H.F.**, 2011, Chemical dissolution resistance of anodic oxide layers formed on aluminum, *Trans. Nonferrous Met. Soc. China*, **21**, pp. 1673-1679
- Choi, J.**, 2004, Fabrication of Monodomain Porous Alumina Using Nanoimprint Lithography and Its Applications, *PhD. Thesis*, Martin-Luther-Universitat Halle, Wittenberg, Germany
- De Wolf, I.**, 2010, Materials Characterization Techniques : Nanoindentation, Retrieved 10.12.2010, from MatCharTech-Nanoindentation_final.ppt
- Fang, T.H., Wang, T.H., Kang, S.H. and Chuang, C.H.**, 2009: Indentation deformation of mesoporous anodic aluminium oxide, *Current Applied Physics*, **9**, pp. 880-883
- Fang, T.H., Wang, T.H., Liu, C.H., Ji, L.W. and Kang S.H.**, 2007: Physical behavior of nanoporous anodic alumina using nanoindentation and microhardness tests, *Nanoscale Research Letters*, **2**, pp.410-415
- Fischer-Cripps, A.C.**, 2002, Nanoindentation, Springer
- Gallego, L. and Nelias, D.**, 2007, Modeling of fretting wear under gross slip and partial slip conditions, *Journal of Tribology*, **129**, pp. 528-535
- Hagelsieb, L.M.**, 2007, Anodic Aluminum Oxide Processing, Characterization and Application to DNA Hybridization Electrical Detection, *PhD. Thesis*, Universite Catholique de Louvain, Louvain-La-Neuve, Belgique
- Huh, S.H., Riu, D.H., Choi, J., Kim, S.J., Jin, E.J., Shin, D.G. and Cho, K.Y.**, 2007, Surface and bottom structures of grouped alumina nanopores, *Journal of the Korean Physical Society*, **51**, pp. L1-L3
- Jiang, C.X., Tu, J.P., Guo, S.Y., Fu, M.F. and Zhao, X.B.**, 2005, Friction properties of oil-infiltrated porous AAO film on an aluminium substrate, *Acta Metallurgica Sinica (English Letters)*, **18**, pp. 249-253
- Khan, I.U., John, P., Sheikh, S.T., Gulzar, N. and Rehman, A.U.**, 2010, Anodizing of aluminum with improved corrosion properties, *J.Chem.Soc.Pak*, **32**, pp. 46-51

- Kim, H.S., Kim, D.H., Lee, W., Cho, S.J., Hahn, J.H. and Ahn, H.S.,** 2010 : Tribological properties of nanoporous anodic aluminium oxide film, *Surface & Coatings Technology*, doi:10.1016/j.surfcoat.2010.07.056
- Ko, S., Lee, D., Jee, S., Park, H., Lee, K. and Hwang, W.,** 2005: Mechanical properties and residual stress measurements in anodic aluminium oxide structures using nanoindentation, *Glass Physics and Chemistry*, **31**, pp. 356-363
- Ko, S., Lee, D., Jee, S., Park, H., Lee, K. and Hwang, W.,** 2006: Mechanical properties and residual stress in porous anodic alumina structures, *Thin Solid Films*, **515**, pp. 1932-1937
- Kothari, A.K., Konca, E., Brian, W.S., Jian, K., Li, H., Xia, Z., Ni, W. and Hurt, R.,** 2009: Mechanical behavior of anodic alumina coatings reinforced with carbon nanofibres, *Journal of Material Science*, **44**, pp. 6020-6027
- Lee, G.S., Choi, J.H., Choi, Y.C., Bu, S.D. and Lee, Y.Z.,** 2011, Tribological effects of pores on an anodized Al alloy surface as lubricant reservoir, *Current Applied Physics*, doi:10.1016/h.cap.2011.03.057
- Lee, W.,**2010: The anodization of aluminium for nanotechnology applications, *JOM*, **62**, pp.57-63
- Lillo, M. and Losic, D.,** 2009, Pore opening detection for controlled dissolution of barrier oxide layer and fabrication of nanoporous alumina with through-hole morphology, *Journal of Membrane Science*, **327**, pp.11-17
- Ma, D., Li, S. and Liang, C.,** 2009, Electropolishing of high-purity aluminium in perchloric acid and ethanol solutions, *Corrosion Science*, **51**, pp. 713-718
- Maejima, M., Saruwatari, K., Takaya, M.,** 2000: Friction behaviour of anodic oxide film on aluminium impregnated with molybdenum sulfide compounds, *Surface and Coatings Technology*, **132**, pp. 105-110
- Masuda, H. and Fukuda, K.,**1995, Ordered metal nanohole arrays made by a two-step replication of honeycomb structures of anodic alumina, *Science*, **268**, pp. 1466-1468
- Ng, K.Y., Lin, Y. and Ngan, A.H.W.,** 2009, Deformation of anodic aluminium oxide nano-honeycombs during nanoindentation, *Acta Materialia*, **57**, pp. 2710-2720
- O'sullivan, J.P. and Wood, G.C.,**1970, The morphology and mechanism of formation of porous anodic films on aluminium, *Proc. Roy. Soc. Lond.A.*, **317**, pp. 511-543
- Öztürk, S., Taşaltın, N., Kiliç, N. and Öztürk, Z.Z.,** 2009, Fabrication of ZnO nanotubes using AAO template and sol-gel method, *Journal of Optoelectronic and Biomedical Materials*, **1**, pp. 15-19
- Paşaoğlu, I.,**2011, Electrodeposition and Characterization of Free Standing Ni-W Nanowires on Anodized Aluminum Oxide Templates, *MSc. Thesis*, Istanbul Technical University, Istanbul, Turkey

- Skeldon, P., Wang, H.W. and Thompson, G.E.,** 1997: Formation and characterization of self-lubricating MoS₂ precursor films on anodized aluminium, *Wear*, **206**, pp. 187-196
- Stachowiak, G. and Batchelor, A.W.,**2001, Engineering Tribology Second Edition, Butterworth-Heinemann
- Suciu, C.V. and Uchida, T.,**2010, Modeling and Simulation of the Fretting Hysteresis Loop, *International Conference on P2P, Parallel, Grid and Internet Computing*,doi 10.1109/3PGCIC.2010.96
- Sulka, G.D. and Parkola, K.G.,**2006: Anodizing potential influence on well-ordered nanostructures formed by anodization of aluminium in sulphuric acid, *Thin Solid Films*, **515**, pp. 338-345
- Sulka, G.D. and Stepniowski, W.J.,**2009, Structural feature of self-organized nanopore arrays formed by anodization of aluminium in oxalic acid at relatively high temperatures, *Electrochimica Acta*, **54**, pp. 3683-3691
- Takadom, J.,**2008, Materials and Surface Engineering in Tribology, ISTE Ltd
- Takaya, M., Hashimoto, K., Toda, Y., Maejima, M.,** 2003: Novel tribological properties of anodic oxide coating on aluminium impregnated with iodine compound, *Surface and Coatings Technology*, **169-170**, pp. 160-162
- Vojkuvka, L., Marsal, L.F. and Pallares, J.,** 2007, Study of porous alumina porosity after pore widening process, *IEEE*,1-4244-0869-5, pp. 41-43
- Wang, Y.C., Leu, I.C. and Hon, M.H.,** 2004: Dielectric property and structure of anodic alumina template and their effects on the electrophoretic deposition characteristics of ZnO nanowire arrays, *Journal of Applied Physics*, **95**,pp. 1444-1449
- Wernick, S., Pinner, R. and Sheasby, P.G.,** 1987, The surface treatment and finishing of aluminum and its alloys 5th Edition, ASM International
- Xia, Z., Riester, L., Sheldon, B.W., Curtin, W.A., Liang, J., Yin, A. and Xu, J.M.,** 2004, Mechanical properties of highly ordered nanoporous anodic alumina membranes, *Rev.Adv.Mater.Sci.*, **6**, pp. 131-139
- Yang, F. and Li, J.C.M.,**2008, Micro and nano mechanical testing of materials and devices, Springer
- Zaraska, L., Sulka, G.D. and Jaskula, M.,** 2010, Porous anodic alumina membranes formed by anodization of AA1050 alloy as templates for fabrication of metallic nanowire arrays, *Surface & Coatings Technology*, doi:10.1016/j.surfcoat.20.10.09.038
- Zhang, L., Zhang, P. and Fang, Y.,** 2007, An investigation of the surface-enhanced Raman scattering effect from new substrates of several kinds of nanowire arrays, *Journal of Colloid and Interface Science*, **311**, pp. 502-506
- Zhao, S., Chan, K., Yelon, A. and Veres, T.,** 2007, Novel structure of AAO film fabricated by constant current anodization, *Advanced Materials*,**19**, pp.3004-3007
- Url-1**<<http://en.wikipedia.org/>>, accessed at 15.08.2011

Url-2< <http://www.anodizing.org> >, accessed at 16.08.2011

Url-3<<http://electrochem.cwru.edu> >, accessed at 16.08.2011

Url-4< www.metalfinishing.com >, accessed at 16.08.2011

Url-5< <http://www.substech.com> >, accessed at 18.08.2011

Url-6< <http://www.engineersedge.com> >, accessed at 10.09.2011

Url-7< <http://frettingwear.com> >, accessed at 10.09.2011

CIRRICULUM VITAE

Candidate's full name: Berkay KAVAS

Place and Date of Birth: İstanbul, 11.04.1986

Permanent Address: Selvilik Cad. No:72/4 Üsküdar / İstanbul

Education: İstanbul Technical University, M.Sc.(2009-2011)

Yıldız Technical University, B.Sc. (2004-2008)

Hüseyin Avni Sözen Anatolian High School

(1997-2004)

Publications:

Kavas, B.,Tsyntaru, N., Urgan, M., Celis, J.-P., 2011, Tribological and mechanical properties of anodized aluminium oxide, *1st Surface Treatment Symposium*, Istanbul, Turkey, 15-18 June